ABSTRACT

Title of dissertation: SPIN INJECTION AND DETECTION
IN COPPER SPIN VALVE STRUCTURES

Samir Garzón, Doctor of Philosophy, 2005

Dissertation directed by: Richard A. Webb
Department of Physics

We report measurements of spin injection and detection in a mesoscopic copper wire from which the electron spin relaxation time and the spin current polarization in copper can be found. Spin injection is realized by applying a voltage to drive a current from a ferromagnet into the normal metal, while spin detection is done using transport measurements. Precession of the spin of the injected electrons due to an external magnetic field is also studied. The existence of a previously unobserved spin signal which vanishes at low temperatures but increases nonlinearly above 100^oK is reported and a possible explanation for its origin, based on interfacial spin-flip scattering, is suggested. Multiple cross checks to test the possibility of artifacts as an origin of this signal are discussed.

An alternative spin detection method using magnetic force microscopy (MFM)

is also studied. This method measures the magnetic field produced by the injected spins directly, so the spin coherence length and the spin current polarization can be extracted directly without the need of a particular transport model, avoiding issues like contact resistance and interface scattering. The MFM method can also be useful for measuring the spin polarization of currents in semiconductors and semiconductor heterostructures, which is important for the development of spintronics.

SPIN INJECTION AND DETECTION

IN COPPER SPIN VALVE STRUCTURES

by

Samir Garzón

Dissertation submitted to the Faculty of the Graduate School of the
University of Maryland, College Park in partial fulfillment
of the requirements for the degree of
Doctor of Philosophy
2005

Advisory Commmittee:

Professor Richard A. Webb, Chair/Advisor
Professor J. Robert Anderson
Assistant Professor Michael S. Fuhrer
Professor Romel D. Gomez
Professor Ellen D. Williams

ACKNOWLEDGEMENTS

First of all I want to give thanks to my family. To my mom and dad, who, from a distance, provided constant support and encouragement. They helped me get through the toughest moments. To my sister, Cosh, who was always able to put a smile on my face. And to my brother, who was always there when I needed him.

I also want to give thanks to Professor Webb for his help in the lab and his patience at times when research progress was slow, but over all, for allowing me the freedom to work on my own. I want to thank my labmates, Chen and Tarek, for their company and conversations, which made the lab feel like a second home. I want to give special thanks to Chen for his encouragement during the last year. The dissertation committee members, Professors Anderson, Fuhrer, Gomez, and Williams, also deserve many thanks for having taken the time to understand my work and for giving me valuable suggestions. Professors Fuhrer, Gomez, and Williams deserve additional thanks for allowing me to use the MFM's in their labs.

I want to give special thanks to Igor for being of great help during the last year. He gave very valuable suggestions, facilitated useful discussions with Dr. Mark Johnson from NRL, and encouraged me to go on during some tough moments.

I also want to thank the staff in the Center for Superconductivity Research, who was always helpful and kept things running smoothly, and the technicians in charge of maintenance, especially those in charge of the HVAC, since they were always willing to help, and kept the system running (or at least, walking). I also want to thank the Physics Department staff for their help. In particular I want to thank Lorraine, who helped keep the lab moving whenever we had technical problems, and quickly relocated us once Webb's lab moved out, and to Jane, who was always willing to help, and made dealing with paperwork a much easier task.

Finally, I want to thank all my friends, inside and outside the Physics Department, for making the time outside the lab enjoyable. Without them, these five and a half years in College Park wouldn't have been worthwhile. I want to give special thanks to my roommates, Juan and Luis, who were my second family, and to Paiki, for her time, company, and patience.

TABLE OF CONTENTS

LIST OF FIGURES

LIST OF TABLES

Chapter 1
Introduction

This thesis reports measurements of spin injection and detection in a mesoscopic copper wire from which the electron spin relaxation time and the spin current polarization in copper can be found. Spin injection is realized by applying a voltage to drive a current from a ferromagnet into the normal metal, while spin detection is done using transport measurements. Precession of the spin of the injected electrons due to an external magnetic field is also studied. The existence of a previously unobserved spin signal which vanishes at low temperatures but increases nonlinearly above 100K is reported and a possible explanation for its origin, based on interfacial spin-flip scattering, is suggested. Multiple cross checks to test the possibility of artifacts as an origin of this signal are discussed.

An alternative spin detection method using magnetic force microscopy (MFM) is also proposed. This method measures the magnetic field produced by the injected spins directly, so the spin coherence length and the spin current polarization can be extracted directly without the need of a particular transport model, avoiding issues like contact resistance and interface scattering. The MFM method, as opposed to the transport method [1], can also be useful for measuring the spin polarization of

currents in semiconductors and semiconductor heterostructures, which is important for the development of spintronics.

The outline of this thesis is as follows. Chapter 1 defines the concept of spintronics and motivates the idea of studying spin injection and detection by providing a brief overview of the field. The essence of spin injection and detection via transport is discussed, as well as the possibility of using MFM detection. Chapter 2 introduces concepts such as single electron coherence time, spin relaxation time, and spin dephasing time, and gives a brief overview of the spin scattering mechanisms relevant for conduction electrons in metals. Chapter 3 discusses spin-dependent transport in metallic systems, considering the cases of transparent and resistive interfaces, and local and nonlocal measurement configurations. Additionally the spin precession of electrons is studied and the effect of interface spin flip scattering is considered. Chapter 4 explains the details of sample fabrication and experimental setup. The results and analysis of the spin valve measurements are presented in chapter 5 together with relevant cross-checks to clarify the role of geometrical effects, and heating and thermoelectric effect. This finishes the first part of the thesis, which explores spin injection and detection via transport in spin valve structures. The following two chapters discuss spin detection using MFM. Chapter 6 introduces scanning probe microscopy and its limitations, discusses calibration procedures for the cantilevers, and shows some of the improvements that were made in the resolution and sensitivity of the MFM. Then, chapter 7 shows the additional improvements in signal detection and sample design that were made, and the null results of the measure-

ments. Finally, conclusions and possible directions for future work are presented in chapter 8.

1.1 Spintronics

Simply stated, electronics is to electric charge as spintronics is to electron spin. Spintronics, therefore, studies the spins of electrons and their interaction with the surrounding solid state system. The essential quantities are the population of electrons in different spin states, and their relative phase, which gives the degree of coherence of the spin populations. Creating a spin-polarized population of electrons in a nonmagnetic material involves perturbing the system from equilibrium. This can be done using optical techniques in which, by shining circularly polarized light on a particular region, a nonequilibrium spin population is created by the transfer of angular momentum [2]. Equivalently, by injecting a current from a ferromagnetic material, which has a net spin polarization of the conduction electrons, a nonequilibrium spin population can also be created [3]. The spin polarization diffuses away from the injection region, so the spin accumulation is given by a balance of the spin being produced within a region, the spin leaving (or entering) the region, and the rate at which the nonequilibrium spin population relaxes and dephases. Typical spin-independent momentum relaxation mechanisms like phonons and boundary or impurity scattering can cause spin relaxation due to spin-orbit coupling which mixes the two spin channels [4, 5]. Additionally, spin-dependent scattering off magnetic impurities also contributes to momentum and spin relaxation. Hence, in order to exploit electronic spin for the fabrication of novel devices, it is essential to measure

the spin relaxation times and the magnitude of the spin polarization, and to find ways to enhance them.

The single most important application of spintronics is the use of Giant Magneto Resistive (GMR) effects for magnetic reading heads. All of the currently available hard drives with GByte storage capacities use GMR magnetic heads for the readout of stored information. The principle of operation is based on the concept of a spin valve. Simply stated, a spin valve is a structured composed of layers of magnetic and nonmagnetic materials, such that the device resistance depends on the relative alignment of the magnetization of the magnetic layers. Figure 1.1(a) shows a simple schematic of a GMR structure used for magnetic reading heads. Two ferromagnetic films (F_1 and F_2) are separated by a thin layer of a nonmagnetic metal (N). The magnetization of the top magnetic electrode is pinned as shown in Fig. 1.1(a) by means of an additional antiferromagnetic layer (not shown in the schematic). The magnetization of the lower magnetic electrode is free to rotate in the plane of the film. As the magnetic reading head is scanned over the surface of a magnetic storage disk, the magnetization of F_1 rotates in response to the field produced by each of the bits in the magnetic disk. By applying a sensing current in the plane of the films (CIP) and measuring the voltage between the two leads, the state of the bit can be detected since the resistance between the leads depends on the alignment of the magnetization of the two ferromagnetic films. Another important spintronic application is a Magnetic Tunnel Junction (MTJ), which can be used as a memory device to store a bit of information. A schematic of such a

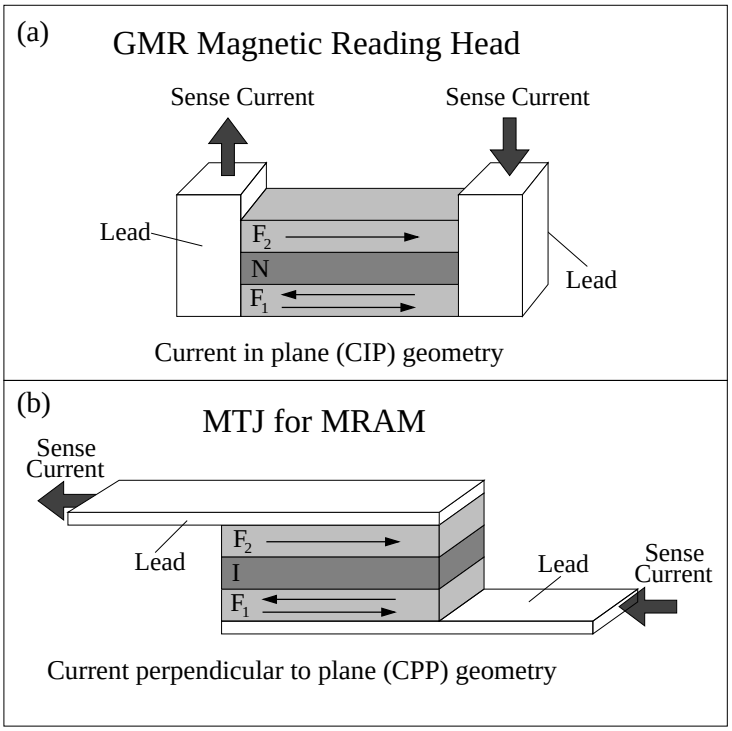

Figure 1.1: (a) Schematic of a GMR structure for a magnetic reading head. The two ferromagnetic layers (F_1 and F_2) separated by a nonmagnetic metal (N) are shown, together with the leads for applying a sensing current. (b) Schematic of a Magnetic Tunnel Junction (MTJ) used for Magnetic Random Access Memories (MRAM's).

device is shown in Fig. 1.1(b). The structure is similar to that of GMR, except that the nonmagnetic material is replaced by an insulator, and the sensing current is driven perpendicular to the plane of the films (CPP). Depending on the state of the magnetization of F_1, either parallel or antiparallel to F_2, the measured resistance between the leads is different. Since no power is necessary to keep the memory state of the system, such a device is referred to as being nonvolatile, meaning that no information is lost after power-off. By fabricating arrays of such structures, it is possible to fabricate a Magnetic Random Access Memory (MRAM) which could replace actual RAM's used in everyday computers since, being nonvolatile, they

require no turn-on time. The speed at which this devices can operate, their power consumption, and the maximum storage density they can achieve depend on the magnitude of the resistance change between the parallel and antiparallel configurations. The size of this resistance change in GMR structures and MTJ's is directly related to the degree of spin current polarization that is either injected into the normal metal (GMR) or that tunnels across the insulating barrier (MTJ's), which is very sensitive to interface effects. Therefore studying the spin transport across ferromagnetic-nonmagnetic (F-N) and insulating interfaces can be important for the development of hard drives and MRAM's that are faster, more power efficient, and have larger storage density than the ones currently available.

The basis for understanding spin-polarized transport is due to Mott [6, 7], who realized that the electrical current in ferromagnets could be expressed as the sum of two independent and unequal parts for two different spin projections implying that the current is spin-polarized. This idea of a two-current model was extended by Campbell, Fert, and Valet [8, 9, 10], and provides the explanation for different kinds of magnetoresistive effects[1] such as giant magnetoresistance (GMR) and tunnelling magnetoresistance (TMR), key elements in applications such as magnetic hard drives and nonvolatile magnetic random access memory (MRAM) [11, 12].

The interest to study spin accumulation, one of the key elements in spintronic applications [13], is not limited to novel spin-based devices. Spin injection can also be used as a sensitive spectroscopic tool to study fundamental properties such as the

[1]Changes in the resistance in ferromagnetic multi-layer structures depending on the alignment of the magnetizations of the different layers.

pairing symmetry of unconventional superconductors [14, 15], Skyrmion excitations in the quantum Hall regime [16, 17], and spin-charge separation in non-Fermi liquids [18, 19].

Spin accumulation in metals was first demonstrated by Johnson and Silsbee [3], who injected a spin polarized current from permalloy into bulk aluminum and detected the nonequilibrium spin polarization with a second permalloy contact at a distance L from the injector. By fabricating samples with different L and by performing spin precession measurements, they were able to extract information on the degree of spin polarization and the spin relaxation length for aluminum. Johnson extended these studies to thin gold films [20, 21]. Later, Jedema et. al. [22] applied Johnson's injection technique to mesoscopic devices and measured the spin relaxation length and the spin polarization in copper. However, their geometry was not optimal, the data was not very reproducible, and the analysis of the results questionable. In a later improved experiment Jedema et. al. [23] studied injection into aluminum through a tunnel barrier and used spin precession to extract the degree of spin polarization and the spin relaxation length in a mesoscopic aluminum wire. In this thesis, spin injection and detection measurements in copper mesoscopic wires are performed using both the cross geometry configuration reported by Jedema et. al. [22] and a completely nonlocal configuration. Experiments with both transparent and resistive interfaces are discussed, and spin precession with tunnel barriers is studied. Additionally, the temperature dependence of the spin signal is measured, and the appearance of a previously unobserved feature, consistent with interfacial

spin-flip scattering, is reported.

1.2 Spin injection and detection: transport

A nonequilibrium spin polarization in a nonmagnetic material can be generated by driving a current from an adjacent ferromagnetic material. The basic principle can be understood by studying Fig. 1.2, which shows the spin dependent density-of-states (DOS) diagrams of a ferromagnet in contact with a nonmagnetic metal. The DOS at the Fermi energy for a ferromagnet is different for spin up and spin down, as shown in the schematic, where spin up has been assumed to be the majority carrier. In the absence of any current flow between the two metals [Fig. 1.2(a)], the system is in equilibrium and therefore all the electrochemical potentials (ECP) are aligned at μ_0, the average ECP. In this case the DOS of the nonmagnetic metal is equivalent for spin up and spin down. By applying a potential difference between the two metals (by means of a battery, for example), a current can be injected from the nonmagnetic metal into the ferromagnet [Fig. 1.2(b)]. This means that electrons will be injected in the opposite direction, that is, from the ferromagnet (F) into the nonmagnetic metal (N). Since the DOS at the Fermi energy in F is larger for electrons with spin up than for electrons with spin down, most of the electrons injected into N will have spin up. This leads to spin accumulation in N as shown in [Fig. 1.2(b)]. To preserve charge neutrality in each of the metals, an increase in the number of electrons with spin up is accompanied by a decrease in the number of electrons with spin down. Therefore charge transport across the F-N interface is accompanied by spin transport. This produces the nonequilibrium configuration

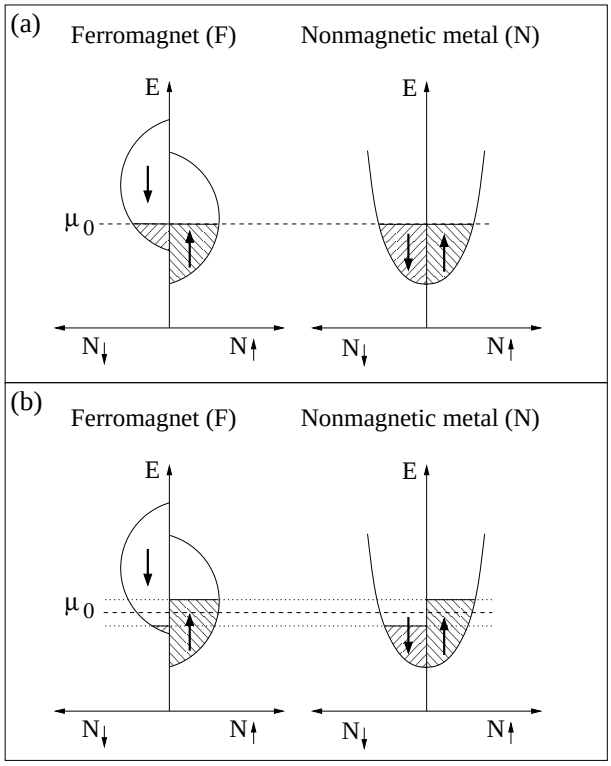

Figure 1.2: Spin dependent density-of-states diagrams of a ferromagnet placed in contact with a nonmagnetic metal when (a) no current is being injected, and (b) a current is driven between the two metals. The dashed line represents the average electrochemical potential μ_0.

of the ECP's shown in [Fig. 1.2(b)], which, for simplicity, have been assumed to be continuous at the interface.

Figure 1.3 gives a more complete picture of the charge-spin coupling in a F-N structure by showing the spin dependent electrochemical potential as a function of position, with the interface being at $x = 0$. An electric current is applied between the nonmagnetic metal and the ferromagnet so that electrons are injected from F into N. The dashed lines at both sides of the interface represent the electrical potential, with the slope of the line being proportional to the resistivity of each metal. As explained above, most of the electrons injected into N have spin up. Therefore $\mu_\uparrow^N$ increases

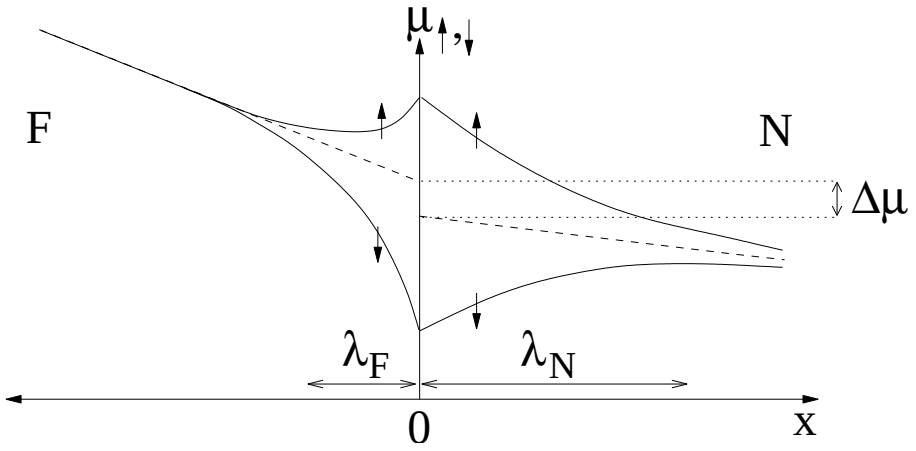

Figure 1.3: Position dependence of the electrochemical potential μ for both spin channels near a F-N interface in the presence of electric current.

with respect to its equilibrium value. This has the following consequences: first, due to charge neutrality, $\mu_{\downarrow}^{N}$ has to decrease so that the total DOS at any position in N is uniform. Since in N the DOS is spin independent, the size of the increase in $\mu_{\uparrow}^{N}$ is equivalent to the size of the decrease in $\mu_{\downarrow}^{N}$. Second, $\mu_{\uparrow}^{F}$ has to increase to avoid back-flow of electrons with spin up from N into F. And third, due to the increase in $\mu_{\uparrow}^{F}$, $\mu_{\downarrow}^{F}$ should decrease, again to preserve charge neutrality. However, since the DOS of F is different for spin up and spin down, a large change in $\mu_{\downarrow}^{F}$ is necessary to compensate for a small change in $\mu_{\uparrow}^{F}$. This produces the asymmetry in the ECP's in F shown in Fig. 1.3. This spin-charge coupling is also responsible for the appearance of the discontinuity in the electrical potential at the F-N interface, which implies the existence of an additional spin-related voltage at the interface $\Delta\mu/e$. In the case of transparent interfaces shown here, the spin dependent ECP's are continuous. As the magnitude of the current increases, so does the deviation in the ECP's from the zero-current value, which increases the size of $\Delta\mu$. The fact

that the spin relaxation length λ is longer in N than in F is also clear from Fig. 1.3.

A conventional model for spin injection across the ferromagnet/nonmagnetic metal (F/N) interfaces [24, 25, 26] is provided by noting that, in each metal, the spin-flip scattering is typically much weaker than the momentum scattering. This leads to a mean free path (MFP) l which is much shorter than the spin diffusion length (SDL) λ–the characteristic scale for the decay of spin accumulation at each side of the interface. Within the two-current model one can then define local spin-resolved electrochemical potentials μ_σ, $\sigma = \uparrow, \downarrow$ for carriers with majority and minority spin (with magnetic moment parallel and antiparallel to the magnetization $\mathbf{M}$ in a ferromagnet). In the steady state an electrical current driven across a F/N junction will lead to spin accumulation proportional to $(\mu_\uparrow - \mu_\downarrow)$ which is the balance between spins added by the magnetization current and spins removed by spin relaxation. In the absence of interfacial spin-flip scattering, the spin-resolved current I_σ is conserved across the interface [25, 26], and the contact resistance for each spin can be expressed as

$$R_\sigma = e(\mu_\sigma^F - \mu_\sigma^N)/I_\sigma, \tag{1.1}$$

where the indices F, N label the quantities in the corresponding region at each side of the contact and e is the proton charge. $R_\uparrow \neq R_\downarrow$ can be inferred from the effect of exchange splitting in the F region, leading to spin-dependent Fermi wave vectors, transmission coefficients, and density of states. Spin accumulation in the N region can act as a source of spin electromotive force which produces a voltage $V \propto (\mu_\uparrow - \mu_\downarrow)$ measurable by adding another ferromagnet [27].

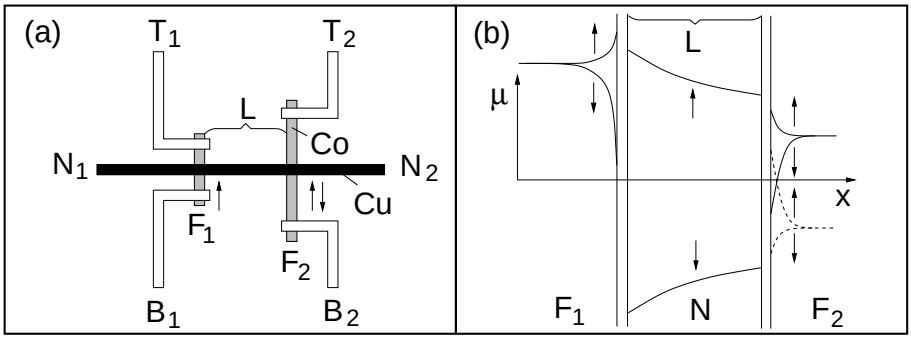

Figure 1.4: (a) Sample geometry. Shaded regions represent two Co ferromagnets separated by a distance L, while the solid black region represents the Cu line. T_i and B_i are nonmagnetic measurement leads. (b) μ_σ for spin up and spin down electrons in injector (left), normal metal (center), and detector (right) as a function of position. Detector μ_σ for parallel (solid) and antiparallel (dashed) magnetizations is shown.

Using different variations of spin valve geometries like the one depicted in Fig. 1.4(a) in which F_1 represents the spin injector and F_2 the spin detector, spin injection and detection measurements can be made. Charge current is driven between the leads T_1 and N_1 while the nonlocal voltage V_{NL} is measured between the leads T_2 and N_2 which, in the absence of nonequilibrium spin, is an equipotential region without a charge current flow such that $V_{NL} = 0$. As compared to local measurements (current driven between B_1 and B_2 and voltage measured between T_1 and T_2), the nonlocal measurement has been shown to simplify the extraction of spurious effects (for example, anisotropic magnetoresistance and the Hall effect) from those intrinsic to spin injection [3, 28]. In Fig. 1.4(b) a spatial profile of μ_σ is sketched for a fixed magnetization of F_1 (pointing $\uparrow$) and for both aligned (pointing $\uparrow$, solid traces in region F_2) and anti-aligned (pointing $\downarrow$, dashed traces in region F_2) magnetization of F_2. The presence of interfacial resistance leads to the discontinuity

of the electrochemical potential $\mu = (\mu_\uparrow + \mu_\downarrow)/2$ at each contact [25, 26, 10]. The region labelled F_1 refers to the upper half of the injector, N refers to the middle section of the nonmagnetic wire between F_1 and F_2, and F_2 refers to the upper half of the detector. $\uparrow$ and $\downarrow$ label the electrochemical potentials of the two spin channels in each region. The value of the average electrochemical potential in region F_2 is the measurable quantity, which is directly related to the magnitude of the residual spin population at the $F_2 - N$ interface. A measurable difference in the average electrochemical potential of F_2 when its magnetization is reversed can be seen as a difference between the dashed and solid lines at the far right.

1.3 Magnetic force microscopy

On the other hand, magnetic force microscopy MFM is an extremely sensitive probing tool for measuring extremely small magnetic field gradients with a resolution of tens to hundreds of nanometers. State of the art cantilevers which require advanced micro-engineering have been fabricated by groups in Stanford and IBM [29, 30] and have been used in a special vertical configuration, low temperature, vacuum, magnetic resonance force microscope to measure a single localized spin [31]. In this work I have attempted to use MFM to measure the magnetic field produced not by one, but by a few hundred electrons which are diffusively moving along a narrow Cu wire, and which have been injected from a neighboring ferromagnetic electrode. Besides requiring large sensitivity and resolution, it is essential to separate the very small magnetic field produced by a few hundred electrons from the very large (1500 times larger) magnetic fields produced by both the injection current and the ferromagnetic

injector. For this purpose high magnetic field resolution cantilevers were fabricated and the MFM setup was optimized by using a multi-frequency resonant method. The essence of the method is to drive the injection current at a frequency ω_1, oscillate the magnetization of the injector at a frequency ω_2, and detect the spin signal at a frequency $\omega_0 = \omega_1 + \omega_2$ in resonance with the cantilever natural frequency. Even though the required sensitivity could not be achieved with the current MFM and magnetic cantilevers, the resolution and sensitivity were increased. Furthermore, the measurement setup was refined to significantly reduce unwanted magnetic signals from currents and magnetic electrodes, and the validity of the operation and model of the method were validated. Improvements in electrostatic potential balancing and reduction of the noise level by increasing the quality factor of the cantilever should make the measurement possible.

Chapter 2

Theory of spin transport and decoherence

2.1 Single spin coherence time, spin dephasing, and spin relaxation times

The spin coherence time τ_s of an electron in a solid can be defined as follows. Let $|\chi_t\rangle$ represent the spin state of an electron at time t. Then τ_s is the minimum value of τ that satisfies

$$\lim_{t\to+\infty} \frac{1}{t} \int_0^t \langle \chi_{t'+\tau} | \chi'_t \rangle \, dt' = 0. \tag{2.1}$$

This condition just states that there should not be any correlation between $|\chi_t\rangle$ and $|\chi_{t+\tau}\rangle$ for $\tau \geq \tau_s$. Measuring τ_s in a real mesoscopic system is not as easy as it may seem. First, the sensitivity to measure the spin of a single electron in a mesoscopic system in a time short compared with the decoherence time has not been achieved. And second, it is difficult to tag one particular electron and distinguish it from the rest of the electron reservoir[1]. To get around these two problems, usually the spin of an ensemble of electrons is measured. By doing so, however, the electron-electron interactions that conserve the total spin of the electron system are disregarded [2].

[1] Quantum dots in semiconductor heterostructures have been used to confine one or a few electrons, separating them from the electron bath; but doing the same in a metallic system is an insurmountable task.

[2] Electron exchange interactions and the term in the electron dipole-dipole interaction which are of the form $\overrightarrow{S_1} \cdot \overrightarrow{S_2}$ conserve the expectation value of the total spin of the electrons $\langle \overrightarrow{S} \rangle$ and therefore are not accounted for in an ensemble measurement.

Therefore the ensemble coherence time τ_e is longer than the single spin coherence time τ_s. It is important now to make a distinction between measurements made in the presence or absence of a magnetic field. In the presence of a magnetic field there will be two different time scales that characterize the exponential approach to equilibrium of the average spin of the system. These are T_1 (the spin relaxation, longitudinal, or spin-lattice time) and T_2 (the spin dephasing, transverse, or decoherence time) which characterize the spin decay in directions parallel and perpendicular (respectively) to the external magnetic field [32, 33]. T_2 measures only the irreversible decoherence of the electronic spin while T_2^* also includes reversible dephasing between the spins of different electrons due to inhomogeneities in the magnetic field. Therefore in general $T_2^* \leq T_2$, but for conduction electrons $T_2^* = T_2$ is a very good approximation [34, 13]. These time scales, which were originally used in nuclear magnetic resonance but which have been adopted also for electron spin relaxation, are of course ensemble averages. One of the main objectives of this research is measuring T_2^*, which is equivalent to the time τ_e discussed above when dephasing is negligible. The other time scale, T_1, is usually much longer than T_2 and measures the rate of thermalization of the spin population rather than the coherence time. For T_1 processes, energy is transferred from the spin system to the lattice, usually by phonons. In the absence of an external magnetic field, or for small enough magnetic fields [3], and for isotropic systems, the longitudinal and transverse relaxation times are equal: $T_1 = T_2$, and they both measure the spin

[3]Small meaning that $\omega_L \tau_c << 1$ where ω_L is the Larmor precession frequency and τ_c is the correlation time (i.e. the typical time interval between spin changing events).

coherence time of an ensemble of electrons [32, 35, 36, 37]. The equality between the relaxation and dephasing times for weak magnetic fields can be understood by realizing that if the energy uncertainty introduced by the random fluctuations in the phase of the electron is larger than the Zeeman splitting between the two spin orientations, then the energy splitting is irrelevant for the dynamics, and the system is effectively isotropic. Therefore dephasing will affect equally the longitudinal and transverse components of the spin. Since the Larmor frequencies corresponding to the magnetic fields applied during the measurements were small compared with the inverse of the correlation time[3], $\omega_L \ll 1/\tau_c$, and since the material used was copper, a metal with an isotropic cubic crystal structure, then it is valid to assume $T_1 = T_2$, so throughout the rest of this thesis both the spin relaxation and spin dephasing times will be referred to with the symbol τ.

2.2 Spin relaxation mechanisms

The relevant sources of spin relaxation in metals are magnetic impurity scattering, the Elliot-Yafet, and the D'yakonov-Perel' mechanisms. Magnetic impurity scattering comes from the exchange interaction between the conduction electrons and a localized magnetic impurity. The Elliot-Yafet mechanism [5, 38] is based on the fact that in real crystals Bloch states are not eigenstates of spin, and so any non-magnetic (spin-independent) scattering leads to spin mixing and therefore spin relaxation. The D'yakonov-Perel' mechanism applies only to crystals that lack inversion symmetry. In such systems electrons in the same momentum state can have different energies for spin up and spin down. This can be understood by assuming

the reference frame of the electron, in which an effective magnetic field is produced by the moving charged lattice sites. Since the lattice lacks inversion symmetry, electrons moving in opposite directions will see magnetic fields of different magnitude so the average field seen by a randomly scattering electron is non-zero. For copper, which has a cubic lattice, the D'yakonov-Perel' mechanism is irrelevant and the only sources of relaxation are magnetic impurity scattering and Elliot-Yafet. These will be treated in more detail in the following sections. Other scattering mechanisms such as electron spin-spin and electron-nuclear spin give very long relaxation times in metals ($> \mu$s) [39] when compared with the Elliot-Yafet and magnetic impurity scattering, and will be ignored.

2.2.1 Elliot-Yafet

Conduction electron spins can relax through ordinary momentum scattering with phonons and impurities since eigenstates of spin are not eigenstates of the complete Hamiltonian of the system. The spin-orbit interaction introduces a term in the Hamiltonian of the form

$$V_{SO} = \frac{\hbar}{4m^2c^2}\nabla U \times \hat{\mathbf{p}} \cdot \hat{\sigma}, \tag{2.2}$$

where U is the spin-independent periodic potential of the lattice, $\hat{\mathbf{p}}$ is the momentum, and $\hat{\sigma}$ are the Pauli matrices. For metals with inversion symmetry the Bloch states for electrons with spin up and spin down with crystal momentum $\mathbf{k}$ and band index n are given by

$$\Psi_{\mathbf{k},n,\uparrow}(\mathbf{r}) = \left[a_{\mathbf{k},n}(\mathbf{r})|\uparrow\rangle + b_{\mathbf{k},n}(\mathbf{r})|\downarrow\rangle\right] e^{i\mathbf{k}\cdot\mathbf{r}}$$
$$\Psi_{\mathbf{k},n,\downarrow}(\mathbf{r}) = \left[a^*_{-\mathbf{k},n}(\mathbf{r})|\downarrow\rangle - b^*_{-\mathbf{k},n}(\mathbf{r})|\uparrow\rangle\right] e^{i\mathbf{k}\cdot\mathbf{r}}. \tag{2.3}$$

Since the spin-orbit coupling term is much smaller than the kinetic and potential terms of the Hamiltonian, it can be treated perturbatively. The value of the coefficient $b_{\mathbf{k},n}(\mathbf{r})$ is close to zero whereas that of $a_{\mathbf{k},n}(\mathbf{r})$ is close to one. Hence, even though the eigenstates of the full Hamiltonian have mixed spin, it still makes sense to talk about spin up and down, as those states with a majority of spin up or down. By itself, spin-orbit coupling does not cause spin relaxation. However, the presence of any kind of momentum scattering does. Since the non-diagonal elements of the scattering matrix with different spin indexes are non-zero, transitions between states with different spin are allowed and can occur every time there is some scattering event. This means that mechanisms that produce momentum relaxation such as phonons, impurities, and boundaries, will also produce spin relaxation. Elliot and Yafet showed that for negligible heavy impurity scattering the ratio of the momentum and spin relaxation times is given by a constant

$$a^p = \tau_p/\tau. \tag{2.4}$$

At high temperatures phonons are the main source of scattering. The temperature dependence of the spin relaxation time then follows the temperature dependence of the mean free time $1/T$, so the spin relaxation time has the same temperature

dependence as the conductivity. In the absence of any other scattering mechanism besides phonons, the spin relaxation time would also be proportional to the mean free time at low temperatures. Since in metals at low temperatures the resistivity behaves according to Bloch's law, $\rho \propto T^5$, the spin relaxation time should have a T^{-5} dependence. However, spin relaxation at low temperatures is caused mainly by the temperature independent impurity and boundary scattering. Therefore the spin relaxation time becomes temperature independent at low temperatures, making the observation of the T^{-5} behavior impossible up to now.

2.2.2 Magnetic impurity scattering

For dilute concentrations of magnetic impurities in a nonmagnetic host, the exchange interaction between the localized spin and the conduction electron spins creates an additional mechanism for spin relaxation and momentum scattering. When a conduction electron is scattered off a magnetic impurity, the spin of the electron is flipped, while the localized magnetic moment changes in order to compensate for the gained or lost magnetic moment of the electron. Since momentum is also affected in the magnetic scattering, this process contributes to the resistivity (Kondo effect) [40]. The temperature dependance of the Kondo resistivity is given by [41]

$$\rho_K = c\rho_M[1 - b\ln(T/T_K)], \tag{2.5}$$

where ρ_M is a measure of the strength of the exchange scattering, c is the magnetic impurity concentration, b depends on the ratio of the exchange and Fermi energies and on the crystal structure, and T_K is the Kondo temperature, which gives

the temperature where the Kondo resistivity becomes comparable to the phonon induced resistivity. The temperature dependence of the Kondo resistivity is rather different from the phonon resistivity, since it increases with decreasing temperature. The competing effects of the two resistivity mechanisms gives a minimum in the resistivity at a temperature which depends on the relative magnitude of phonon and magnetic impurity scattering. For Fe impurities in thin Cu films the Kondo temperature is of the order of 15^oK [42], and the Kondo effect is suppressed as the thickness of the film is decreased.

However, not every magnetic impurity causes Kondo behavior. For example Ni impurities in Cu do not, and Co impurities in Cu create a not very well defined magnetic moment which gives a quasi-Kondo temperature of 500^oK [43]-1000^oK [44]. However, Co atoms in the surface of Cu are considered to be a Kondo system [43] with a Kondo temperature of about 23^oK. Well above the Kondo temperature the main source of resistivity, and of spin relaxation, is due to phonons. However at 4.2^oK the main source of resistivity and spin relaxation is a combination of magnetic, nonmagnetic impurity scattering, and boundary scattering[4]. The relative magnitude of these effects depends on the magnetic and nonmagnetic impurity concentration, the spin orbit-coupling, and the grain boundary scattering. By using high purity nonmagnetic metals (5 ppm or less impurities), it is possible to significantly reduce the magnetic impurity scattering so at 4.2^oK the main source of resistivity and spin relaxation is boundary scattering [42].

[4]Specially important in films with grain structure.

Chapter 3
Spin Transport

In the previous chapter characteristic time scales for an ensemble of spins, such as the relaxation and the dephasing time, were defined, and the origins of spin relaxation and dephasing in metals with inversion symmetry was discussed. In this chapter I will discuss how to measure the spin relaxation time in metals by providing the basic theory for spin transport in one-dimension and by applying it to spin-valve devices with different geometries and different types of contacts. I will also discuss the effect of interfacial spin-flip scattering and small leakage currents. However, before going on to present the theory of spin transport, I will, as a motivation, describe and briefly explain the operation of a spin-valve device.

A typical spin-valve device is shown schematically in Fig. 3.1. The gray areas represent magnetic contacts, the black regions are normal metal wires, and the white regions are leads to inject or sink current and to measure voltages. The magnetic contacts serve as a source of spin-polarized electrons and also as a way of detecting the remaining magnetization of the injected spin-polarized electrons at a distance $L_1 + L_2$ from the injection point. In normal operation, a current is injected from one of the leads, say B_1, and the ground of the system is connected to lead B_N.

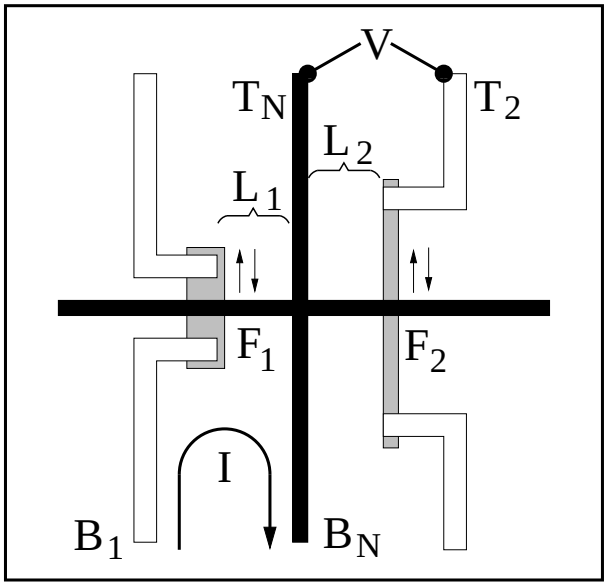

Figure 3.1: Schematic of a spin valve device showing magnetic contacts (gray), normal metal wires (black), and normal metal leads (white) for current transport and voltage measurement.

Due to the exchange splitting in ferromagnetic materials, spin up and spin down conduction electrons have different number densities and Fermi velocities, so the current injected from the magnetic contact labelled F_1 into the normal metal wire is spin-polarized. As the electrons travel along the normal wire between F_1 and the cross, and as they diffuse from the cross to F_2, part of the spin-polarization is lost due to spin relaxation. When they reach F_2 the spin-polarization of the electrons in the normal metal wire is different from that of the electrons in the magnetic contact F_2, so an electrochemical potential difference appears between the two metals. This potential difference can be observed by connecting leads at T_N and T_2. Depending on the relative alignment of the magnetization of F_1 and F_2 (injector and detector)[1],

[1]Which can be changed by applying an external magnetic field to selectively flip the magnetization of the injector or detector due to their different aspect ratios.

the measured potential is different. This measurement provides some information on the degree of injected spin-polarization and on the spin relaxation time. Details of the operation of the spin-valve will be addressed later in this section. Now the relevant theory for diffusive spin transport will be presented.

3.1 Spin transport: diffusion equation

In the absence of any momentum scattering mechanism (phonons, impurities, boundaries, other electrons, etc.), electrons in a crystal lattice are in Bloch states, eigenstates of the periodic lattice potential, and are able to transport charge without any resistance. In such a case transport is ballistic in any length scale. However in real systems at non-zero temperatures, in particular in mesoscopic systems where the length scales are of the order of tens or hundreds of nanometers and where single metallic crystals are difficult to grow, impurities, phonons, and boundaries prove to be effective momentum scattering mechanisms, so that the average time that an electron can travel without any scattering, the mean free time τ_c, is of the order of 10 fs[2]. For a fermi velocity of 10^6m/s this corresponds to a mean free path of the order of 10 nm. Therefore, from the point of view of the mean free path, a mesoscopic wire with a cross section of 50 nm by 100 nm is effectively three dimensional. Transport in metallic mesoscopic wires over distances of the order of a micron (typically much larger than the mean free path) is diffusive, which means that in a time t, electrons travel an average distance x given by

[2]Mesoscopic devices with long mean free times can be prepared, but for the particular devices fabricated for this research, and for typical mesoscopic devices found in the literature, mean free times of the order of 10 fs are typically observed.

$$x = \sqrt{Dt}, \tag{3.1}$$

after being scattered many times by phonons, impurities, and boundaries, where D is the diffusion constant given by

$$D = \frac{1}{3} V_F^2 \tau_c, \tag{3.2}$$

with V_F the Fermi velocity of electrons in the metal. In the Drude model the mean free time is related to the conductivity σ of the metal by $\sigma = ne^2\tau_c/m^*$ where n is the free electron density, e is the electron charge, and m^* the effective electronic mass. An alternative, more useful form of equation (3.2) is given by Einstein's relation [41]

$$D = \frac{\sigma}{e^2 N}, \tag{3.3}$$

where N is the density of states at the Fermi energy.

Typical spin relaxation times measured using methods like CESR (conduction electron spin resonance) [45, 46] or spin injection [3] are between tens of picoseconds and nanoseconds, although for high purity sodium at 10 K values as large as 1 μs have been measured [47]. Since the spin relaxation time is typically much larger than the mean free time, it is possible to define local distinct electron densities for spin up $n_\uparrow$ and spin down $n_\downarrow$. Even though there is no special direction that can define up and down, it is possible to choose any direction as the quantization axis. Starting from the Boltzmann transport equation and using the approximation of a

linear transport regime at zero temperature, it can be shown [10] that the current density $\mathbf{j}_\sigma$ for spin σ ($\sigma = \uparrow, \downarrow$) is given by

$$\mathbf{j}_\sigma = \sigma_\sigma \mathbf{E} - eD_\sigma \nabla \delta n_\sigma, \tag{3.4}$$

where σ_σ is the conductivity, $\mathbf{E}$ the electric field, D_σ the diffusion constant, and δn_σ the deviation from equilibrium of the local carrier density. The first term corresponds to Ohm's law while the second one is due to diffusion from high to low electron concentration. By definition, the density of states at the Fermi energy N_σ for each spin channel is $N_\sigma = \partial n_\sigma / \partial \epsilon_\sigma$ where ϵ_σ is the chemical potential. Replacing this, together with equation (3.3) into equation (3.4) gives

$$\mathbf{j}_\sigma = -\frac{\sigma_\sigma}{e} \nabla \mu_\sigma, \tag{3.5}$$

where the electrochemical potential μ_σ is defined as

$$\mu_\sigma = \epsilon_\sigma + e\phi, \tag{3.6}$$

where ϕ is the electric potential which produces the electric field $\mathbf{E}$. Due to relaxation, spin is not conserved. Therefore the continuity equation is given by

$$\nabla \cdot \mathbf{j}_\sigma + e\delta n_\sigma / \tau_\sigma = 0, \tag{3.7}$$

where τ_σ is the time for an electron to scatter out of state σ. From equation (3.7) it is possible to obtain the charge and spin continuity equations

$$\nabla \cdot (\mathbf{j}_\uparrow + \mathbf{j}_\downarrow) = 0 \tag{3.8}$$

$$\nabla \cdot (\mathbf{j}_\uparrow - \mathbf{j}_\downarrow) = -e(\delta n_\uparrow/\tau_\uparrow - \delta n_\downarrow/\tau_\downarrow). \tag{3.9}$$

By replacing $\mathbf{j}_\sigma$ from equation (3.5) into equations (3.8) and (3.9) and using the detailed balance principle $N_\uparrow/\tau_\uparrow = N_\downarrow/\tau_\downarrow$ [48, 49], which states that the scattering rates for spin $\uparrow$ and spin $\downarrow$ are equivalent at equilibrium, we obtain [26][3]

$$\nabla^2(\sigma_\uparrow\mu_\uparrow + \sigma_\downarrow\mu_\downarrow) = 0 \tag{3.10}$$

$$\nabla^2(\mu_\uparrow - \mu_\downarrow) = \lambda^{-2}(\mu_\uparrow - \mu_\downarrow), \tag{3.11}$$

with the spin diffusion length λ related to the spin relaxation time

$$\tau = 2\left(\frac{1}{\tau_\uparrow} + \frac{1}{\tau_\downarrow}\right)^{-1}, \tag{3.12}$$

and the diffusion constant

$$D = \frac{(N_\uparrow + N_\downarrow)D_\uparrow D_\downarrow}{N_\uparrow D_\uparrow + N_\downarrow D_\downarrow}, \tag{3.13}$$

in the usual way, i.e. $\lambda = \sqrt{D\tau}$. In the case of normal metals $N_\uparrow = N_\downarrow = N/2$, $D_\uparrow = D_\downarrow = D$, $\sigma_\uparrow = \sigma_\downarrow = \sigma/2$, and $\tau_\uparrow = \tau_\downarrow = \tau$.

[3] Although the derivation of Takahashi [26] was followed, it agrees with Valet and Fert [10] and Jedema [49] except for the definition of τ, which was incorrect in [49].

3.1.1 Spin transport in one dimension

For spin diffusion in one dimension (say in the x direction) the most general solution to equations (3.10) and (3.11) is

$$\mu_\sigma = a + bx \pm \frac{c}{\sigma_\sigma} e^{-x/\lambda} \pm \frac{d}{\sigma_\sigma} e^{x/\lambda}, \tag{3.14}$$

where the positive sign is for $\sigma =\uparrow$ and the negative sign for $\sigma =\downarrow$, and a, b, c, and d are still unspecified coefficients. This solution is valid for both magnetic and non-magnetic metallic regions. The first two terms on the right hand side of equation (3.14) are the same for both spin channels. They represent a reference potential energy plus a linear (in x) potential energy coming from the electric field that drives the current. In the absence of charge current the second term vanishes. The last two terms on the right hand side of equation (3.14) have different sign and magnitude for the different spin channels and they show the exponential decrease or increase in the electrochemical potential as a function of position. In order to find the values of the coefficients it is necessary to specify the particular geometry of the device and a set of boundary conditions. This will be done in the following sections.

3.1.2 Interfacial spin transport

The previous sections presented the formalism for describing diffusive spin transport in metals. However, no reference was made to transport across interfaces, which is critical for the injection and detection of spin, as explained at the beginning of this chapter (see Fig. 3.1). Therefore the issue of interfacial spin transport will be

addressed in this section.

A complete understanding of the microscopic details of spin transport across interfaces is lacking. Even though specific details of the interface seem to be relevant, first principle calculations are incomplete, and it is necessary to use phenomenological parameters and make assumptions with no a-priori justification, which can be validated only if the predictions agree with the measurements. Here the same phenomenological approach will be taken. It is usually assumed [10, 22, 50, 51] that the spin-flip scattering at the interface is irrelevant. This assumption will be used for the most part of this chapter but it will be relaxed in section 3.5.1 where the effects of interface spin-flip scattering will be studied. If this assumption holds, the spin-dependent current must be conserved at each interface. This defines the first boundary condition for the electrochemical potential. In addition, the interface between two metals can be either transparent or resistive (non-transparent). Transparent contacts are defined as those in which the electrochemical potential is continuous across the interface. Resistive contacts, on the other hand, are those in which the difference in electrochemical potential between the two sides of the interface is equal to the product of the spin-dependent resistance R_σ and the spin-dependent current $j_\sigma A$ that crosses the interface:

$$\mu_\sigma^N - \mu_\sigma^F = R_\sigma j_\sigma A, \tag{3.15}$$

where A is the area of the contact, and F and N label ferromagnetic and normal

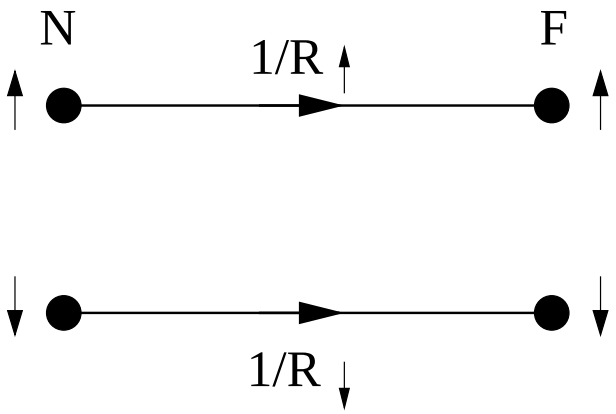

Figure 3.2: Schematic of the transport across a nonmagnetic-ferromagnet interface in the case of conserved spin. The two transport channels (spin ↑ and spin ↓) and their associated interface resistances are shown.

regions of the device.[4] This sets the second boundary condition for the electrochemical potential. A schematic of the spin conserved transport at the interface is shown in Fig. 3.2 for aligned injector and detector. The dots on the left represent the nonmagnetic metal while the ones on the right represent the ferromagnetic metal. The two possible transport channels (spin ↑ and spin ↓) are shown, together with their associated interface resistance. Different interface resistances for spin up and spin down are due to the exchange splitting in the ferromagnetic region, which leads to spin-dependent Fermi wave vectors, transmission coefficients, and density of states. The remaining boundary condition is that the electrochemical potential be finite as $x \rightarrow \pm\infty$. This three boundary conditions, together with information on the geometry of the spin-valve, are enough to find the coefficients that specify the exact functional form of the electrochemical potential in every region of the device.

[4]Only $F - N$ contacts will be studied since they are essential for spin injection and detection (see Fig. 3.1).

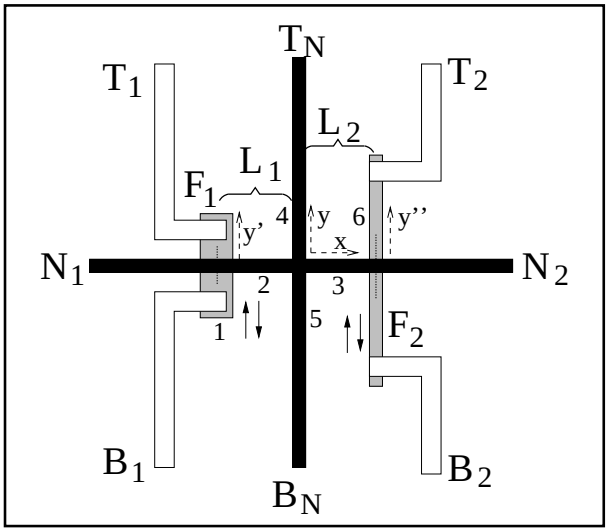

Figure 3.3: Schematic of a spin valve device with magnetic contacts (gray), normal metal wires (black), and normal metal leads (white) for current transport and voltage measurement, in the cross geometry configuration.

3.2 Spin valve structures

Several geometries of spin-valve devices were fabricated and different measurement configurations were used. They can be divided into two different kinds: cross geometry and nonlocal geometry. In the following sections I will solve the equations for the electrochemical potential for the two different configurations, and calculate relevant quantities such as the spin-related resistance and the contact resistance, which are the quantities that can be observed experimentally.

3.2.1 Cross geometry

The cross geometry configuration is shown in Fig. 3.3. The black regions are made of a nonmagnetic metal, the white regions are non-magnetic leads for probing the system, and the gray areas are the ferromagnetic contacts. F_1 and F_2 label each

of the two magnetic regions, L_1 and L_2 give the distances between the cross and each of the magnetic contacts, while the remaining capital letters label leads that are available experimentally. The two ferromagnetic contacts are elongated in the vertical direction (along the y axis) to facilitate alignment of the magnetization in this direction. Therefore the vertical axis is called the easy geometrical axis. Additionally, the ferromagnetic contacts have different aspect ratios to ensure different coercive fields, and hence allow independent rotation of the magnetization of each contact with an applied external field. The active part of the device, in which spin injection and detection takes place, is composed of the black and gray regions, which can be divided into six different sections numbered in Fig. 3.3. Region 1 is the lower half of F_1, regions 2-5 are the different arms of the cross, with regions 2 and 3 extending from the middle of the cross to the vertical black lines at the centers of F_1 and F_2 respectively, and region 6 is the upper half of F_2. The dashed black lines with arrow heads indicate the coordinate systems that will be used. Region 1 is along $-y'$, region 2 along $-x$, region 3 along x, region 4 along y, region 5 along $-y$, and region 6 along y''.

Spin injection and detection experiments are performed by injecting current into lead B_1, grounding lead B_N so that all the charge current is drained through this lead, and measuring the potential difference between leads T_N and T_2, between which no charge current circulates [5]. In such a configuration, the equations for the

[5]This is not exactly true since as the current flows through the cross, a measurable ohmic voltage appears between leads T_N and T_2. However, this voltage is independent of the magnetization direction of the magnetic contacts and can therefore be distinguished from the spin signal.

electrochemical potentials in the six different regions described above are

$$\mu_{1\sigma}(y') = a_1 - \frac{je}{\sigma_F}y' \pm \frac{d_1}{\sigma_\sigma}\exp\frac{y'}{\lambda_F}$$

$$\mu_{2\sigma}(x) = a_2 - \frac{je}{\sigma_N}x \pm \frac{c_2}{\sigma_N}\exp\frac{-x}{\lambda} \pm \frac{d_2}{\sigma_N}\exp\frac{x}{\lambda}$$

$$\mu_{3\sigma}(x) = a_3 \pm \frac{c_3}{\sigma_N}\exp\frac{-x}{\lambda} \pm \frac{d_3}{\sigma_N}\exp\frac{x}{\lambda}$$

$$\mu_{4\sigma}(y) = \pm\frac{c_4}{\sigma_N}\exp\frac{-y}{\lambda}$$

$$\mu_{5\sigma}(y) = a_5 + \frac{je}{\sigma_N}y \pm \frac{d_5}{\sigma_N}\exp\frac{y}{\lambda}$$

$$\mu_{6\sigma}(y'') = a_6 \pm \frac{c_6}{\sigma_\sigma}\exp\frac{-y''}{\lambda_F}, \tag{3.16}$$

with $\sigma_F = \sigma_\uparrow + \sigma_\downarrow$ and σ_N the conductivities of the ferromagnet (F) and normal metal (N), λ_F and λ the spin relaxation lengths in (F) and (N), j the current density, and where the positive (negative) sign is for $\sigma = \uparrow$ ($\sigma = \downarrow$). Charge current conservation has been used to solve for the coefficient of the linear term in the electrochemical potential, assuming equal cross sectional areas for all the regions[6]. Since the potential is specified up to a constant, the constant term in the electrochemical potential for the lead labelled T_N (region 4 in Fig. 3.3) was set to zero. The condition of finite electrochemical potentials at $y' \to -\infty$, $y \to \pm\infty$, and $y'' \to \infty$, simplified the original equations by removing the exponentially divergent terms. Conservation of spin current, which has not been used yet, gives the following set of boundary conditions, one for each of the three points at which different regions meet[7]:

[6]This assumption can be relaxed and the case of different cross sectional areas for F_1, F_2, and N can be obtained by multiplying the second term in the first one of equations (3.16) by A_N/A_F, the ratio of the cross sections of the normal metal wire and the ferromagnetic contact F_1.

[7]Again for equal cross sectional areas.

$$-\mu'_{1\uparrow}(0)\sigma_\uparrow + \mu'_{2\uparrow}(-L_1)\sigma_N/2 = 0$$

$$-\mu'_{2\uparrow}(0) + \mu'_{3\uparrow}(0) + \mu'_{4\uparrow}(0) - \mu'_{5\uparrow}(0) = 0$$

$$-\mu'_{3\uparrow}(L_2)\sigma_N/2 + \mu'_{6\uparrow}(0)\sigma_\uparrow = 0, \tag{3.17}$$

where μ' is the derivative of the electrochemical potential. The most relevant coefficient in equations (3.16) is a_6 which gives the potential at lead T_2 far away from the active region of the device. The measured signal, as explained above, is the voltage V between leads T_N and T_2 which is given by

$$eV = \mu_4(y \to \infty) - \mu_6(y'' \to \infty) = -a_6. \tag{3.18}$$

Cross geometry spin valve with transparent contacts

In the case of transparent contacts, the additional boundary conditions are the continuity of the electrochemical potentials for both channels:

$$\mu_{1\sigma}(0) - \mu_{2\sigma}(-L_1) = 0$$

$$\mu_{2\sigma}(0) = \mu_{3\sigma}(0) = \mu_{4\sigma}(0) = \mu_{5\sigma}(0)$$

$$\mu_{3\sigma}(L_2) - \mu_{6\sigma}(0) = 0. \tag{3.19}$$

Equations (3.17) and (3.19) are valid for the case of aligned injector F_1 and detector F_2. However, if they are anti-aligned, the direction of the majority spin for F_1 will be the same as the direction for the minority spin of F_2. This means that to obtain

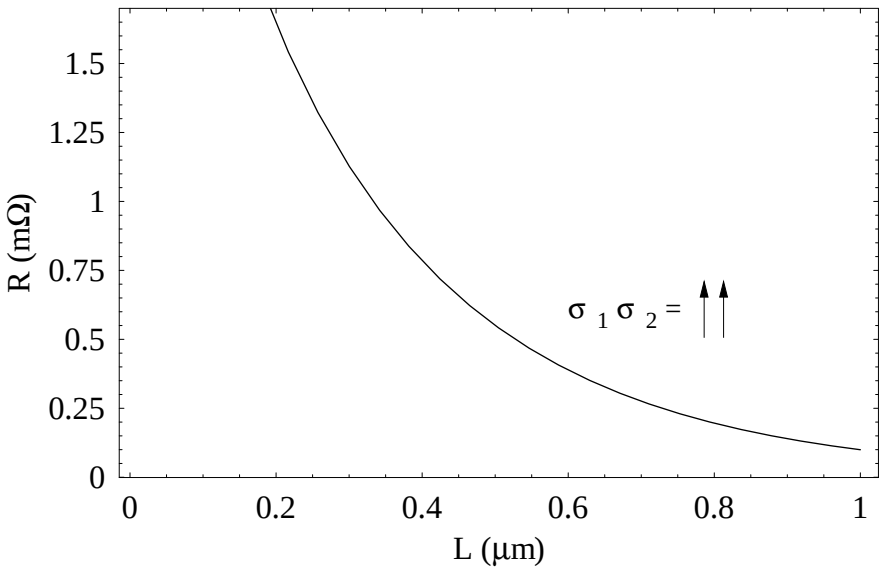

Figure 3.4: Resistance given by equation (3.20) as a function of separation L between magnetic contacts for $\sigma_1\sigma_2 = \uparrow\uparrow$ (aligned magnetizations of F_1 and F_2).

the correct boundary conditions in the case of anti-aligned magnetic contacts, the indexes $\uparrow$ and $\downarrow$ in equations (3.17) and (3.19) have to be reversed for either F_1 or F_2. The solution to equations (3.16) with boundary (matching) conditions (3.17) and (3.19) in the case of $L_1 = L_2 = L/2$ gives an observable voltage V (3.18) which can be normalized by the injected current to obtain the spin related resistance

$$R = \pm \frac{\alpha_F^2 \lambda}{\sigma_N A(1+\gamma(1-\alpha_F^2))[1-\gamma(1-\alpha_F^2)+\exp(L/\lambda)(1+\gamma(1-\alpha_F^2))]}, \quad (3.20)$$

where $\sigma_F = \sigma_\uparrow + \sigma_\downarrow$, $\alpha_F = (\sigma_\uparrow - \sigma_\downarrow)/\sigma_F$, $\gamma = \lambda\sigma_F/(\lambda_F\sigma_N)$, A is the cross sectional area of the wires [8], and the positive (negative) sign is for aligned (anti-aligned) magnetizations of F_1 and F_2. Figure 3.4 shows the behavior of the resistance given by equation (3.20) as a function of L for typical values of the relevant parameters for

[8] Again in the case of regions with equal cross sectional area.

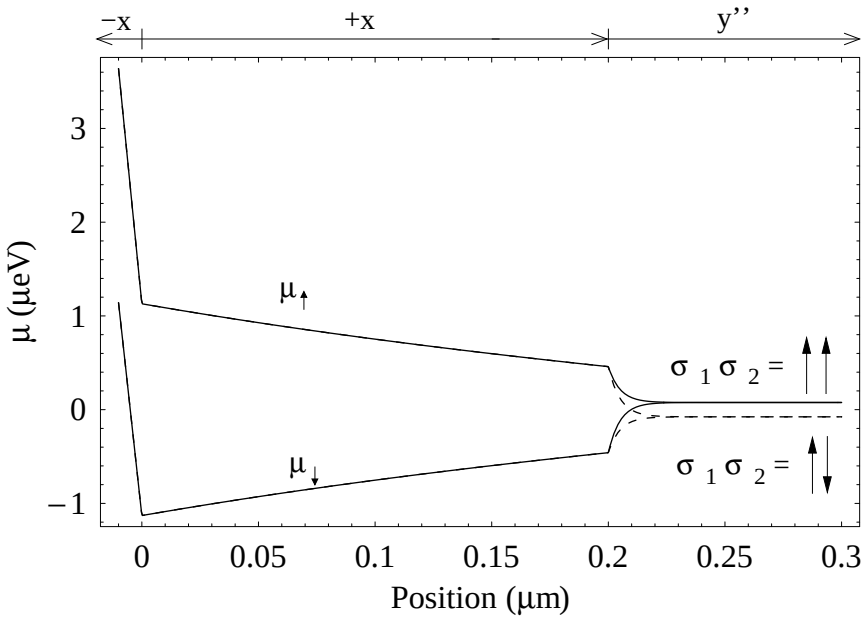

Figure 3.5: Electrochemical potential for both spin channels and both aligned (solid line) and anti-aligned (dashed line) magnetizations of F_1 and F_2.

Cu. It shows that the spin-related resistance decays with L, so that measurements of R for different values of L can give information about the relaxation length of electronic spin in the normal metal.

The behavior of the electrochemical potential as a function of position for fixed $L_1 = L_2 = L/2$ =0.2 μm is shown in Fig. 3.5 for both spin channels and both aligned ($\sigma_1\sigma_2 = \uparrow\uparrow$, solid line) and anti-aligned ($\sigma_1\sigma_2 = \uparrow\downarrow$, dashed line) magnetizations of F_1 and F_2. The solid and dashed lines coincide throughout F_1 and N but they differ in F_2. The axes at the top delimit regions 2 (-0.2 μm$< x < 0$), 3 ($0 < x < 0.2$ μm), and 6 ($y'' > 0.2$ μm) as defined in Fig. 3.3. The difference in electrochemical potentials (ECP's) between the two configurations $\uparrow\uparrow$ and $\uparrow\downarrow$ in the region in F_2 where the spin has relaxed completely is the measurable signal, equal to twice the potential V

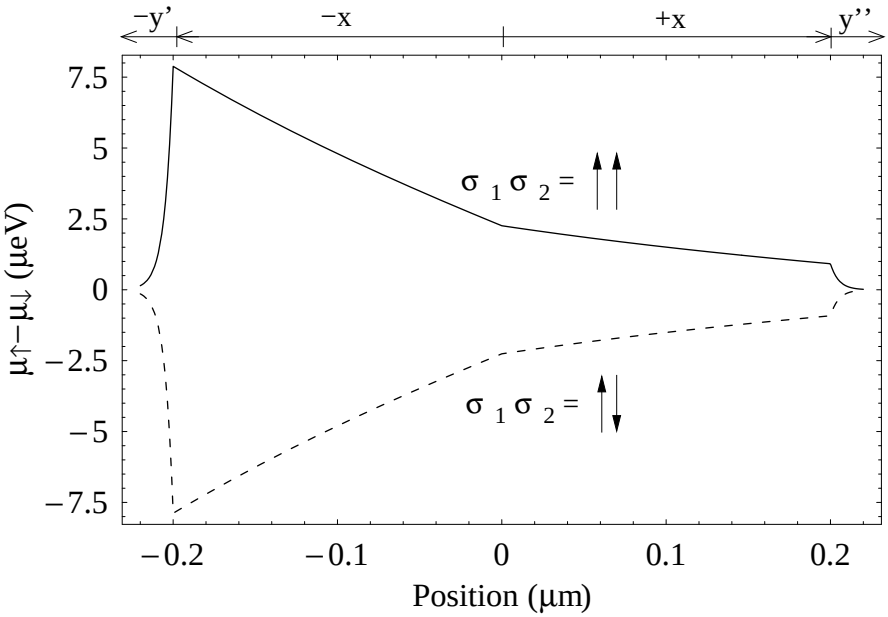

Figure 3.6: Spin component of the electrochemical potential for aligned (solid line) and anti-aligned (dashed line) magnetizations of F_1 and F_2.

[see equation (3.18)] in units of eV. The ohmic potential drop in region 2 (see Fig. 3.3) can be seen as a line with large negative slope for both spin channels. The slow change of the ECP in region 3 and the fast change in region 4 is due to the much larger relaxation length in nonmagnetic metals than in ferromagnetic ones.

The ECP's shown in Fig. 3.5 contain both spin and charge effects. The spin effects can be isolated by calculating the spin electrochemical potential (SECP) which is the difference in the ECP of both spin channels, $\mu_\uparrow - \mu_\downarrow$ as shown in Fig. 3.6 for both aligned (solid line) and anti-aligned (dashed line) magnetizations of F_1 and F_2. The axes at the top delimit regions 1 (y' <-0.2 μm), 2 (-0.2 μm< x < 0),3 (0 < x < 0.2 μm), and 6 (y'' > 0.2 μm) defined in Fig. 3.3. Far inside F_1, the component of the electrochemical potential related to spin (SECP) is zero, since

the spin population is in equilibrium. However, since spin is being injected into the normal metal, there is a large non-equilibrium spin population at the F_1-N interface which manifests as a large SECP. Back-diffusion of the electrons into the injector also increases the SECP for a short distance of the order of the spin relaxation length in the magnetic material λ_F. As electrons are transported to the cross (Fig. 3.3) by the current flow, spin relaxation decreases the degree of spin polarization and therefore the SECP. At the cross the charge current flows in a different direction and the spin polarization can only be transported to region 3 by the diffusive motion of electrons. Hence the SECP decreases at a smaller rate. Finally, the residual non-equilibrium spin population at the $F_2 - N$ interface diffuses a distance λ_F into F_2 and the SECP decays to zero.

Cross geometry spin valve with non-transparent contacts

In the case of non-transparent contacts the electrochemical potential is no longer continuous at the $F-N$ interfaces so equations (3.19) have to be modified to include the spin-dependent contact resistances $R_{1\sigma}$ and $R_{2\sigma}$ (for contacts F_1-N and F_2-N defined in equation [3.15]) as follows:

$$\begin{aligned}
\mu_{1\sigma}(0) - \mu_{2\sigma}(-L_1) &= -\mu'_{2\sigma}(-L_1)A_{c1}R_{1\sigma}\sigma_N/2 \\
\mu_{2\sigma}(0) = \mu_{3\sigma}(0) &= \mu_{4\sigma}(0) = \mu_{5\sigma}(0) \\
\mu_{3\sigma}(L_2) - \mu_{6\sigma}(0) &= -\mu'_{3\sigma}(L_2)A_{c2}R_{2\sigma}\sigma_N/2, \qquad (3.21)
\end{aligned}$$

where A_{c1} and A_{c2} are the contact areas for each of the two $F-N$ contacts, and μ'

is the derivative of the electrochemical potential. In this case the complete solution is long and not very enlightening so its transcription has been avoided. However, in the limit of large $R_{1\sigma}$ and $R_{2\sigma}$ compared to the resistance of each material (F, N) over its spin relaxation length, the measurable spin-related resistance is found to be

$$R = \pm \frac{\lambda P_1 P_2}{A\sigma_N[\exp(L/\lambda) + \cosh((L_1 - L_2)/\lambda)]}, \tag{3.22}$$

where $L = L_1 + L_2$ is the total separation between magnetic contacts, $A = A_{c1} = A_{c2}$, the positive (negative) sign is for aligned (anti-aligned) magnetizations of F_1 and F_2, and

$$P_i = \frac{R_{i\downarrow} - R_{i\uparrow}}{R_{i\downarrow} + R_{i\uparrow}}, \tag{3.23}$$

for $i = 1, 2$. Furthermore, P_1 can be interpreted as the spin current polarization injected into the normal metal defined as

$$P_1 = \frac{j_{1\uparrow} - j_{1\downarrow}}{j_{1\uparrow} + j_{1\downarrow}}, \tag{3.24}$$

where $j_{1\uparrow}$ and $j_{1\downarrow}$ are the current densities for spin up and spin down at the F_1-N interface. The equivalence between equations (3.23) for $i = 1$ and (3.24) is obtained by explicitly calculating the spin dependent current densities $j_{1\sigma}$ using the same set of equations for the electrochemical potential and boundary conditions that led to equation (3.22). On the other hand, P_2 cannot be interpreted directly as the spin current polarization at the detector: since no charge current flows across the N-F_2 interface, the spin current polarization at the detector would be infinite. However,

it will be shown in chapter 5 that P_2 contains important physical information of the ratio of spin polarized transport to total transport across the detector interface. Therefore the P_i are not simply a convenient ratio of the resistances, but also provide information about the degree of spin-polarized transport across each of the interfaces. The degree of spin polarization is set then, not by the interplay of the resistivity and the spin relaxation lengths of the metals, but instead by the values of the spin-dependent contact resistances. This means that choosing an appropriate magnetic material, which defines the exchange splitting and therefore the density of states at the Fermi energy, and choosing the resistive barrier between the F and N materials, which changes the tunnelling probabilities, is essential for maximizing spin injection. Figures 3.7 and 3.8 show respectively the electrochemical potential and the spin electrochemical potential for aligned (solid line) and anti-aligned (dashed line) magnetizations of F_1 and F_2, for spin current polarizations $P_1 = P_2 = P$ of (a) 5%, (b) 10%, and (c) 20% for a constant contact resistance of 5 Ω. The spin-related resistance (proportional to the difference between the solid and dashed lines at the right of each of Figs. 3.7), as well as the magnitude of the chemical potentials, clearly increase with P. However, more information can be extracted by looking at the SECP in Fig. 3.8. The spin signal again increases in magnitude with increasing P, but there are some additional important features to be noticed. In the extreme case of P=0 (not shown here), equal number of electrons with spin up and spin down cross the interface. Since F_1 has, in equilibrium, more electrons with spin up than spin down, the ratio between spin up and spin down electrons is increased,

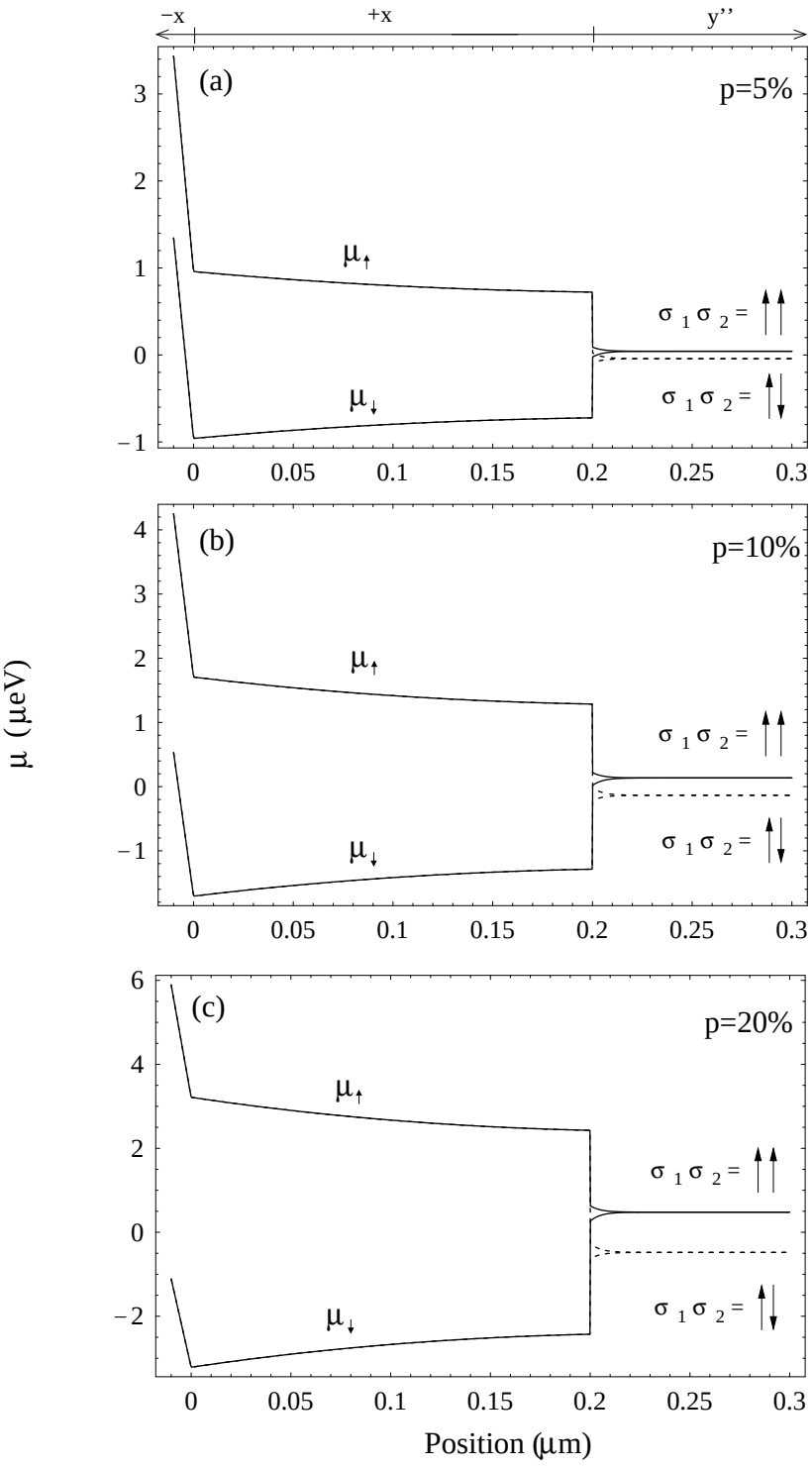

Figure 3.7: Electrochemical potential for both spin channels and both aligned (solid line) and anti-aligned (dashed line) magnetizations of F_1 and F_2 for spin current polarizations $P_1 = P_2 = P$ of (a) 5%, (b) 10%, and (c) 20% for a contact resistance of 5 Ω.

producing an enhancement in the SECP (directly related to the magnetization) in F_1 close to the interface. This effect is seen in Fig. 3.8(a). The value of P is only 5% so only a few more electrons with spin up than electrons with spin down cross the interface, effectively increasing the ratio of spin up to spin down electrons in F_1, producing the "spike" at x =-0.2μm. In (b) this is less evident since P is higher so more electrons with spin up are leaving F_1, and in (c), for P =20%, the effect has now reversed, showing that, compared with the number of electrons with spin down, the number of electrons with spin up that leave F_1 is so large that the ratio of electrons with spin up to electrons with spin down left in F_1 decreases below the equilibrium value, giving a dip in the SECP at the interface. This reversal occurs when the spin current polarization at the injector interface P is equal or larger than the spin current polarization of the magnetic material P_M. For the simulations shown in Figs. 3.7 and 3.8 the value P_M =16.7% has been used[9]. Another important observation is that for P=5% the injected spin polarization is small so not many electrons can pile up in the right hand side of the injector interface (x=-0.2μm+ϵ), or equivalently, the magnetization diffuses from the interface towards the right at a faster rate than the maximum injection rate of F_1. This is different for P=10%, where the spin polarized electrons pile up at the interface, acting as an additional impedance for injection. In this case the rate at which the magnetization diffuses to the right is smaller than the maximum rate of injection. This is known as spin bottle-neck.

[9]Even though Giant Magneto Resistance (GMR) measurements give values for P_M as high as 50% for Co [52], much smaller values have also been measured [49].

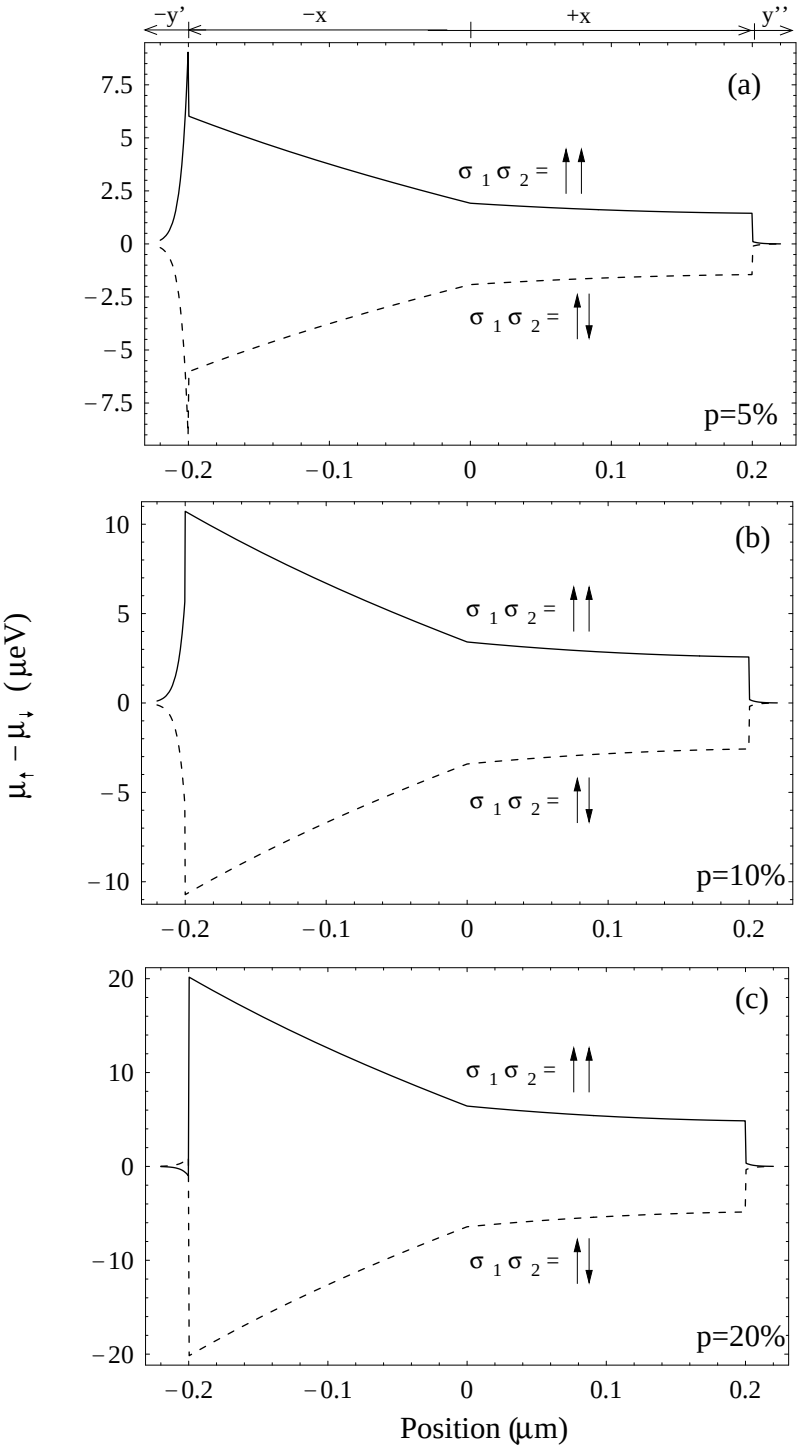

Figure 3.8: Spin electrochemical potential for both aligned (solid line) and anti-aligned (dashed line) magnetizations of F_1 and F_2 for spin current polarizations $P_1 = P_2 = P$ of (a) 5%, (b) 10%, and (c) 20% for a contact resistance of 5 Ω.

3.2.2 Nonlocal geometry

The geometry discussed in the previous section has the drawback that voltages which are not spin-related appear at the measuring leads, and that a large part of the spin polarized electrons diffuse into the vertical arms of the cross, decreasing the measured signal. To avoid these problems, the nonlocal configuration shown in Fig. 3.9 is preferred. For this type of geometry the current is injected through lead B_1 while lead N_1 is grounded so all the current is sinked this way. The voltage difference between leads T_2 and N_2 is measured. The ratio of the measured nonlocal voltage to the injected current is the nonlocal resistance R. The nonlocal character of the measurements comes from the fact that any effect produced by spin comes from purely diffusive transport of the magnetization (spin) without any accompanying charge current, and in the absence of spin effects the measured voltage would be

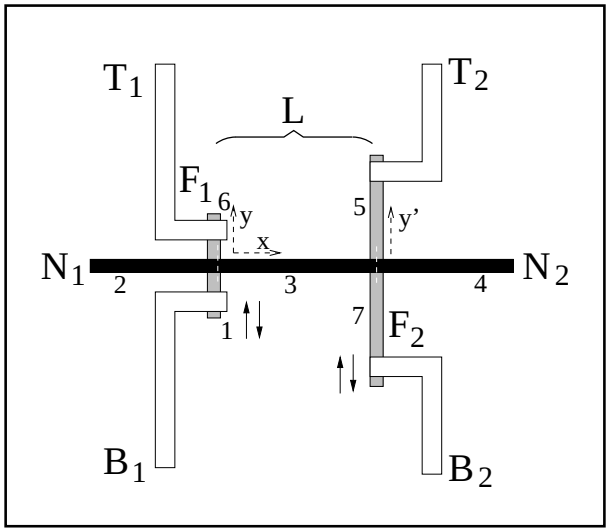

Figure 3.9: Schematic of a spin valve device for nonlocal measurements. Gray regions represent the magnetic contacts, black ones the normal metal wire, and white regions the connecting leads.

zero. In other words, spin current flows in regions 3, 4, 5, 6, and 7, but no charge current flows in such regions, so spurious effects like anisotropic magnetoresistance or Hall effect cannot affect the measurement. The procedure for finding the relevant equations is very similar to that described in the last section for the cross geometry, so details will not be mentioned.

For this geometry the equations for the electrochemical potential [see equation (3.14)] are

$$\begin{aligned}
\mu_{1\sigma}(y) &= a_1 - \tfrac{Ie}{\sigma_F A_{F1}} y \pm \tfrac{d_1}{\sigma_\sigma} \exp \tfrac{y}{\lambda_F} \\
\mu_{2\sigma}(x) &= a_2 + \tfrac{Ie}{\sigma_N A_N} x \pm \tfrac{d_2}{\sigma_N} \exp \tfrac{x}{\lambda} \\
\mu_{3\sigma}(x) &= a_3 \pm \tfrac{c_3}{\sigma_N} \exp \tfrac{-x}{\lambda} \pm \tfrac{d_3}{\sigma_N} \exp \tfrac{x}{\lambda} \\
\mu_{4\sigma}(x) &= \pm \tfrac{c_4}{\sigma_N} \exp \tfrac{-y}{\lambda} \\
\mu_{5\sigma}(y') &= a_5 \pm \tfrac{c_5}{\sigma_\sigma} \exp \tfrac{-y'}{\lambda_F} \\
\mu_{6\sigma}(y) &= a_6 \pm \tfrac{c_6}{\sigma_\sigma} \exp \tfrac{-y}{\lambda_F} \\
\mu_{7\sigma}(y') &= a_7 \pm \tfrac{d_7}{\sigma_\sigma} \exp \tfrac{y'}{\lambda_F},
\end{aligned} \tag{3.25}$$

where charge current conservation has been used to find the coefficients of the linear terms, I is the injected current, and A_{F1} and A_N are the cross sectional areas of $F1$ and N. The potential in region 4, far away from the active area of the device, was chosen as zero so that the measurable nonlocal resistance R is

$$R = \frac{\mu_5(y' \to \infty) - \mu_4(x \to \infty)}{Ie} = \frac{a_5}{Ie}. \tag{3.26}$$

Since the chemical potential is continuous in regions made of the same material, it is clear from equations (3.25) that $a_6 = a_1$, $c_6 = d_1$ $a_7 = a_7$, and $d_7 = c_5$. For aligned magnetic contacts the continuity in the spin current at the $F_1 - N$ and $F_2 - N$ interfaces implies

$$\begin{aligned} -\mu'_{1\uparrow}(0)\sigma_\uparrow A_{F1} - \mu'_{2\uparrow}(0)\sigma_N/2A_N + \mu'_{3\uparrow}(0)\sigma_N/2A_N = 0 \\ -\mu'_{3\uparrow}(L)\sigma_N/2A_N + \mu'_{5\uparrow}(0)\sigma_\uparrow A_{F2} + \mu'_{4\uparrow}(L)\sigma_N/2A_N = 0, \end{aligned} \tag{3.27}$$

where A_N, A_{F1}, and A_{F2} are the cross sectional areas for the normal metal and ferromagnetic contacts F_1 and F_2, and μ' is the derivative of the electrochemical potential. For anti-aligned magnetic contacts the spin index for either regions 1 and 6 or regions 5 and 7 should be reversed.

Nonlocal geometry spin valve with transparent contacts

For transparent contacts the electrochemical potential (ECP) is continuous therefore the last set of boundary conditions for aligned magnetizations of F_1 and F_2 is

$$\begin{aligned} \mu_{1\sigma}(0) = \mu_{2\sigma}(0) = \mu_{3\sigma}(0) \\ \mu_{3\sigma}(L) = \mu_{4\sigma}(L) = \mu_{5\sigma}(0). \end{aligned} \tag{3.28}$$

In the case of anti-aligned magnetizations of F_1 and F_2 the spin index for either region 1 or region 5 should be reversed. By applying the conditions (3.27) and (3.28) to equations (3.25), the nonlocal resistance is found to be

$$R = \pm \frac{2R_N \exp(-L/\lambda)(\frac{\alpha_F R_{F1}/R_N}{1-\alpha_F^2})(\frac{\alpha_F R_{F2}/R_N}{1-\alpha_F^2})}{(1+\frac{2R_{F1}/R_N}{1-\alpha_F^2})(1+\frac{2R_{F2}/R_N}{1-\alpha_F^2}) - \exp(-2L/\lambda)}, \tag{3.29}$$

where $R_{F1} = \lambda_F/(2\sigma_F A_{F1})$, $R_{F2} = \lambda_F/(2\sigma_F A_{F2})$, $R_N = \lambda/(\sigma_N A_N)$, and the positive (negative) sign is for aligned (anti-aligned) magnetizations of F_1 and F_2. The factors of 2 in the definition of R_{F1} and R_{F2} come from the existence of the additional regions 6 and 7 (which had been ignored in previous analysis [26]).

Nonlocal geometry spin valve with non-transparent contacts

In the case of resistive contacts the boundary conditions for the ECP are

$$\begin{aligned}
\mu_{1\sigma}(0) - \mu_{3\sigma}(0) &= -\mu'_{1\sigma}(0) A_{c1} R_{1\sigma}\sigma_\sigma \\
\mu_{2\sigma}(0) &= \mu_{3\sigma}(0) \\
\mu_{3\sigma}(L) &= \mu_{4\sigma}(L) \\
\mu_{3\sigma}(L) - \mu_{5\sigma}(0) &= -\mu'_{5\sigma}(L) A_{c2} R_{2\sigma}\sigma_\sigma,
\end{aligned} \tag{3.30}$$

where A_{c1} and A_{c2} are the junction areas of the contacts $F_1 - N$ and $F_2 - N$, and μ' is the derivative of the electrochemical potential. In the case of anti-aligned magnetizations of F_1 and F_2 the spin index for either region 1 or region 5 should be reversed. By applying conditions (3.27) and (3.30) to equations (3.25), the nonlocal resistance is found to be

$$R = \pm \frac{2R_N \exp(-L/\lambda)(\frac{P_1 R_{c1}}{R_N(1-P_1^2)} + \frac{\alpha_F R_{F1}}{R_N(1-\alpha_F^2)})(\frac{P_2 R_{c2}}{R_N(1-P_2^2)} + \frac{\alpha_F R_{F2}}{R_N(1-\alpha_F^2)})}{(1+\frac{2R_{c1}}{R_N(1-P_1^2)} + \frac{2R_{F1}}{R_N(1-\alpha_F^2)})(1+\frac{2R_{c2}}{R_N(1-P_2^2)} + \frac{2R_{F2}}{R_N(1-\alpha_F^2)}) - \exp(-2L/\lambda)}, \tag{3.31}$$

where R_{cj} $(j = 1, 2)$ is given by

$$R_{cj} = \frac{A_{cj}}{A_{Fj}(\frac{1}{R_{j\uparrow}} + \frac{1}{R_{j\downarrow}})}. \tag{3.32}$$

It can be seen that in the limit of transparent contacts, $R_{c1} = R_{c2} = 0$, equation (3.29) is recovered. In the opposite limit of contact resistance much larger than the resistance of the ferromagnetic and normal metals over their spin relaxation length, more precisely when

$$R_{cj} >> R_{Fj}, R_N \tag{3.33}$$

for $j = 1, 2$, equation (3.31) reduces to

$$R = \pm\frac{1}{2}P_1P_2R_N \exp(-L/\lambda), \tag{3.34}$$

where the positive (negative) sign is for aligned (anti-aligned) magnetizations of F_1 and F_2. This equation takes into account the effect of all the electrons that diffuse from injector to detector in time $t < \infty$. However, it is also useful to consider the effect of only those electrons which diffuse from injector to detector in exactly a time t. This is given by

$$R_D(t) = \pm\frac{1}{2}P_1P_2R_N \exp(-Dt/\lambda^2). \tag{3.35}$$

From the theory of diffusive transport (or equivalently by solving the symmetric random walk problem) it can be shown that the probability for an electron to diffuse

a distance L in a time between t and $t + dt$ in a system with diffusion coefficient D is given by

$$P(t)dt = 1/\sqrt{4\pi Dt}\exp(-L^2/(4Dt))dt. \tag{3.36}$$

By averaging $R_D(t)$ (equation [3.35]), over all possible times with the weighting factor $P(t)$ defined above[10], it is possible to recover equation (3.34).

3.2.3 Contact resistance

Besides the spin-dependent resistance described in the previous sections, another significant measurement is that in which the current is injected from lead B_1 and drained through lead N_1, while the voltage between leads T_1 and N_2 is measured (see Fig. 3.9). In the absence of spin injection the result of this measurement would be the contact resistance R_{c1}, defined in equation (3.32). However, in the presence of spin injection there is an additional effect produced by the spin accumulation at the interface which acts as an additional resistance for the injection of spin polarized electrons δR [13, 53], and which was illustrated in the previous section in Fig. 3.8. The general expression for the contact resistance is complicated and depends not only on the parameters of the measured contact but also on the distance to the other contact and its parameters. However, for large separations between F_1 and F_2, it can be shown that δR is always positive. This can be understood from the perspective of the Johnson-Silsbee spin-charge coupling [27, 3, 24]. Spin that accumulates near the F_N interface due to the interplay of spin relaxation and spin diffusion acts as an

[10] More precisely, $\int_0^\infty R_D(t)P(t)dt$.

effective impedance for the flow of more spin polarized electrons since it raises the local electrochemical potential of the majority spin in both F and N metals. Since spin and charge are carried by electrons, the back-flow of spin due to diffusion is accompanied by an additional resistance to charge flow. An important limiting case that yields a simple result is that of large contact resistances [equation (3.33)]. In that case the measured contact resistance is given by equation 3.32.

3.3 Effect of leakage currents

The effect of leakage currents was analyzed by solving equations 3.27 in the general case of additional current through regions 4, 5, and 7 in Fig. 3.9. The results of the analysis are shown in Fig. 3.10 for five different values of the leakage current through each of the regions. For the calculations a current of 100 μA was applied between leads T_1 and N_1 (see Fig. 3.9) and an injector-detector separation of 582 nm was used. For leakage currents that are more than 10^3 times smaller than the injection current there is no significant change in the nonlocal resistance. When the leakage current is as large as 1% of the injection current there is only a 6% change in the nonlocal resistance, but above 1% the nonlocal resistance changes dramatically. Therefore the effect of leakage currents is significant only for extremely large leakage currents, larger than 0.1% of the injection current.

3.4 Hanle effect: spin precession

An important tool for extracting parameters such as the spin relaxation length and the interfacial spin current polarization in spin valve structures is the Hanle effect,

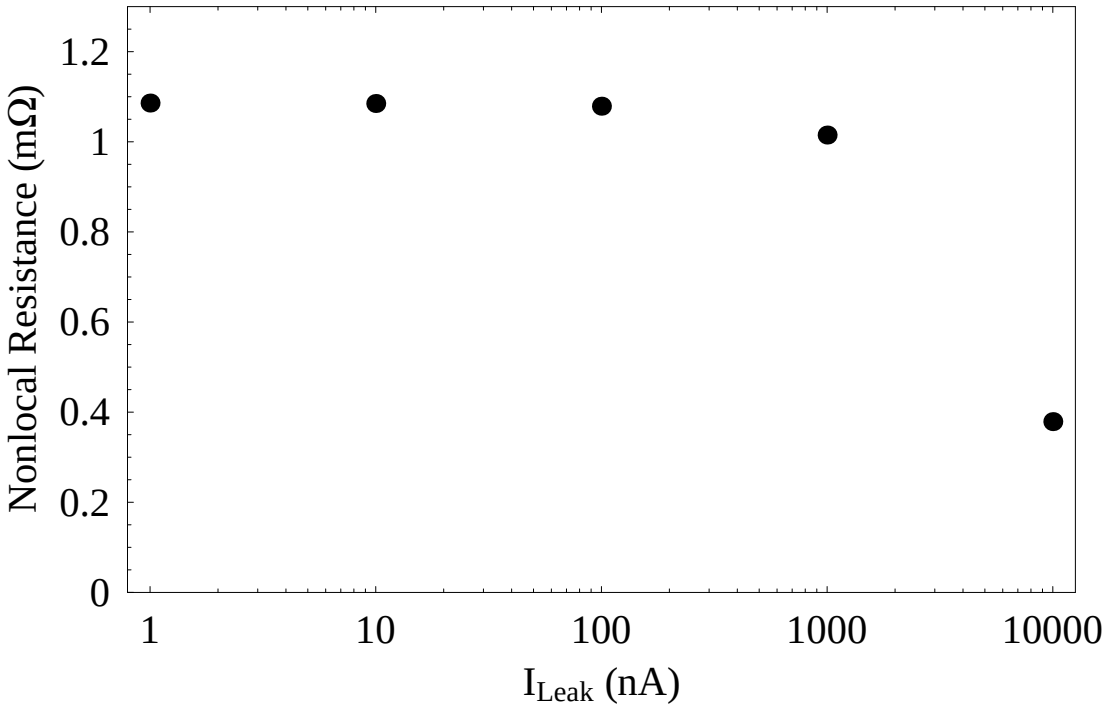

Figure 3.10: Nonlocal resistance for a current of 100 μA in the presence of leakage currents through regions 4, 5, and 7 in Fig. 3.9. The horizontal axis gives the leakage current through each of the leads.

which is equivalent to the zero frequency version of Transmission Electron Spin Resonance (TESR). In this section I will give a brief introduction to spin precession in a constant magnetic field, and will explain how spin precession affects the nonlocal resistance measurements in the case of ballistic and diffusive transport.

If an electron spin is originally in the state $|\chi(t=0)\rangle = |+_y\rangle$, that is, at time zero the spin is "up" in the y direction, then, in the presence of a magnetic field of magnitude $B_\perp$ in the z direction, the electron spin at time t will be given by $|\chi(t)\rangle = \exp(-i\omega t\hat{S}_z/\hbar)|\chi(t=0)\rangle$ where ω is the Larmor frequency $\omega = g\mu_B B_\perp/\hbar$, μ_B is the Bohr magneton, g is the electron Lande g-factor, and $\hat{S}_z$ is the spin operator in the z direction. After applying the exponential operator the result is the well

known expression [54] $|\chi(t)\rangle = \cos(\omega t/2)|+_y\rangle - \sin(\omega t/2)|-_y\rangle$. The probability of the electron having spin up in the y direction after time t is therefore $\cos^2(\omega t/2)$ and the probability of the electron having spin down at time t is $\sin^2(\omega t/2)$. The average spin per electron in the y direction at time t is therefore $\hbar/2[\cos^2(\omega t/2) - \sin^2(\omega t/2)] = \hbar/2\cos(\omega t)$. So even though each electron spin precesses around the direction of the magnetic field with frequency $\omega/2$, the average spin in the y direction precesses with frequency ω.

In the absence of spin relaxation and in zero magnetic field, spin polarized electrons injected at F_1 (see Fig. 3.9) diffuse to F_2 without losing their spin information[11]. Furthermore, if electron transport is ballistic between F_1 and F_2, all of the electrons will take the same time to travel from the injector to the detector, say a time t_b. If the perpendicular magnetic field is zero then $\theta = \omega t_b = 0$ and the average spin in the y direction (see Fig. 3.9) does not change with time so the electron spins arrive to the detector aligned with the magnetization of F_2 and the measured nonlocal resistance should be given by the positive value of equations (3.31) and (3.34). When a nonzero perpendicular magnetic field is applied, the average spin in the y direction of the electrons arriving to the detector is proportional to $\cos(\omega t_b)$ [55, 49][12]. If the average spin in the y direction of the electrons that arrive at F_2 has rotated by an angle $\theta = \omega t_b = \pi$, their spin is completely anti-aligned with the magnetization of the detector, and the measured nonlocal resistance should be given by the negative value of equations (3.31) and (3.34). If $\theta = \pi/2$ the average spin in the y direction

[11]For simplicity it can be assumed that both the magnetizations of F_1 and F_2 are aligned.

of the electrons arriving to F_2 will be zero so the nonlocal resistance vanishes. If the field is so strong or the time of flight so long that $\theta = \omega t_b = 2\pi$, the spin of the electrons arriving to F_2 will once more be aligned with F_2 giving again a positive value. However, for values of the perpendicular magnetic field $B_\perp$ comparable to the internal field of the magnetic material, the magnetization of F_1 and F_2 can start to rotate out of the plane and further considerations have to be made to interpret the results.

Transport between F_1 and F_2 is, however, diffusive, so there is a distribution of times for the electrons to travel between injector and detector (equation [3.36]). Furthermore, the spin relaxes with a characteristic length scale λ. Therefore, in the limit of large contact resistances, the nonlocal resistance should be given by a weighted sum of equation 3.35 times the rotation term $\cos(\omega t_b)$ with the weight being given by the probability density $P(t)$, more precisely

$$R(\omega) = \pm \int_0^\infty R_D(t) cos(\omega t) P(t) dt. \tag{3.37}$$

The complete expression in the case of large contact resistances is

$$R(\omega) = \pm \int_0^\infty \frac{1}{2} \frac{P_1 P_2 R_N}{\sqrt{4\pi D t}} \exp(-Dt/\lambda^2) \cos(\omega t + \alpha) \exp(-L^2/(4Dt)) dt, \tag{3.38}$$

where $\cos(\omega t)$ has been replaced by $\cos(\omega t + alpha)$ to allow for possible misalign-

[12]This factor of $\cos(\omega t_b)$ can also be understood as a position dependent rotation of the reference frame, so that at each coordinate x the positive y axis is aligned with the average spin of the electrons (the reference frame rotates with frequency ω around the axis of the magnetic field). Therefore F_2 will be rotated by an angle ωt_b with respect to the local reference frame, and the projection of the average y spin onto the magnetization direction of F_2 will be given by $\cos(\omega t_b)$.

ments between the magnetizations of F_1 and F_2 in case that an angle α exists between the easy axis of the two magnetic contacts.

3.5 Interface spin-flip scattering

Throughout the previous sections of this chapter it was assumed that spin-flip scattering at the F-N interfaces was negligible. In this section the effect of interfacial spin-flip scattering will be considered by relaxing the assumption of spin current conservation at the interfaces. To quantify the amount of interfacial spin-flip scattering, parameters which can in principle be calculated if the details of the spin scattering are known, will be used. Spin valves with both transparent and resistive interfaces can be analyzed using the general framework of resistive contacts, since the former can be considered to be a limiting case in which the interface resistances vanish.[13]

3.5.1 Nonlocal geometry spin valve with interfacial spin-flip scattering

The process of interfacial spin-flip scattering can be pictured as the transition from the incoming states $|\phi_\uparrow>$ and $|\phi_\downarrow>$ in the nonmagnetic metal into the outgoing states $|\psi_\uparrow>$ and $|\psi_\downarrow>$ in the ferromagnet, where $\uparrow$ and $\downarrow$ refer to the spin in the z direction. The rate at which transitions between incoming and outgoing states occur can be calculated using Fermi's golden rule if the density of states and the transition probabilities between states $|\phi_\uparrow>$, $|\phi_\downarrow>$ and $|\psi_\uparrow>$, $|\psi_\downarrow>$ are known. This requires knowledge of microscopic details of the interfaces which are outside the scope of

[13] See discussion after equation (3.31).

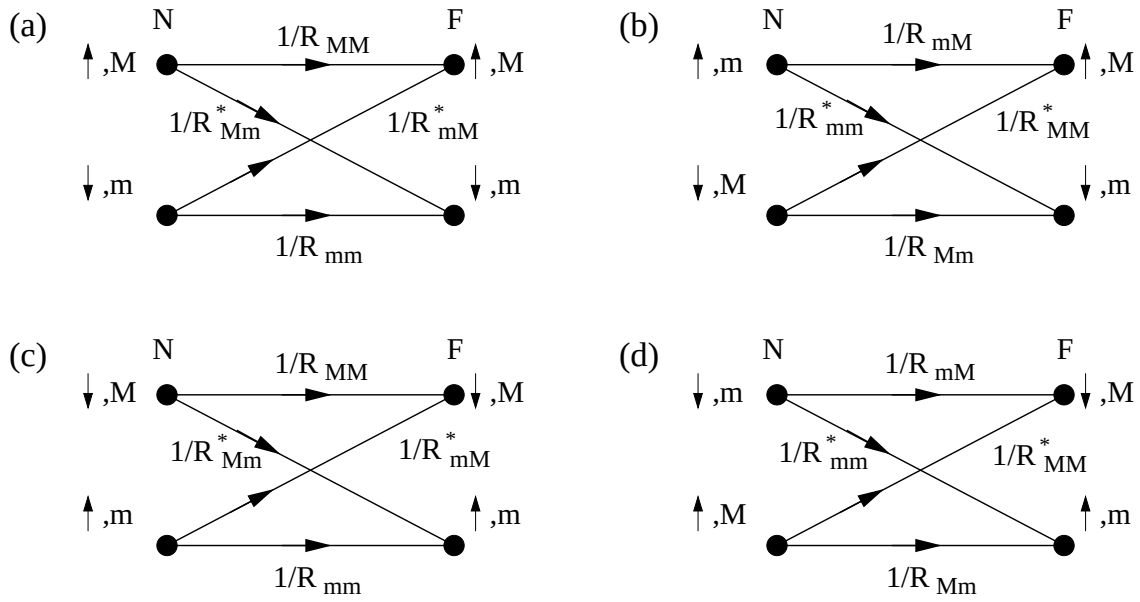

Figure 3.11: Diagrams representing the scattering at the interface together with phenomenological coefficients R that represent the interface resistance of each spin channel. (a) Majority carriers of each region are aligned and have spin $\uparrow$. (b) Majority carriers of the ferromagnet have spin $\uparrow$ while majority carriers of the nonmagnetic metal have spin $\downarrow$. (c) Majority carriers of each region are aligned and have spin $\downarrow$. (d) Majority carriers of the ferromagnet have spin $\downarrow$ while majority carriers of the nonmagnetic metal have spin $\uparrow$.

this work. However, in the case of small voltage biases[14] [56, 57] the currents and electrochemical potentials at both sides of the interface can be related by means of a set of phenomenological parameters with the physical meaning of resistance which completely describe the scattering process of the transmitted electrons. The pictorial representation shown in Fig. 3.11 is useful for defining each of the resistance parameters R. The horizontal lines represent conserved spin transitions while the lines drawn at an angle represent spin-flip events at the interface. $\uparrow$ and $\downarrow$ clearly label spin up and spin down channels, which have an additional label M for spin majority or m for spin minority. This labels can be used for both the ferromagnet

[14]Small compared with the thermal energy divided by the charge.

and nonmagnetic metal.[15] N and F label the nonmagnetic and ferromagnetic sides of the interface. Figures 3.11 (a), (b), (c), and (d) have different alignments between the excess magnetization in the nonmagnetic metal and the magnetization in the ferromagnet. In Fig. 3.11 (a) the majority carriers of each region have spin up, while in Fig. 3.11 (b) the majority carriers in the nonmagnetic metal have spin down. In Fig. 3.11 (c) the majority carriers of each region have spin down, while in Fig. 3.11 (d) the majority carriers in the nonmagnetic metal have spin up. A resistance term such as R^*_{Mm} is defined as the interfacial resistance from the majority (M) spin channel in the nonmagnetic metal to the minority (m) spin channel in the magnetic metal with spin-flip (*). On the other hand a term such as R_{Mm} means the interfacial resistance from the majority (M) spin channel in the nonmagnetic metal to the minority (m) spin channel in the magnetic metal without any spin-flip. Therefore subindexes like Mm do not necessarily require a spin flip since majority carriers in one metal can have spin $\uparrow$ while majority carriers in the other metal can have spin $\downarrow$ [Fig. 3.11 (b)].

From the diagrams shown in Fig. 3.11 it is possible to write the boundary conditions for the electrochemical potential at each F-N interface, which relate the difference in electrochemical potential across the interface with the current and with the resistance coefficients R. As an example of this procedure, the boundary equations for the F_2-N interface (detector) when the magnetizations of injector and

[15]Majority and minority carriers are well defined in ferromagnets. We have extended these terms to refer to the nonequilibrium magnetization present in the nonmagnetic metal, so if there is an excess of electrons with spin up, then those are the majority carriers in the normal metal.

detector are aligned and pointing ↑ [Fig. 3.11(a)] are written explicitly:

$$\begin{aligned} j_{\uparrow}^{F} A_{C2} &= (\mu_{\uparrow}^{N} - \mu_{\uparrow}^{F})/R_{MM} + (\mu_{\downarrow}^{N} - \mu_{\uparrow}^{F})/R_{mM}^{*} \\ j_{\downarrow}^{F} A_{C2} &= (\mu_{\uparrow}^{N} - \mu_{\downarrow}^{F})/R_{Mm}^{*} + (\mu_{\downarrow}^{N} - \mu_{\downarrow}^{F})/R_{mm} \\ j_{\uparrow}^{N} A_{C2} &= (\mu_{\uparrow}^{N} - \mu_{\uparrow}^{F})/R_{MM} + (\mu_{\uparrow}^{N} - \mu_{\downarrow}^{F})/R_{Mm}^{*} \\ j_{\downarrow}^{N} A_{C2} &= (\mu_{\downarrow}^{N} - \mu_{\uparrow}^{F})/R_{mM}^{*} + (\mu_{\downarrow}^{N} - \mu_{\downarrow}^{F})/R_{mm}, \end{aligned} \tag{3.39}$$

where A_{C2} is the contact area of the F_2-N interface, and where j_{σ}^{F} (j_{σ}^{N}) is the current density with spin σ going into the ferromagnetic region (out of the nonmagnetic region). The boundary conditions at the F_2-N interface for other configurations of the magnetizations of the injector and detector can be deduced from Fig. 3.11(b), (c), and (d). For the F_1-N (injector) interface, where current is injected from the ferromagnetic to the nonmagnetic metal, or in general when current flows in the opposite direction, diagrams similar to those shown in Figs. 3.11(a) and (c) can be obtained by simply reversing the direction of the arrows. For the injector interface only such diagrams exist since the majority carriers in both F_1 and N always have the same spin orientation. If the magnetizations of the injector and detector are parallel, then diagrams (a) or (c) should be used for both injector and detector interfaces. However, if the magnetization of injector and detector are anti-aligned either diagrams (a) for the injector interface and (d) for the detector interface or diagrams (c) for the injector interface and (b) for the detector interface must be used. Diagrams (b) and (d) therefore only apply to the F_2-N (detector) interface, where

majority carriers at both sides of the interface can have different spin orientation when the magnetization of the injector is antiparallel to the magnetization of the detector.

In order to see the effects of spin scattering, and without loss of generality, it will be assumed that the magnetization of the injector is fixed and pointing $\uparrow$, while the magnetization of the detector can have two possible orientations, either $\uparrow$ or $\downarrow$. Therefore, according to the previous discussion, when both magnetizations are aligned and pointing $\uparrow$, diagram (a) should be used to find the boundary conditions for both interfaces. On the other hand, when the magnetization of the injector is reversed, diagram (a) should be used for the injector interface and diagram (d) for the detector interface. After writing the boundary conditions corresponding to these diagrams, and using them to solve equations (3.25), an expression for the nonlocal resistance can be found. Since the result is not very illuminating it will not be transcribed here. However, in the limit of contact resistances much larger than the resistance of the ferromagnetic and nonmagnetic metals over their spin relaxation length [see equation (3.33)], it is possible to simplify the expression for the nonlocal resistance to obtain[16]

$$\begin{aligned} R^{\uparrow\uparrow} &= \frac{1}{2} P_1 P_2^{\uparrow\uparrow} R_N \exp(-L/\lambda) \\ R^{\uparrow\downarrow} &= \frac{1}{2} P_1 P_2^{\uparrow\downarrow} R_N \exp(-L/\lambda), \end{aligned} \tag{3.40}$$

where P of the injector and detector in the presence of interface spin-flip scattering

[16] See equation 3.34.

are defined as

$$
\begin{aligned}
P_1 &= \frac{(1/R_{1,MM} - 1/R_{1,mm}) + (1/R^*_{1,Mm} - 1/R^*_{1,mM})}{(1/R_{1,MM} + 1/R_{1,mm}) + (1/R^*_{1,Mm} + 1/R^*_{1,mM})} \\
P_2^{\uparrow\uparrow} &= \frac{(1/R_{2,MM} - 1/R_{2,mm}) + (1/R^*_{2,Mm} - 1/R^*_{2,mM})}{(1/R_{2,MM} + 1/R_{2,mm}) + (1/R^*_{2,Mm} + 1/R^*_{2,mM})} \\
P_2^{\uparrow\downarrow} &= \frac{-(1/R_{2,mM} - 1/R_{2,Mm}) + (1/R^*_{2,MM} - 1/R^*_{2,mm})}{(1/R_{2,mM} + 1/R_{2,Mm}) + (1/R^*_{2,MM} + 1/R^*_{2,mm})}.
\end{aligned} \tag{3.41}
$$

The difference between $R^{\uparrow\uparrow}$ and $R^{\uparrow\downarrow}$ is due to the difference between $P_2^{\uparrow\uparrow}$ and $P_2^{\uparrow\downarrow}$, which in turn comes from the difference between the spin-flip scattering of majority and minority carriers in the nonmagnetic metal. For both alignments of the magnetizations of F_1 and F_2, the spin polarization of the injector (P_1) is the same.

In the absence of interfacial spin-flip scattering all the resistance terms in equation (3.41) that contain a "*" should be dropped and the result should be the same as the original definition of the P_i given by equation (3.23). This equivalence can only be obtained if $R_{i\uparrow} = R_{i,MM} = R_{i,mM}$ and $R_{i\downarrow} = R_{i,mm} = R_{i,Mm}$, that is, if the non-spin-flip resistances are equivalent for majority and minority carriers in the nonmagnetic metal. Therefore equation (3.23) is a particular case of equation (3.41) with the assumption that the tunnelling of spin up and down electrons depends on which channel is the majority carrier in the ferromagnet, but is independent of which channel is the majority carrier in the nonmagnetic metal. This assumption can be justified since the difference in wave functions, the density of states at the Fermi energy, and the Fermi momenta between spin sub-bands is much larger in the ferromagnet. Hence the small differences between majority and minority carriers in

the nonmagnetic metal can be ignored for non-spin-flip tunnelling processes. If this assumption also holds for the spin-flip resistance terms, the nonlocal resistance for anti-aligned magnetizations of F_1 and F_2 is the negative of the nonlocal resistance in the case of aligned magnetizations. If this assumption does not hold, an additional component of the nonlocal resistance, which does not change sign when the injector magnetization is reversed, appears. An example of a case in which the assumption is not valid is when the probability of a spin-flip event for spin σ is proportional to the density of states with spin σ in the ferromagnet. According to Fermi's golden rule the transmission rate is proportional to the density of states of the outgoing spin state $\bar{\sigma}$ (opposite to σ) and to the probability of the transition. Therefore the product of the densities of states for majority and minority carriers in the ferromagnet appear in the calculation of all of the spin-flip resistances R^*. In this case the differences between minority and majority carriers in the nonmagnetic metal might be important so the approximation is not necessarily valid. This will be relevant in chapter 5, where experimental evidence for the existence of an additional component of the nonlocal resistance, which does not change sign with the reversal of the magnetization of the injector, is shown.

Chapter 4
Sample fabrication and experimental setup

In this chapter the techniques used to fabricate the spin valve devices used for spin injection and detection measurements via transport will be described. Then a brief overview of the experimental setup will be given.

4.1 Sample fabrication

Since the size of the smaller features required for the spin valve devices is of the order of 100 nm, and since the alignment between magnetic and nonmagnetic levels is essential, the samples are fabricated using two levels of electron beam lithography together with thermal evaporation. The complete procedure will be explained in this section.

One inch 100-orientated Si wafers with 500 nm thermally grown SiO_2 are used as a substrate. The wafers are covered with a bilayer of positive e-beam resist [poly methyl methacrylate (PMMA)] of molecular weights 150,000 and 360,000 by spinning at 2500 rpm, and have typical thickness 150 nm and 250 nm respectively. Each layer of PMMA is baked at 40^oC for 2 minutes, 80^oC for two more minutes, and 140^oC for 30 minutes to avoid inter-layer mixing. A final bake of 90 minutes is done after the bilayer is completed. The coated wafers are cleaved into quarters, each of

which is processed separately. About ten devices can be fabricated in each of the wafer quarters. An electron beam with an accelerating voltage of 30 kV, working distance of 8mm, typical currents 30-60 pA, and field scale 60 μm[1], is used to expose the regions of the PMMA that are to be covered by the magnetic material with a typical dose of 5.9 pC/μm^2 [Fig. 4.1(a)]. The difference in molecular weight, together with the backscattered and secondary electrons creates a profile in the PMMA as shown in Fig. 4.1(b). In order to align the first and second levels of electron beam lithography, and in order to focus the electron beam correctly, a small region of PMMA is overexposed at a field scale of 8μm with the typical e-beam currents for 30-45 seconds. The region with cross-linked PMMA (due to overexposure) can be easily seen with the SEM, so focusing and stigmation adjustments can be made. If immediately after one of these focusing spots has been made the areas to be covered by the magnetic material are exposed by the electron beam, this focusing spot can be used as a very precise alignment marker for the second level of lithography [see Fig. 4.2(a)]. Developing, or removal of the exposed PMMA, is done by immersing the wafer in a methyl isobutyl ketone (MIBK):isopropyl alcohol (IPA) (1:3 by volume) solution at 23^o C for 30 seconds [Fig. 4.1(c)], rinsing the wafer by immersing it in isopropanol, and blow drying it with research grade compressed N_2. This creates a mask for transferring the patterns onto the substrate. The wafer is immediately transferred to the vacuum chamber of an evaporator to avoid contamination. After reaching typical base pressures between 7×10^{-7} Torr and 2×10^{-6} Torr, the wafer

[1]JEOL-420 Scanning Electron Microscope (SEM)

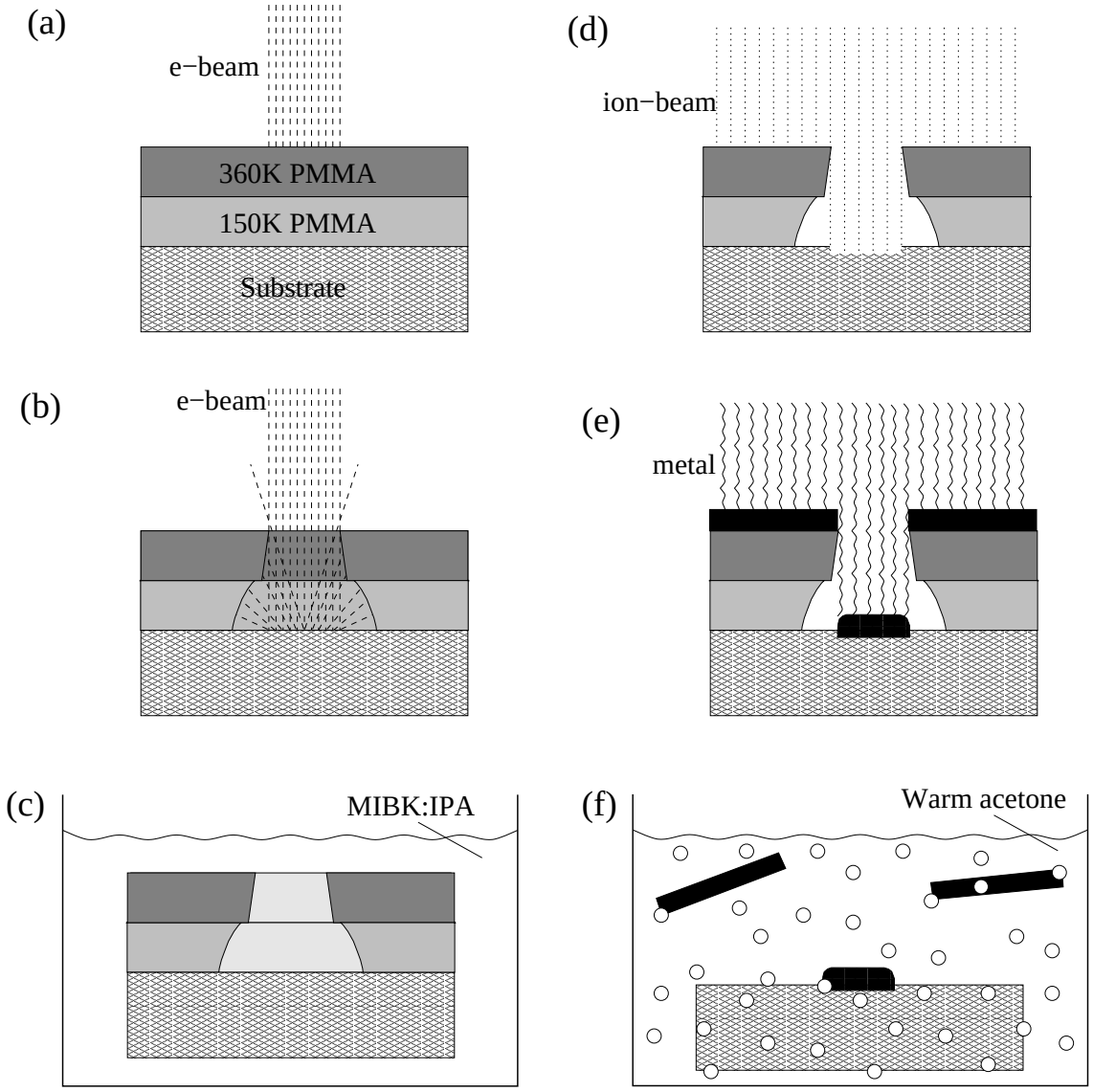

Figure 4.1: Schematic of the e-beam lithography and thermal evaporation process for sample fabrication. A side view of the wafer is shown. (a) Substrate and PMMA bilayer. (b) Exposure of the PMMA to the e-beam. (c) Developing (or removal) of the exposed PMMA. (d) Ion milling of the substrate for cleaning and increasing adhesion. (e) Thermal evaporation of metal. (f) Lift-off of the remaining PMMA and metallization.

is ion milled with Argon for 30-80 seconds in a Commonwealth Plasma system at a pressure of 1×10^{-4} Torr, with a beam voltage of 500 V, an accelerating voltage of 100 V, 5 mA of current, and a neutralizer current of 7.5 A [Fig. 4.1(d)]. The purpose of ion milling is to clean the substrate of any remaining undeveloped PMMA and additional contamination (like IPA), increasing the adherence of the metallic film. The vacuum chamber is pumped once more to a pressure lower than 2×10^{-6} Torr, and the magnetic material [Co or Py (permalloy[2])] is thermally evaporated using rates between 0.1 and 0.5 nm/s. The typical thickness of the evaporated film is 36 nm according to the in-situ film thickness monitor, which has been calibrated using a Tencor alfa-step profilometer. The evaporated material sticks to the exposed wafer through the holes in the mask and also to the PMMA mask itself [Fig. 4.1(e)]. After waiting for the system to cool down for 30 minutes at low pressure, the sample is extracted from the chamber and immediately introduced in warm acetone, which lifts-off the remaining PMMA removing the film from unexposed regions and leaving only the metal that adhered directly to the substrate. Ultrasound is sometimes used to help with the lift-off process [Fig. 4.1(e)].

After the first level has been completed, the sample is again covered with a bilayer of PMMA, baked and inserted in the SEM. Some of the focusing spots made during the first level are used to align the rotation of the stage, and also as a map to find the position of each sample. The electron beam is blocked and the stage is moved to the focusing spot that serves as the alignment marker for a particular sample.

[2]NiFe 80-20.

The beam is unblocked at a small field scale (10μm) and after coarse adjustment has been made, the field scale is reduced to 1μm, where precise alignment to within 50 nm to 100 nm can be made. Then, electron beam lithography is done at two different magnifications. First the small features are exposed to the e-beam with the same parameters as in the first level [see the narrow wires in Fig. 4.2(a)], but then a field scale of 1.5 mm is used to expose the large features such as connecting wires and bonding pads using currents as large as 7000 pA [see Fig. 4.2(b)]. In the case of transparent samples, the remaining steps of the second level are exactly the same as the first, except that Cu is evaporated instead of Co or Py using a different mask. In the case of resistive contacts, additional steps in the second level of material deposition, between the ion milling [Fig. 4.1(d)] and the Cu thermal evaporation [Fig. 4.1(e)], are necessary. First, just after ion milling, when the pressure is lower than 2×10^{-6}, 2 nm of Al are thermally evaporated to make a thin covering of the exposed magnetic material. Pumping is then stopped and 100 to 800 mTorr of O_2 is let into the chamber. The aluminum is oxidized for 4 minutes, after which pumping is resumed, and the remaining steps of the second level [Figs. 4.1 (e) and (f)] are completed. By controlling the oxygen pressure, the barrier thickness and resistivity can be controlled. However, the resistance of the barrier is very sensitive to its thickness, which can vary due to surface roughness of the magnetic film. Therefore fabricating barriers of specified resistance can be challenging, but since the only requirement is that they be large compared to the resistance of Py, Co, and Cu over their spin relaxation lengths (see chapter 3), any value larger than a

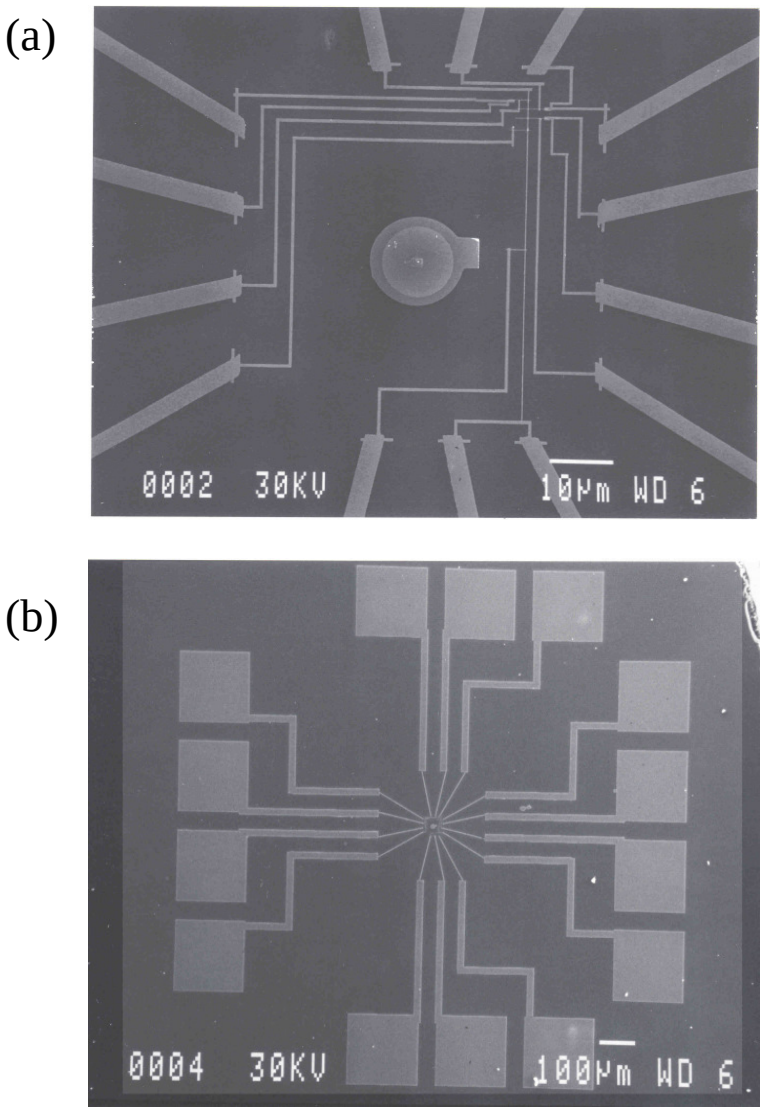

Figure 4.2: SEM micrographs of the typical large field samples design. (a) Focusing and alignment spot, together with additional wiring at a field scale of 120 μm. (b) Bonding pads and additional wiring at a field scale of 2mm.

few ohms is acceptable. However, due to the stray capacitances in the experimental setup, barrier resistances larger than a few hundred ohms contribute to capacitive leakage which increases as the square of the barrier resistance and should therefore be avoided.

Spin valve designs evolved as the understanding of the spin resistance increased. The first working sample design is shown in the SEM micrograph in Fig. 4.3(a). This sample is of the cross geometry type. The light gray lines are made of Cu, the gray ones are made of Py, and the remaining dark gray regions are the substrate. Vertical alignment is critical since the separation between the two Py lines is close to 350 nm and the width of the horizontal Cu line is 100 nm, leaving only 125 nm of clearance above and below, much smaller than the typical backslash of the SEM mechanical stage. However, as explained in chapter 3, this particular geometry is not optimal for spin injection and detection experiments, and a nonlocal geometry [Fig. 4.3(b)] is preferred. The micrograph shown in Fig. 4.3(b) was taken at an angle to show the crossings of the Cu lines over the magnetic contacts. A better view of a single contact is shown in Fig. 4.3(c) where a very nice overlap between the magnetic and non-magnetic level can be seen. For some of the measurements samples with many consecutive magnetic contacts that would be used for both injection and detection were fabricated [Fig. 4.3(d)]. In such samples the distance between consecutive magnetic contacts increases so the length dependence of the nonlocal resistance can be studied with sets of measurements on a single sample. Figures 4.3 (a), (b), and (d) show two essential features of the magnetic

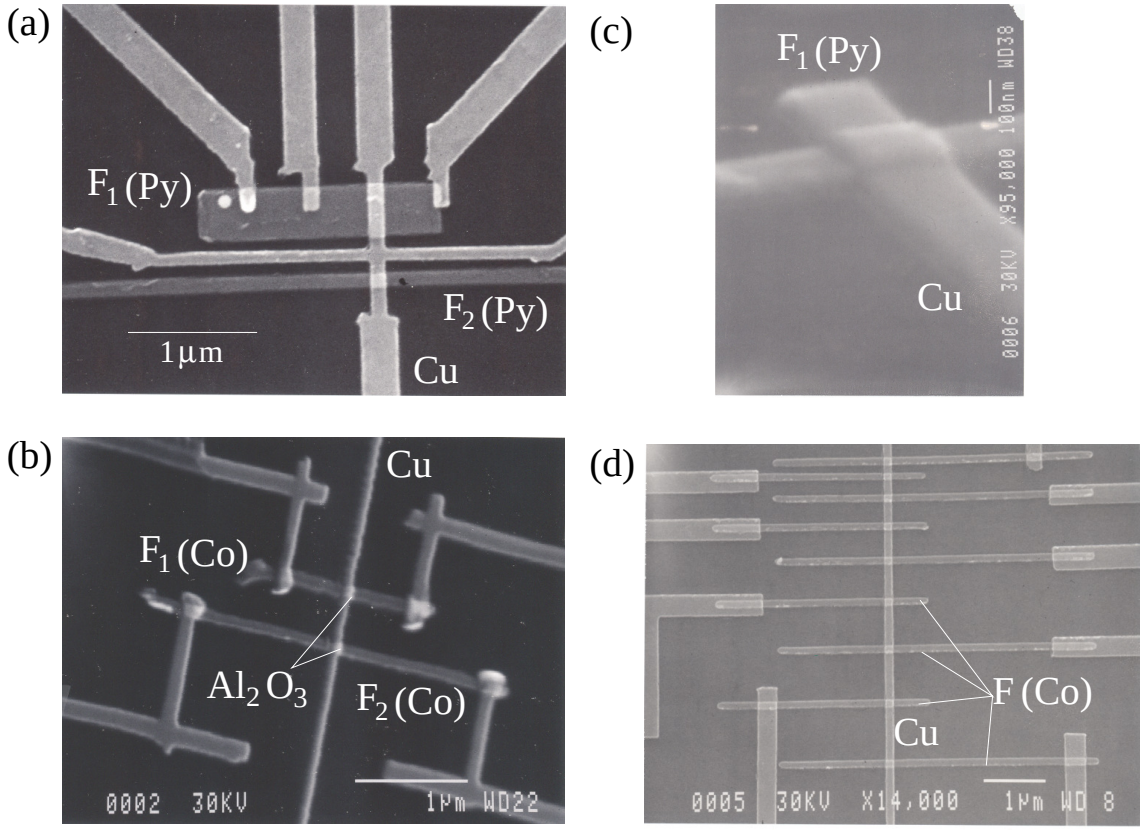

Figure 4.3: SEM micrographs of finished spin-valve samples. (a) Cross geometry Py-Cu sample.(b) Typical nonlocal resistance Co-Cu sample. (c) Typical contact between magnetic and non-magnetic levels for a Py-Cu sample. (d) Sample with many magnetic contacts for measuring the length dependence of the nonlocal resistance.

contacts. First, the high aspect ratios that were used to keep the magnetization of the magnetic contacts in either of two antiparallel directions along the longer (easy) axis of each contact. Second, the different aspect ratios that were used for consecutive magnetic injector-detector pairs in order to allow independent control of the magnetization alignment of each contact by means of an external magnetic field.

For completeness, tables with the relevant information about the samples that were reported in this thesis are shown below.

Device Name	Configuration	Py	Co	Al_2O_3
sam2b8s1	Cross Geometry,2	√		None
sam4b1s4	Nonlocal,8	√		None
sam10b3p1	Nonlocal,9	√		None
sam10b3p3	Nonlocal,9	√		None
sam12b1p2	Nonlocal,9	√		None
s_sam11b2y1p2	Nonlocal,2,2		√	410mTorr
s_sam11b2y3p2	Nonlocal,2,2		√	122mTorr
s_sam12p2	Nonlocal,2		√	423mTorr
s_sam12p11	Nonlocal,2		√	None
s_sam10b1p1	Nonlocal,9		√	None
s_sam10b3y3p1	Nonlocal,9	√		None

Table 4.1: Device characteristics. The number of magnetic contacts is given under "Configuration", where "2,2" means two contacts separated by a large distance from the next two contacts. The magnetic material used for each device is specified with a check under either "Py" (Permalloy) or "Co" (Cobalt). If an oxide barrier is used between ferromagnetic and nonmagnetic metals, the pressure of O_2 during oxidation is given under "Al_2O_3".

When the samples have been completed, they are again coated with PMMA for protection, but this time no baking is used since this affects the quality of the Cu film. A manual wafer dicer is then used to separate the samples that fit into a wafer quarter, after which they are dipped in acetone to remove the PMMA protective layer, rinsed with isopropanol, and blow dried. Silver paint is used to adhere each finished sample to a ceramic header with 16 Be-Cu pins, and after grounding the pins to avoid electrostatic discharges that can damage the thin lines in the device, bonds with 32μm thick aluminum wire are made from the pins to the bonding pads.

4.2 Experimental setup

The experimental setup has four main components which are the probe, the control electronics, the measurement electronics, and an AD-DA converter and computer.

Device Name	Th	W	Cu Th	Cu W	L
sam2b8s1	85 nm	470nm, 120nm[3]	90 nm	120nm[2]	35 nm[2]
sam4b1s4	30 nm	470nm,100nm	48 nm	150nm	200-1500nm[3]
sam10b3p1	34 nm	135 nm	45 nm	125 nm	354-1068nm[4]
sam10b3p3	34 nm	140 nm	45 nm	125 nm	354-1068nm[4]
sam12b1p2	48 nm	100 nm	76 nm	130 nm	354-1068nm[4]
s_sam11b2y1p2	32 nm	100 nm	54 nm	100 nm	525,740 nm
s_sam11b2y3p2	32 nm	115 nm	54 nm	120 nm	987,1220 nm
s_sam12p2	36 nm	150 nm	54 nm	150 nm	717 nm
s_sam12p11	36 nm	128 nm	54 nm	180 nm	980 nm
s_sam10b1p1	36 nm	130 nm	48 nm	140 nm	252-966nm[5]
s_sam10b3y3p1	42 nm	130 nm	48 nm	140 nm	252-966nm[5]

Table 4.2: Device lengths. The abbreviated column titles are "Thickness" of the ferromagnetic material, "Width" of the ferromagnetic material, "Cu Thickness", "Cu Width", and "L", the separation between contacts. In the case of many magnetic contacts the separations of consecutive contacts are given in the footnotes.

The probe consists of an aluminum shielding box with BNC connectors, fixed on top of a copper-nickel tube with a brass ring at the bottom. A nonmagnetic 16 pin socket which holds the ceramic sample header is thermally grounded and fixed to the brass ring with Emerson-Cummings 2850 epoxy. A Lake-Shore platinum (PT-111) calibrated thermometer is also thermally grounded and fixed to the brass ring. Wiring for the socket is made of copper-nickel wire with a resistance of 23 Ω from the box to the socket, while low resistance copper wiring is used for the magnet and thermometer leads. Wires are paired up, twisted and covered with additional insulation. In addition, signal wires are tied together to reduce inductive pickup. However this increases their capacitance, which is 230 pF between twisted pairs, 120 pF between non-twisted pairs, and 160 pF between each lead and ground. The

[2]Quantities not measured but expected from lithography or from similar measured samples.
[3]Separations between consecutive lines are 200, 240, 240, 402, 798, 1200, 1500 nm.
[4]Separations between consecutive lines are 354, 456, 558, 660, 762, 864, 966, 1068 nm.
[5]Separations between consecutive lines are 252, 354, 456, 558, 660, 762, 864, 966 nm.

superconducting magnet (made of niobium in a copper matrix) is a small 1.25 inch outer diameter by 2 inch high cylinder with a soft iron core in part of its interior, which provides 57.3 mT/A at the site of the sample in a direction parallel to the axis of the probe. For measurements in which a field parallel to the plane of the sample is needed, an additional socket is used, which allows the plane of the sample to be set vertically. In such a configuration the field produced by the magnet is 47.1 mT/A at the site of the sample.

The control electronics is used to measure the temperature close to the sample and to set and sweep the magnetic field. Measurement of the temperature is done by using a Monogram Omega controller, which measures the four terminal resistance of the Pt thermometer, converts it to a temperature value using a previous three point calibration and interpolation in the 77 K-293 K range, and outputs a voltage proportional to the temperature which is read by the computer via the AD converter. The magnetic field control is done by using an HP 3325A synthezizer/function generator to produce a triangular wave of adjustable frequency (typically in the 0.01-0.00003 Hz range) and amplitude which is used to voltage control a bipolar Kepco source (model BOP 20-10 M) operating as a voltage source. The output of the source is connected to a 0.101 Ω, 25 W resistor, at which the voltage drop is measured using an HP3456A digital multimeter and the AD converter in order to monitor the current. After the resistor, a coaxial cable is used to carry the current to an isolated BNC on the box of the probe, and from there thick Cu wires carry the current down to the magnet.

The measurement electronics is used to bias the spin-valve device and detect the small signals that are produced. To accomplish this, two PAR-124 lock-in amplifiers (I and II), tuned to a frequency of 11.1 Hz are used. Operating at higher frequencies was avoided even though it could reduce the noise even further, since it would increase the capacitive leakage through the wiring and through the input impedance of the lock-in amplifiers. The second lock-in amplifier is phase locked to the internal oscillator of the first one. The source output of the first lock-in is connected to a Vishay bias resistor of 100KΩ in series with a Vishay 2KΩ resistor to monitor the current. The bias signal is then taken by a coaxial cable to one of the BNC connectors in the shielding box at the top of the probe (connected, say to lead B_1 in Fig. 3.9). The voltage drop at the 2KΩ resistor is measured with that same lock-in (I) and the output of I is read by the computer through the AD converter. A grounding cap is used to connect the inner conductor (connected, say to lead N_1 in Fig. 3.9) of another of the BNC's to the shielding box (which is grounded only through the exterior conductor of the current input coaxial cable). Two other coaxial cables are used to connect the remaining measurement leads (T_2 and N_2 in Fig. 3.9) to the inputs of the differential preamplifier of lock-in (II), and the in-phase signal is monitored by the computer via the AD converter.

Experiments at low temperature are done by inserting the dipping probe in liquid helium (for measurements at 4.2^o K) and liquid nitrogen (for measurements at 77^o K). Temperature variation in the 100^o K-293^o K range is achieved by inserting the dipping probe in a dewar above the liquid nitrogen level. By changing the height

of the sample above the liquid nitrogen, or equivalently by allowing the nitrogen level to slowly drop due to N_2 evaporation, the temperature of the sample can be adjusted. The dipping probe has a large thermal mass surrounding the sample so the temperature changes in the device are slow to make sure that the temperature of the thermometer and the temperature of the sample are equivalent. By measuring the temperature dependence of any quantity both on cool-down and warm-up and comparing the results, variations between the sample and thermometer temperatures can be detected. During the experiments the temperature change was slow enough so that the traces on cool-down and warm-up were equal to within the noise.

Chapter 5
Spin Valve Measurements

In this chapter I will present the measurements that were performed on Py-Cu and Co-Cu spin valves, which include the characteristic switching of the spin-dependent resistance with the reversal of injector or detector magnetization, spin precession (Hanle effect), length dependence of the spin-dependent resistance, and temperature dependence of the nonlocal resistance for aligned and anti-aligned configurations of the injector and detector magnetizations. I present evidence for the existence of a symmetric component of the nonlocal resistance and provide cross checks that were done to rule out spurious origins of this previously ignored signal, like capacitive leakage, heating coupled with thermo-power, and classical electrostatic effects coming from the solution of Laplace's equation for the potential in a non-ideal conductor for a particular geometry.

5.1 Cross geometry configuration

The initial configuration that was used to study spin injection and detection was the cross geometry described in chapter 3, Fig. 3.3 (see also the insets of the following figures). In this section I will present the results of such measurements and will describe the possible problems that may appear when interpreting the results.

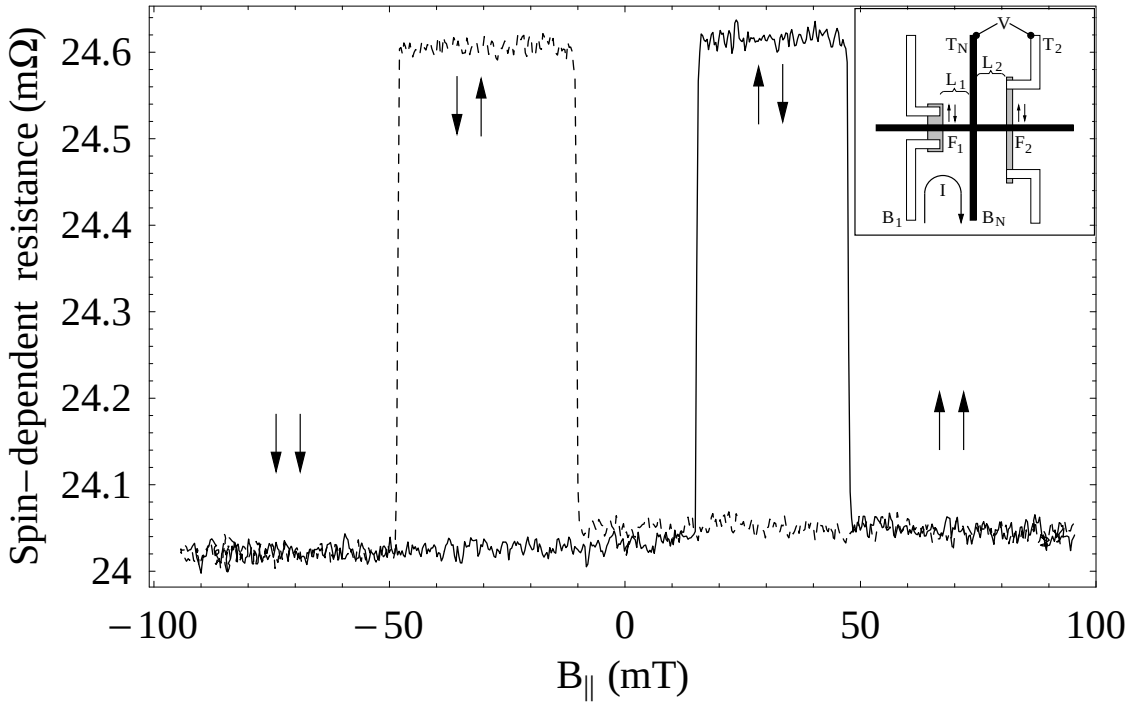

Figure 5.1: R vs $B_{\|}$ for sample sam2b8s1 at 4.2 K. This sample has transparent Py-Cu contacts. The inset shows a schematic of the sample layout and measurement configuration.

As discussed in chapter 3, one of the characteristic signals of spin injection is the switching of the spin-dependent resistance defined as $R = V_{T_N-T_2}/I_{B_1-B_N}$ (where the labels are shown in the inset of Fig. 5.1) when the magnetization of either of the magnetic contacts changes direction due to the applied field. Figure 5.1 shows the spin-dependent resistance as a function of the magnetic field $B_{\|}$ applied parallel to the easy axis of the magnetic contacts of a Py-Cu sample with transparent interfaces at 4.2 K. The solid (dashed) line is for increasing (decreasing) $B_{\|}$. At large negative fields the injector (F_1) and detector (F_2) are parallel and pointing down. When the field is increased above the positive coercive field of the injector, about 15 mT, its magnetization reverses and R switches from 24.02 mΩ to 24.62 mΩ. When the field

is further increased above the positive coercive field of the detector, about 47 mT, its magnetization reverses, the two magnetic contacts become parallel once more but this time pointing up, and R switches to 24.04 mΩ, close to the large negative field value. If the field is then decreased, the two magnetic contacts will remain parallel until the negative coercive field of the injector is reached at -10 mT, when its magnetization reverses and R switches to 24.60 mΩ. When the field is further reduced to the negative coercivity of the detector, about -47 mT, its magnetization also reverses, the two magnetic contacts point down, and R changes to its low value of 24.02 mΩ.

The positive and negative field coercivities of the injector are different showing that there is a preferred direction for its magnetization. In addition, the positive field reversal of the injector is slower than the negative field reversal, providing more evidence that it takes more energy to set the injector pointing up then down. This can be expected since for this sample the injector is 2.2 μm long by 0.5 μm wide, which gives a not very large aspect-ratio of 4.4, so any structural anisotropy arising from the thermal evaporation is relevant[1]. Another important detail from Fig. 5.1 is the fact that the values of R for the injector pointing up and down are slightly different (0.02 mΩ). This slight difference in R can be explained, not by a difference in the spin current polarization of the injector (P_1) for up and down directions of its magnetization, but instead by a slight misalignment of the magnetization

[1]No field was applied during evaporation so the easy axis of different grains are not necessarily aligned. For a small number of grains the distribution is not random and therefore a preferential direction for magnetization might occur.

of F_1 and F_2, by anisotropic magnetoresistance (AMR), or Hall effect. The fact that the value of R can be affected by AMR and Hall effect shows that this is not the optimal geometry for the detection of a spin-related signal. In addition, the existence of a large background (24.3 mΩ), roughly 40 times bigger than the spin-related signal, creates drifts due to temperature changes in the electronics, and denies the possibility of testing the symmetry of the spin-dependent signal that is predicted by the model [see equation (3.20)].

For completeness, 77 K measurements of the same sample are shown in Fig. 5.2. Many traces are plotted simultaneously to show the reproducibility in the magnetization reversal and in the switching of R. The same features as those shown for the 4.2 K measurement are still present, but the magnitude of the signal has changed. The size of the steps decreased to about 0.48 mΩ (from 0.58 mΩ at 4.2 K), and the background resistance increased to 37.44 mΩ. Both trends are expected since as temperature increases both spin preserving and spin-flipping mechanisms become more effective, decreasing the spin diffusion length (and therefore the magnitude of the steps) and decreasing the mean free path, (enhancing the resistivity which gives the main contribution to the background resistance).

In conclusion, spin injection and detection was shown to be possible in mesoscopic Py-Cu spin valves, the reversal of the magnetic contacts and the switching of the spin-related signal were shown to be reproducible, and the correct temperature trend for the background resistance and for the spin-dependent resistance was observed. However, since AMR, Hall effect, and even ohmic voltages are part of the

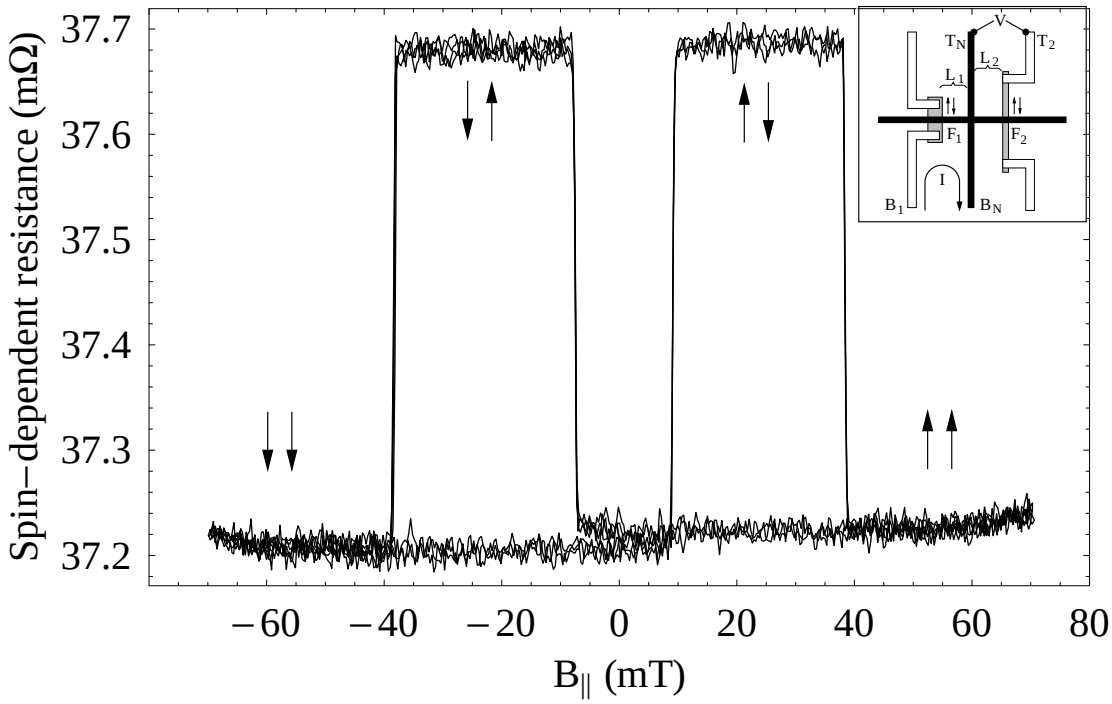

Figure 5.2: R vs $B_{\|}$ for sample sam2b8s1 at 77 K. This sample has transparent Py-Cu contacts. The inset shows a schematic of the sample layout and measurement configuration.

measured signal, this geometry is problematic and should not be used to extract parameters such as the spin diffusion length and the degree of spin polarization.

5.2 Nonlocal geometry configuration

As shown in the previous section the cross geometry is difficult to interpret theoretically since it includes different physical effects. To solve this problem a different geometry was used for the rest of the experiments. The new geometry has the very appealing feature that it is nonlocal, so none of the AMR, Hall effect, or ohmic voltages are part of the measured signal. That is, in the absence of spin injection the expected signal should be exactly zero[2]. I will begin this section by present-

[2]This is not entirely correct, as will be explained later in this chapter when talking about possible artifacts. Local heating coupled with thermoelectric effects can generate spurious voltages,

ing results of the nonlocal resistance as a function of separation between magnetic contacts, from which the spin diffusion length of electrons and the degree of spin polarization can in principle be extracted. Then I will show how particularities of each of the ferromagnetic-nonmagnetic metal contacts can affect the extraction of such quantities, and how a slightly different experiment, based on spin precession (Hanle effect) can be used to extract these numbers with a single measurement. I will then give evidence for the existence of increasing interface spin-flip scattering with temperature, which has been previously unaccounted for, and which appears as a temperature dependent symmetric component of the nonlocal resistance. Finally I will provide additional measurements that were performed to rule out artifacts.

5.2.1 Length dependence of the nonlocal resistance

The nonlocal measurement configuration is depicted in the inset of Fig. 5.3 and was discussed in detail in chapter 3. The nonlocal resistance, defined as $R_{NL} = V_{T_2-N_2}/I_{T_1-N_1}$, can have either of two values, depending on the alignment of the injector and detector magnetizations, $R_{NL}^{\uparrow\uparrow}$ for aligned and $R_{NL}^{\uparrow\downarrow}$ for anti-aligned magnetic contacts [see Eq. (3.29)]. The difference in the value of the nonlocal resistance between the two possible alignments divided by two,

$$R_A = \left[R_{NL}^{\uparrow\uparrow} - R_{NL}^{\uparrow\downarrow}\right]/2, \tag{5.1}$$

the finite input impedance of the amplifiers (lock-in) as well as capacitive leakage between leads can generate small sample dependent background voltages, and wide overlap areas between the magnetic contacts and the normal metal wire can generate small decaying potential drops that can in principle affect the signal. It will be shown, however, that this was not the case in our measurements.

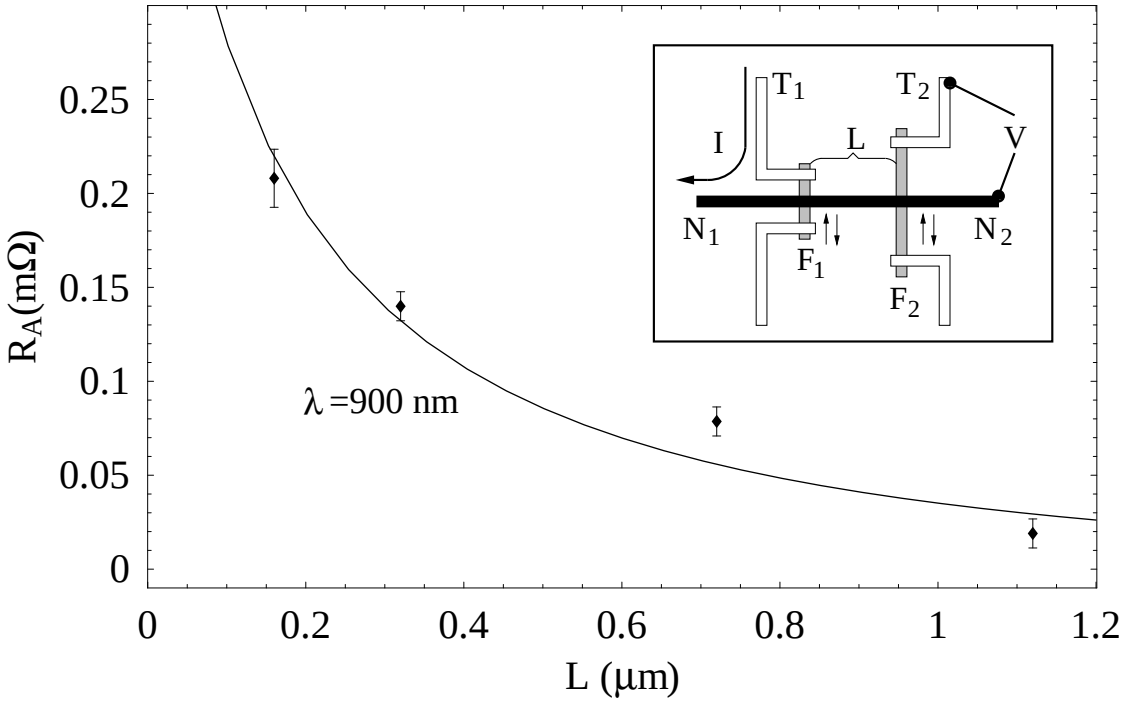

Figure 5.3: Nonlocal resistance switching ($R_A = \left[R_{NL}^{\uparrow\uparrow} - R_{NL}^{\uparrow\downarrow}\right]/2$) as a function of the separation L between injector and detector for sample sam4b1s4, with transparent Py-Cu contacts at 4.2 K.

is related to the spin diffusion length λ by means of equation (3.29), as discussed in the previous chapter. In order to extract the spin diffusion length of electrons in a nonmagnetic metal, samples with varying separation L between injector and detector are fabricated, and the value of R_A is recorded as a function of the separation L. The typical sample layout for these measurements is shown in Fig. 4.3(d), where consecutive magnetic contacts were used as injector-detector pairs.

Figure 5.3 shows the length dependence of R_A for sample sam4b1s4, together with a fit to equation (3.29). This sample has 25 nm thick Py and 48 nm thick Cu lines, and 60 seconds of ion milling with 10^{-4} Torr Ar at 250 V and 5 mA current. The data shows the correct trend of decreasing R_A with increasing L.

The extracted value of the spin diffusion length is 900 nm, which is comparable to previous measurements by different groups [22, 58]. However, a better comparison can be established by calculating the ratio between the momentum and spin scattering times ($a^p = \tau_p/tau$). For our data a^p =2.7×10^{-4}, while for other groups $a^p = 6.9 \times 10^{-4}$ [22] and a^p =3.2×10^{-4} [58]. It must be pointed out that in order to extract λ, the value of the spin diffusion length of electrons in the magnetic material must be known, and since it cannot be measured for the spin valve wires, a reasonable value measured for a different system has to be used [59, 60, 61]. To obtain the best fits shown in Figs. 5.3 and 5.4 we used values of the spin diffusion length in Py between 3nm and 5nm. This is not the only problem. The data is scattered so it cannot be fit well by the model, and since the fitting equation is nonlinear, there is a large set of parameters that can fit the data and have a similar mean square deviation. What this means is that the confidence intervals are large, so the certainty with which it can be claimed that the extracted value of λ is correct is very low.

Figure 5.4 shows two more sets of measurements for samples with different thickness of the Py and Cu wires, and also slightly different milling parameters than those used in Fig. 5.3. Samples sam10b3p1 and sam10b3p3 [Fig. 5.4(a)] have 34 nm thick Py and 41 nm thick Cu lines, with 80 seconds of ion milling with 10^{-4} Torr of argon at 250 V, 100 V accelerating voltage, and 5 mA current. Sample sam12b1p2 [Fig. 5.4(b)] has 48 nm thick Py and 76 nm thick Cu lines, and the same ion milling parameters. The fits to equation (3.29), which give spin relaxation lengths of 920nm

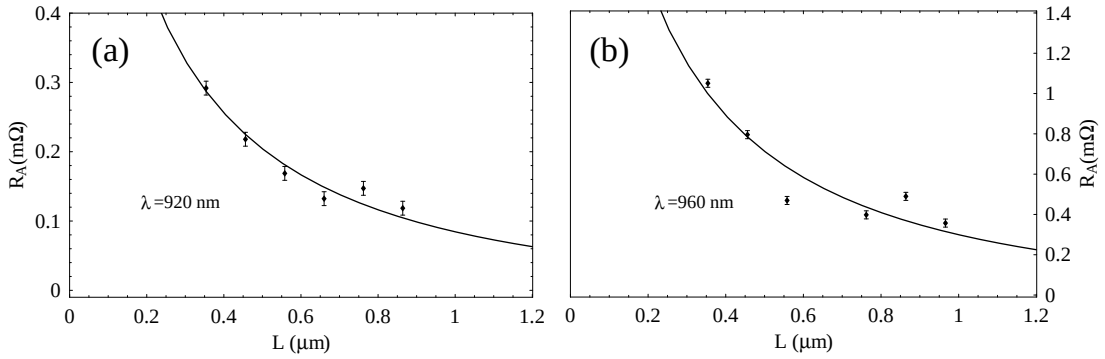

Figure 5.4: Nonlocal resistance switching (R_A) as a function of injector-detector separation L for (a) the average of samples sam10b3p1 and sam10b3p3, and (b) sample sam12b1p2, with transparent Py-Cu contacts at 4.2 K.

(a^p =1.49×10^{-3}) and 960nm (a^p =9.2×10^{-4}), are also shown. The extracted values of λ (and a^p) are also in agreement with the results from previous measurements quoted above, but the scatter in the data still gives confidence intervals which are too large. The scatter in the data is attributed to lack of reproducibility in the contacts between Py and Cu due to differences in the size of the contact area, unremoved resist, and incomplete oxide and surface contamination removal by the ion mill. Efforts to increase sample reproducibility were not completely effective, but the importance of using longer ion mill times and larger line thickness is evident after comparing Figs. 5.3 and 5.4. For longer milling times and thicker Cu wires the size of R_A is larger.

In conclusion, it was shown that although it is in principle possible to extract the spin diffusion length from the length dependence of the spin-dependent resistance, this procedure can have a large systematic error coming from the particularities of each of the Py-Cu contacts. The average value of the spin diffusion length found from the fits is 927 nm (with a^p =8.9×10^{-4}) which is comparable to

values found in the literature[3], but the confidence intervals are large, limiting the credibility of the results. In the next section I will present an alternative method for finding both the spin diffusion length and the degree of spin polarization with a single measurement, evading the issue of contact reproducibility, and yielding more accurate results.

5.2.2 Spin precession: Hanle effect

In this section I will present results of spin precession (Hanle effect) experiments, from which the spin diffusion length and the spin polarization can be determined. All the samples used for this experiments had Co-Al_2O_3-Cu junctions with contact resistances varying between 9 Ω and 1 kΩ, depending on the oxidation parameters. A schematic of the experiment is shown in Fig. 5.5 (b). First the magnetic contacts were aligned by applying an in-plane magnetic field. Then this in-plane field was turned off and an out-of-plane magnetic field $B_\perp$ was applied to induce the precession of the spins as the electrons diffused from the injector to the detector.

Figure 5.5 (a) shows some typical Hanle effect data, together with a fit to the model presented in chapter 3 [equation 3.38]. This particular data is for sample s_sam11b2y1p2, which has a separation of L=425 nm between injector and detector, at a temperature of 4.2 K. As $B_\perp$ increases, the spin, which lies in plane, precesses by a larger angle, and is no longer aligned with the detector, decreasing the magnitude

[3] 1000 nm ($a^p = 6.9\times10^{-4}$) for spin injection by Jedema et. al. [22], 700-1400 nm for energy level spectroscopy by Petta et. al. [62], and 450 nm ($a^p = 3.2\times10^{-4}$) for GMR measurements by Yang et. al. [58]. Conduction electron spin resonance (CESR) measurements give 130 times larger spin relaxation times, but equally larger mean free times, so that the ratio of the two time scales is similar ($a^p = 9\times10^{-4}$) [63, 64].

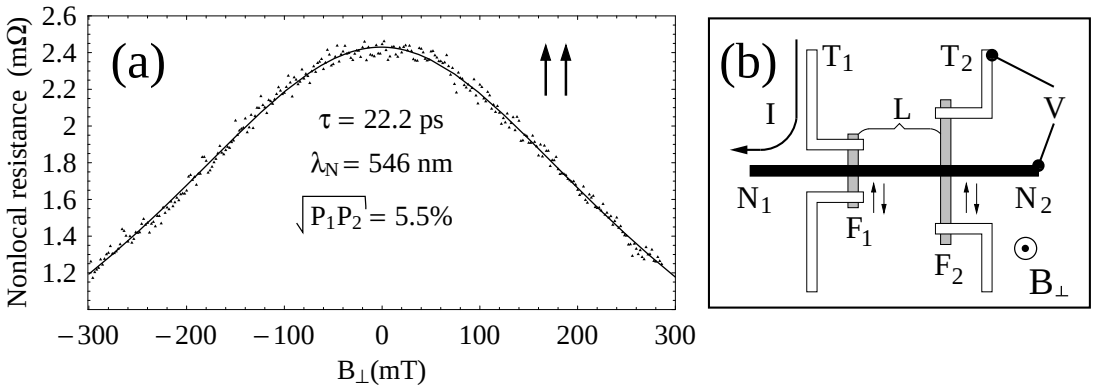

Figure 5.5: (a) Hanle effect measurement of sample s_sam11b2y1p2 at 4.2 K for aligned injector and detector separated by 425 nm; the nonlocal resistance is shown as a function of the out-of-plane magnetic field $B_\perp$. A fit to the data is also shown, together with the fitting parameters τ=22.2 ps and $\sqrt{P_1P_2}$=5.5%. (b) Schematic of the Hanle effect experiment. The nonlocal resistance, defined as $R_{NL} = V_{T_2-N_2}/I_{T_1-N_1}$ for either aligned or anti-aligned magnetizations of injector and detector is measured as a function of the out-of-plane magnetic field $B_\perp$.

of the measured nonlocal resistance. For large enough magnetic fields, the spin can rotate 180 degrees, and the nonlocal resistance can change from positive to negative. However, as $B_\perp$ is increased, the effective magnetization of the injector and detector begins to rotate and starts to have an out-of-plane component, affecting the interpretation of the measurement. This is the main reason to avoid going to higher magnetic fields. Figure 5.5(a) also shows the values of the fitting parameters which are τ=22.2 ps and $\sqrt{P_1P_2}$=5.5%. The spin diffusion length, calculated using $\lambda_N = \sqrt{D\tau}$, is λ_N =546 nm. Although no independent information about P_1 and P_2 can be obtained, their product is known, and if the contacts are assumed to have similar characteristics, then it can be claimed that the current spin polarization at the interface is 5.5%. Furthermore, even without any assumptions it can be inferred that the current spin polarization at one of the interfaces is at least 5.5%,

the geometric mean of P_1 and P_2.

Figure 5.6 shows two complete sets of data (both aligned and anti-aligned configurations of the magnetization of injector and detector) showing the Hanle effect for two different separations between injector and detector at 4.2 K. Parts (a) and (c) are for a separation of 867 nm, while (b) and (d) are for a separation of 1110 nm. The figures on the left are well fit by the same parameters, τ=25.3 ps and $\sqrt{P_1P_2}$=3.8%, while the ones on the right are best fit by slightly different parameters, τ=26.0 ps and $\sqrt{P_1P_2}$=4.3% for aligned, and τ=27.6 ps and $\sqrt{P_1P_2}$=4.6% for anti-aligned. However the difference between them is small. The values of the spin current polarizations and the spin diffusion lengths are comparable to those shown in Fig. 5.5(a). Besides the larger separation between injector and detector, the main difference between these samples and that shown in Fig. 5.5 is that these were oxidized at a pressure of 122 mTorr while the other one was oxidized at a pressure of 410 mTorr.

However there are two important features that should be noticed from Fig. 5.6. The first one is that Fig. 5.6(b) is slightly asymmetric in field. This can be understood from the fact that the magnetization in injector and detector are sometimes not exactly parallel[4]. The zero in-plane field state of the magnetic contacts is that which is a local minimum of the energy stored in the magnetic system. This energy is a function of the domain structure of each contact, which is sensitive to the shape

[4]In the extreme case in which injector and detector are perpendicular to each other, the Hanle effect signal would be completely antisymmetric in field, since for positive fields precession tries to align the spins with the detector, while for negative fields precession tries to align the spins opposite to the detector.

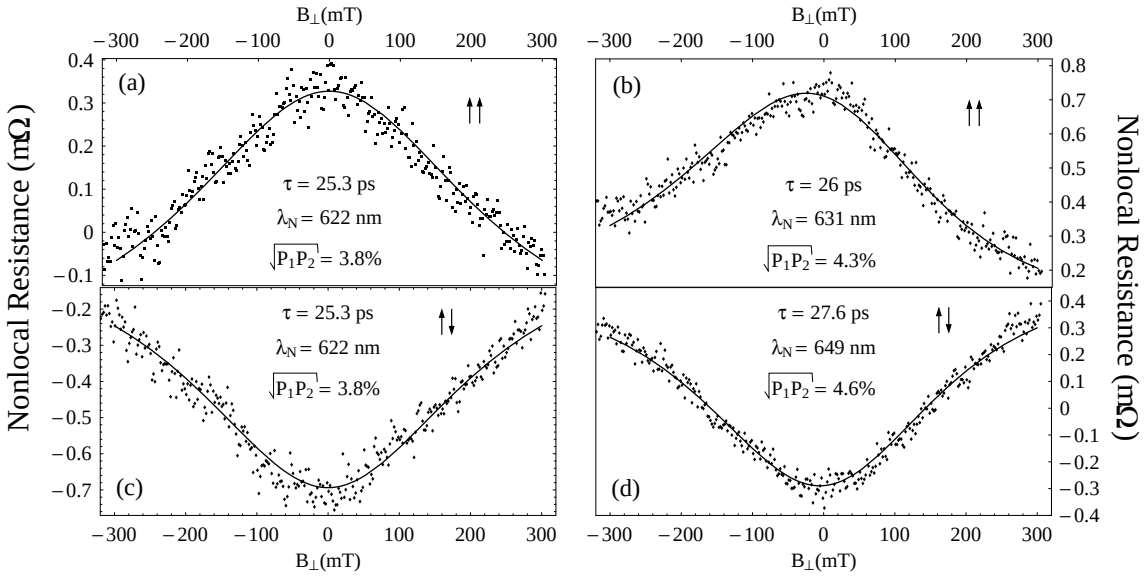

Figure 5.6: Hanle effect measurements and fits for two different injector-detector separations (sample s_sam11b2y3p2) at 4.2 K. (a) 867 nm, aligned injector and detector (↑↑). (b) 1110 nm, ↑↑. (c) 867 nm, ↑↓. (d) 1110 nm, ↑↓.

anisotropy and to the crystalline structure of the material. The fabricated films are polycrystalline so the crystalline structure plays a much smaller role than the shape anisotropy in defining the domain structure of the contacts. In the fabricated samples single domain structure throughout most of the ferromagnetic contacts is expected due to the strong shape anisotropy and the reduced size, but small closure domains at the edges are typical in rectangular shaped structures. This closure domains can be affected by the local crystalline structure which is sample dependent, and can also depend on the history of the magnet. Depending on the details of the closure domains, the magnetization of the contact can be slightly rotated from the main geometrical axis, therefore the magnetization of injector and detector can sometimes be not completely parallel.

The second feature of importance is that the maxima of the data in parts (a)

and (b) have different magnitude than the corresponding minima in figures (c) and (d). This means that there is a shift in the value of the nonlocal resistance which can be positive or negative. This shift can be explained by a small leakage current into the finite input impedance of the lock-in amplifier, and its magnitude and sign depend on the values of the resistance of different sections of the sample, as well as contact, and probe wiring resistances. Simulations using PSPICE (which will be shown later in this chapter) show that the value of this shift is of the order of a few tenths of a milliohm, which gives the correct order for the observed shifts in Fig. 5.6.

Finally, to test the linearity in bias current, Fig. 5.7 shows Hanle effect data for currents of (a) 19.6 μA and (b) 9.8 μA at 4.2 K for sample s_sam12p2 with an injector-detector separation of 717 nm. The fitting parameters are almost identical in both cases, confirming the linearity of the nonlocal resistance on applied bias current. The spin diffusion length is similar but slightly larger than that measured for other samples, but the surprising result is the very high value of the spin current polarization P of 17.2%, compared with other fabricated samples which had P close to 5%, and which is only one half of the value in bulk Cobalt of 35%. The main difference between this and previous samples is that the oxidation pressure was 423 mTorr. Even though this pressure is close to the value of 410 mTorr quoted for sample s_sam11b2y1p2 and shown in Fig. 5.5 which had P of only 5.5 %, it was seen experimentally that the contact resistance was very sensitive to the pressure in the 400 mTorr range. This provides evidence that by controlling the oxidation

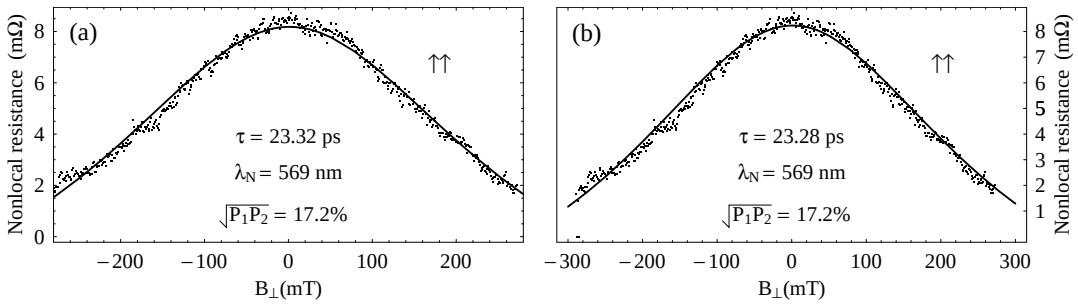

Figure 5.7: Hanle effect measurement for sample s_sam12p2 with injector-detector separation of 717 nm at 4.2 K, for (a) 19.6 μA bias and (b) 9.8 μA bias. Note the large value of the spin current polarization, about three times larger than for other samples, but a comparable spin diffusion length.

pressure precisely in the 400 mTorr range, the spin current polarization can be greatly enhanced.

In conclusion, the spin diffusion length of electrons in Copper was measured to have an average value of 601 nm ± 36 nm (a^p=6.2×10^{-4}), which is comparable to previous results from GMR measurements (450 nm, a^p=3.2×10^{-4}) [58], spin injection (1000 nm, a^p=6.9×10^{-4}) [22], and energy level spectroscopy (700-1400 nm) [62]. These values are smaller than those obtained in the previous section from the length dependence of the nonlocal resistance by roughly a factor of 1.5. However, the ratio of the momentum and spin relaxation times a^p is also smaller, which means that the Hanle effect samples have a higher resistivity than the ones measured before. Spin current polarizations were typically 5% but some samples showed much larger values approaching 20%. The conditions under which samples with very different values of P were fabricated are similar, which shows the extreme sensitivity of the interfacial spin transport to processing details such as the oxidation

parameters, in particular the oxidation pressure.[5].

5.2.3 Symmetric component of the nonlocal resistance

According to the model for spin transport presented in chapter 3, in particular equations (3.31) and (3.34), the nonlocal resistance should have the same magnitude for both aligned and anti-aligned magnetizations of injector and detector, but it should be positive for aligned and negative for anti-aligned magnetizations. In this section I will present data that shows that this is true at low temperatures, but at higher temperatures there is an offset or symmetric component of the nonlocal resistance which is also related to spin transport, and which can be explained by different interface spin-flip scattering for spin $\uparrow$ and spin $\downarrow$ electrons at the detector (F_2) interface.

The temperature dependence of the nonlocal resistance was measured for the two possible injector-detector configurations. First an in-plane magnetic field was used to align injector and detector ($\uparrow\uparrow$). Then the field was turned off and the temperature was changed from room temperature down to 77 K and back up to room temperature. The in-plane field was then turned on to align injector and detector in opposite directions ($\uparrow\downarrow$). The field was then turned off and the temperature was again oscillated slowly between room temperature and 77 K. Due to temperature instability close to liquid nitrogen temperature, only the data above

[5]Some factors that can affect spin transport at the interface are antiferromagnetic oxide formation, magnetic fields produced by inhomogeneities in the magnetic material at the interface, spin-flip scattering, varying oxide thickness, or even contact potentials that can affect the local density of states of the metals. However, understanding this details is outside of the scope of this work.

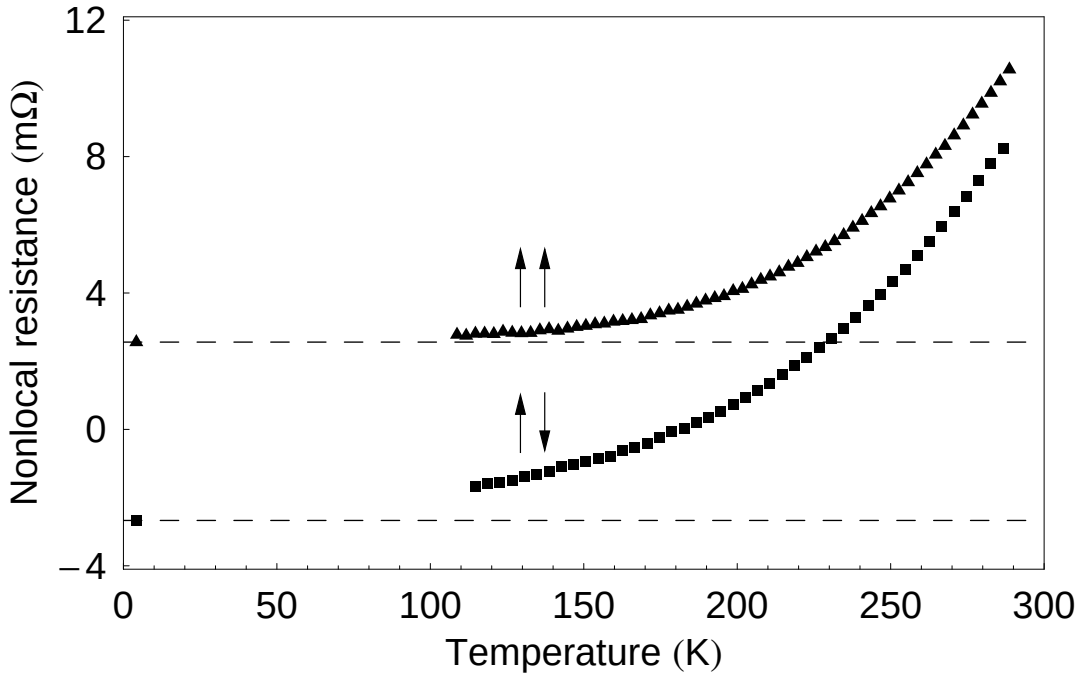

Figure 5.8: Temperature dependence of the nonlocal resistance for aligned (↑↑) and anti-aligned (↑↓) magnetizations of injector and detector for sample s_sam11b2y1p2 with an injector-detector separation of 425 nm. Dashed lines show the 4.2 K values.

100K are shown. Figure 5.8 shows typical traces of the temperature dependence of the nonlocal resistance for both configurations, with the dashed lines representing the values measured at 4.2 K.

At 4.2 K the values of the nonlocal resistance for the two different configurations have the same magnitude but different sign, as expected from the model. However, at 115 K it is clear that this is no longer true and both values have shifted in the positive direction. As the temperature is increased further, the offset increases nonlinearly and at room temperature it is more than three times larger than the low temperature value of the nonlocal resistance. For comparison, the temperature dependence of the resistivity of both copper and cobalt was measured, as well as the temperature dependence of the contact resistance. The results are shown in

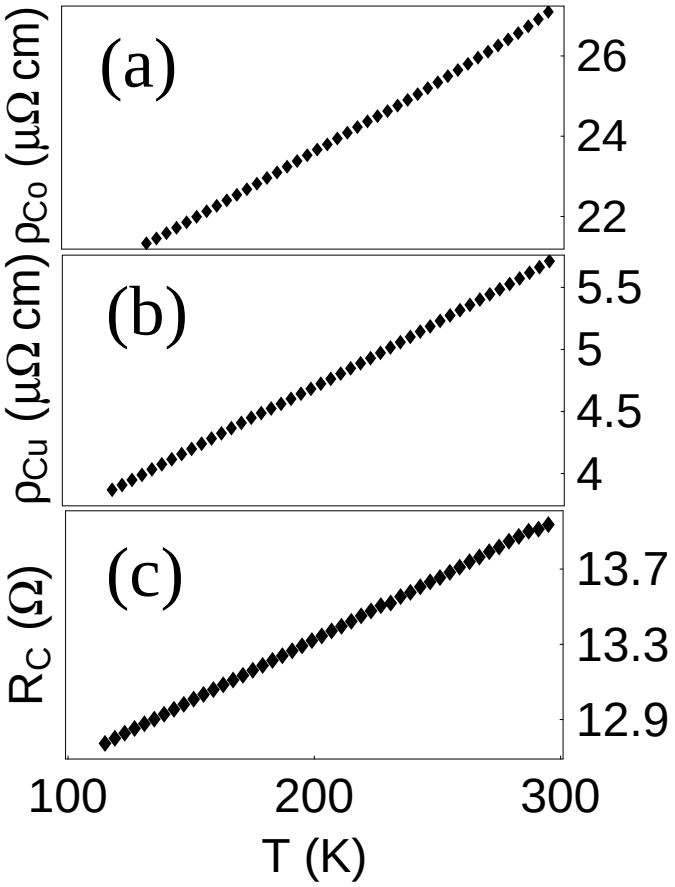

Figure 5.9: Temperature dependence of (a) the resistivity of Co, (b) the resistivity of Cu, and (c) the contact resistance.

Fig. 5.9. They all show a linear increase with temperature in the 100-300 K range, which rules out many resistive effects as a possible origin for the nonlinear increase in both $R_{NL}^{\uparrow\uparrow}$ and $R_{NL}^{\uparrow\downarrow}$. In order to understand this better, the symmetric ("+") and anti-symmetric ("-") components of the nonlocal resistance

$$R_{S,A} = (R_{NL}^{\uparrow\uparrow} \pm R_{NL}^{\uparrow\downarrow})/2, \tag{5.2}$$

are shown in Fig. 5.10. From this figure it is clear that the antisymmetric component of the nonlocal resistance (R_A), which is the only one that had been studied up

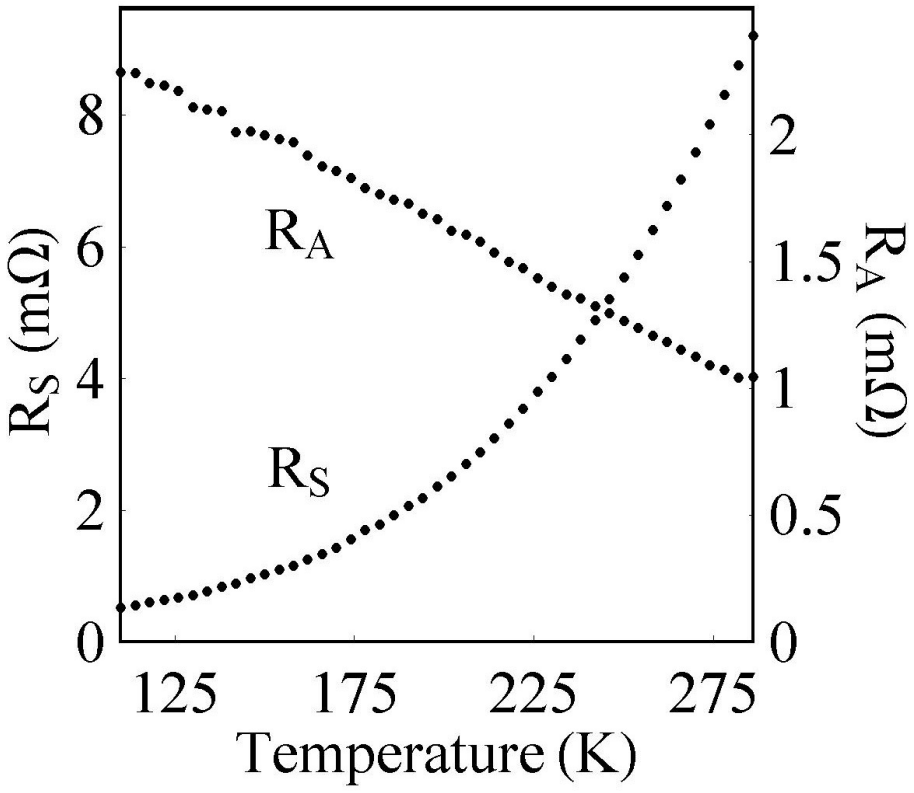

Figure 5.10: Symmetric and anti-symmetric components of the nonlocal resistance as defined in equation (5.2), for the data shown in Fig. 5.8.

to now[6], decreases linearly with increasing temperature in the 100 K to 300 K range. However, the symmetric component, which had not been observed up to now, increases nonlinearly in that temperature range. As opposed to the antisymmetric component, the symmetric one is by definition that component which is independent of the relative alignment of injector and detector. This indicates a possibly different origin for the two signals, which does not mean that the symmetric component is not related to spin-transport, and evidence will be given to support the claim that

[6]With Tunnelling Magneto Resistance (TMR) geometries only R_A can be measured since even in the absence of spin effects there is a large symmetric component or offset arising from resistive effects.

it is in fact related.

The transport model described by equations (3.29), (3.31), and (3.34) cannot explain the existence of R_S since they predict a vanishing symmetric component of the nonlocal resistance. However, if interface spin-flip scattering takes place, these equations are no longer valid, and it is necessary to generalize them to include spin non-conserving currents at the different interfaces. This was done in the last section of chapter 3, where the relevant equations (3.40) and (3.41) were deduced. It was shown that for certain kinds of spin-flip scattering the nonlocal resistance could have an additional component which did not reverse its sign when the magnetization of the injector was reversed, and which was due to the difference between $P_2^{\uparrow\uparrow}$ and $P_2^{\uparrow\downarrow}$. This would allow the existence of a symmetric component of the nonlocal resistance. A detailed discussion follows.

Phenomenology and analysis of R_A and R_S

In the limit of large contact resistances the model discussed in chapter 3 predicted that the nonlocal resistance would be given by [see equation (3.34)]

$$R_{NL} = \pm\frac{1}{2A_N}\rho_N\lambda\exp(-L/\lambda)P_1P_2, \tag{5.3}$$

where P_1 had the physical significance of being the spin current polarization at the detector interface, while the "+" or "-" signs applied to aligned ($\uparrow\uparrow$) or anti-aligned ($\uparrow\downarrow$) injector and detector. The product $\rho_N\lambda/2A_N\exp(-L/\lambda)$ is related to the spin transport in the nonmagnetic material therefore it should be the same for $\uparrow\uparrow$ and $\uparrow\downarrow$. Additionally, the value of P_1, the spin current polarization at the injector, is

independent of the direction of magnetization of the detector, $P_1 \equiv P_1^{\uparrow\uparrow} \equiv P_1^{\uparrow\downarrow}$. On the other hand since the detector can be aligned or anti-aligned with the injector, transport across the detector interface can be characterized by different values of P_2, namely $P_2^{\uparrow\uparrow}$ for aligned and $P_2^{\uparrow\downarrow}$ for anti-aligned. Therefore by using equation (5.3), $R_{S,A} = (R_{NL}^{\uparrow\uparrow} \pm R_{NL}^{\uparrow\downarrow})/2$ can be rewritten as

$$R_{S,A} = \frac{1}{2A_N}\rho_N \lambda \exp(-L/\lambda) P_1 P_{S,A}, \tag{5.4}$$

with the definition

$$P_{S,A} = (P_2^{\uparrow\uparrow} \pm P_2^{\uparrow\downarrow})/2, \tag{5.5}$$

where the "+" ("-") sign refers to the symmetric (antisymmetric) component of P_2. It is possible to analyze the temperature dependence of equation (5.4) further as follows. The term "ρ_N" (the resistivity of copper) was measured in the 100 K - 300 K temperature range as shown in Fig. 5.9(b). The relaxation length λ (which appears both as a multiplying factor and in the exponential term) can be related to the spin relaxation time τ by using the diffusion relation $\lambda = \sqrt{D\tau}$. According to Elliot and Yafet [5, 4] and as discussed in chapter 2, the spin relaxation time is proportional to the momentum relaxation time τ_p. The proportionality constant is temperature independent at high temperatures, where the dominant source of both momentum and spin relaxation is phonons. By using equation (2.4) it is then possible to relate λ to τ_p by

$$\lambda = \sqrt{D\tau_p/a^p}. \tag{5.6}$$

The momentum relaxation time can be calculated in terms of the resistivity by using the Drude model to give

$$\lambda(\rho_N) = \sqrt{\frac{m^* D}{ne^2 a^p \rho_N}}, \tag{5.7}$$

where m^* is the effective mass of electrons in copper, n is the Cu electron density, and e the proton charge. This means that, up to the constant a^p, the temperature dependence of λ can be obtained from the measured temperature dependence of ρ_N in the 100-300K temperature range. At low temperatures the value of a^p can be calculated from our previous measurements of the spin relaxation time and the resistivity of copper at 4.2 K. However, since the scattering mechanisms responsible for momentum and spin relaxation at high temperatures are different from those at low temperatures, a^p should be treated as a fitting parameter. Additionally, the temperature dependence of the term "P_1", the injector spin current polarization, has the form $P_1 = P_0(1 - \eta T^{3/2})$ [65],[7] with the additional fitting parameter η. The value of η is known for bulk but since the injected spin polarization is an interface effect, values much larger than those for bulk are expected. The value of P_0 (5.5%) was measured by using Hanle effect in the previous section. It has been shown [65] that the previously observed P_A has the same temperature dependence as that of

[7]Spin waves in ferromagnetic materials are responsible for the decrease of the magnetization as the temperature increases with the dependence $M = M_0(1 - \eta T^{3/2})$ [66]. If the spin current polarization is assumed to be proportional to the magnetization, the temperature dependence of M should be reflected in P.

the injector. Therefore the functional form of the temperature dependence of the right hand side of R_A in equation (5.4) is known up to two unspecified constants a^p and η. This functional form, given explicitly by

$$R_A = \frac{1}{4A_N} P_0^2 (1 - \eta T^{3/2})^2 \lambda(\rho_N) \rho_N \exp(-L/\lambda(\rho_N)), \tag{5.8}$$

where $\lambda(\rho_N)$ is given by equation (5.6), can be used to fit the data for R_A shown in Fig. 5.10 using a^p and η as fitting parameters. The values obtained from the fit are a^p=6.6×10^{-4} which is 1.06 times larger than the value of a^p measured at 4.2K and agrees very well with the results of Jedema et. al [22] (6.9×10^{-6}), and η =8.4×10^{-5}K$^{-3/2}$, which is, as expected, larger than in bulk [65][8].

Once the parameters a^p and η have been found from the fit, it is possible to calculate P_A and P_S by inverting equation (5.4) since the temperature dependence of all the additional terms is determined by the two fitting parameters. The result of such calculation is shown in Fig. 5.11. The temperature dependence of P_A and P_S is similar to that of R_A and R_S due to the almost linear temperature dependence of the additional factors in equation (5.4). Furthermore P_A is fit well by the assumed form $P_0(1-\eta T^{3/2})$, which confirms the correct choice of fitting function. Additionally R_S can be fit by a Fermi function $B/(1+\exp T_0/T)$ with an activation temperature T_0 of 1227K.

[8]The magnetization, and therefore the spin polarization, is more robust in bulk than at the interfaces, where the ferromagnetic state is more sensitive to thermal effects.

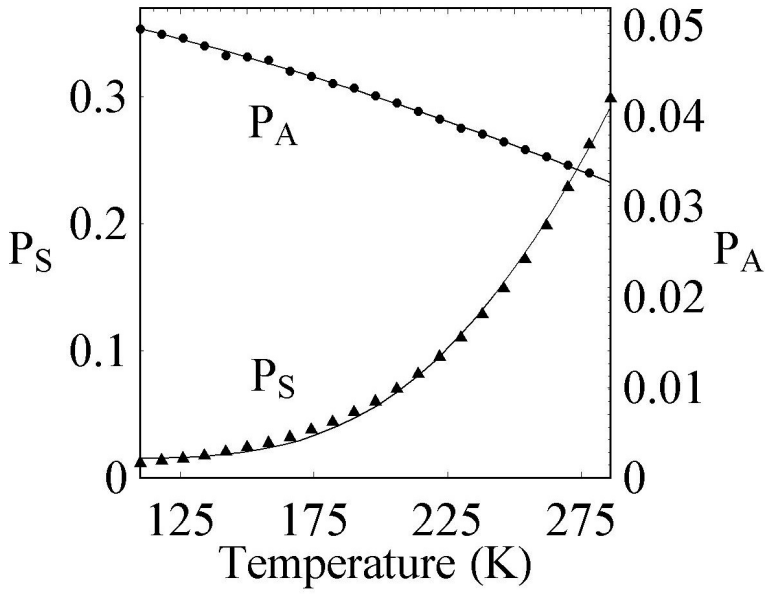

Figure 5.11: Temperature dependence of P_A and P_S together with fits to $P_0(1 - \eta T^{3/2})$ (with P_0=5.5% and η=8.4×10^{-5}K$^{-3/2}$) and a Fermi function $B/(1 + \exp T_0/T)$ with an activation temperature of T_0=1227K.

Theory and physical interpretation of P_A and P_S

In the absence of spin-flip scattering at the interfaces, both the charge and spin current are conserved. In this case the boundary conditions given by equation (3.15) and the corresponding schematic shown in Fig. 3.2 describe transport at each interface. However, it was shown in chapter 3 that in the case of interfacial spin-flip scattering the correct boundary conditions were given by equations (3.39) and the corresponding schematics shown in Fig. 3.11. By using this new set of boundary conditions it was shown that the nonlocal resistance was given by the same expression as the one used in the absence of interfacial spin-flip scattering, namely equation (5.3), with redefined constants P_i $(i = 1, 2)$. The general expressions for the P_i were not very enlightening [see equations (3.41)]. However, assuming that

the spin-conserving interfacial resistances (R_σ) depend only on the magnetization of the ferromagnet, and that the spin-flipping interfacial resistances depend on the nonequilibrium magnetization in the nonmagnetic metal, it is possible to simplify equations (3.41) to obtain[9]

$$\begin{aligned} P_1 &= \frac{(1/R_{1\uparrow} - 1/R_{1\downarrow})}{(1/R_{1\uparrow} + 1/R_{1\downarrow}) + (1/R^*_{1\uparrow} + 1/R^*_{1\downarrow})} \\ P_2^{\uparrow\uparrow} &= \frac{(1/R_{2\uparrow} - 1/R_{2\downarrow}) + (1/R^*_{2\uparrow} - 1/R^*_{2\downarrow})}{(1/R_{2\uparrow} + 1/R_{2\downarrow}) + (1/R^*_{2\uparrow} + 1/R^*_{2\downarrow})} \\ P_2^{\uparrow\downarrow} &= \frac{-(1/R_{2\uparrow} - 1/R_{2\downarrow}) + (1/R^*_{2\uparrow} - 1/R^*_{2\downarrow})}{(1/R_{2\uparrow} + 1/R_{2\downarrow}) + (1/R^*_{2\uparrow} + 1/R^*_{2\downarrow})}. \end{aligned} \tag{5.9}$$

Therefore the symmetric and antisymmetric combinations $P_{S,A} = (P_2^{\uparrow\uparrow} \pm P_2^{\uparrow\downarrow})/2$ are given explicitly by

$$\begin{aligned} P_S &= \frac{(1/R^*_{2\uparrow} - 1/R^*_{2\downarrow})}{(1/R_{2\uparrow} + 1/R_{2\downarrow}) + (1/R^*_{2\uparrow} + 1/R^*_{2\downarrow})} \\ P_A &= \frac{(1/R_{2\uparrow} - 1/R_{2\downarrow})}{(1/R_{2\uparrow} + 1/R_{2\downarrow}) + (1/R^*_{2\uparrow} + 1/R^*_{2\downarrow})}. \end{aligned} \tag{5.10}$$

The denominator of both of these equations is proportional to the inverse of the contact resistance, which was measured (see Fig. 5.9) and found to be almost constant in the 100-300K temperature range. This means that it is the temperature behavior of the numerators of both of equations (5.10) which causes the particular temperature dependence of P_S and P_A shown in Fig. 5.11. The physical significance of the quantities P_A and P_S can now be understood from equation (5.10). P_A gives the ratio of spin-polarized to total transport from Cu into F_2 (the detector). This

[9]The following P's have been defined so that the $\pm$ sign in front of equation (5.3) should not be used, since it has already been included into the new definition of P_2.

new interpretation clarifies that at low temperatures P_2 gives a measure of the spin polarized transport that differs from the spin current polarization, which diverges due to the absence of charge current. In addition, P_S provides information on the ratio of differential spin-flipping to total transport from Cu into the detector. In other words, it compares the spin-flip transport of the two spin channels, normalized by the total transport across the $N - F_2$ interface. Therefore as the temperature increases up to 300 K, the amount of spin polarized transport from Cu to the detector decreases to about 3%, while the difference in spin-flipping transport of spin $\downarrow$ and spin $\uparrow$ increases to about 30%. This can be expected since it has been shown that in some ferromagnetic materials the mean free path of majority electrons is more than 80% larger than the mean free path of the minority electrons [67].

In conclusion, the existence of spin-flip scattering at the interface can explain the symmetric component of the nonlocal resistance observed in the measurements. Since interfacial spin-flip scattering increases with temperature, it is expected that the symmetric component of the nonlocal resistance also increases with temperature, as confirmed by the measurements. The new observed component of the nonlocal resistance, R_S, is fit well by a Fermi function, typical for thermally activated mechanisms, which further confirms the proposed explanation of enhanced interfacial spin-flip.

In order to check for possible artifacts as the origin of R_S, its dependence on the separation between injector and detector was measured. Temperature and length dependence measurements of nonmagnetic control samples were also done.

Additionally, tests were performed to rule out thermoelectric effects produced by local sample heating, geometric electrostatic effects, current leakage through the input impedance of the lock-in amplifiers, resistive leakage in the probe wiring, capacitive leakage, DC and second harmonic leakage of signal into the lock-in amplifiers, and out of phase detection due to dephasing. In the following sections I will describe these measurements and tests and give their results.

5.2.4 Length dependence of R_S

Figure 5.12 shows the symmetric component of the nonlocal resistance as a function of the separation L between injector and detector for two different samples, one (a) with transparent Py-Cu contacts and seven working magnetic contacts, the other (b) with transparent Co-Cu contacts and eight working magnetic contacts. Measurements were taken at room temperature. Each of the different symbols in Fig. 5.12 represents a different injector, and for a given injector the signal is measured at detectors placed at different distances from the injector. For many of the measurements there are intermediate magnetic contacts between injector and detector. As L increases the value of R_S decreases, as expected for a signal that is related to spin injection. Furthermore, the length dependence of the data is fit well by the model discussed in chapter 3 for transparent interfaces which was used to fit the decay of the antisymmetric component of the nonlocal resistance R_A. The fits give decay lengths λ_S of 875 nm and 943 nm for the samples shown in (a) and (b) respectively[10]. The values of λ_S are close to the average value of the spin diffusion length measured

[10]Fits to the data for a single injector gave similar values of the fitting parameters as those obtained by fits to all of the data.

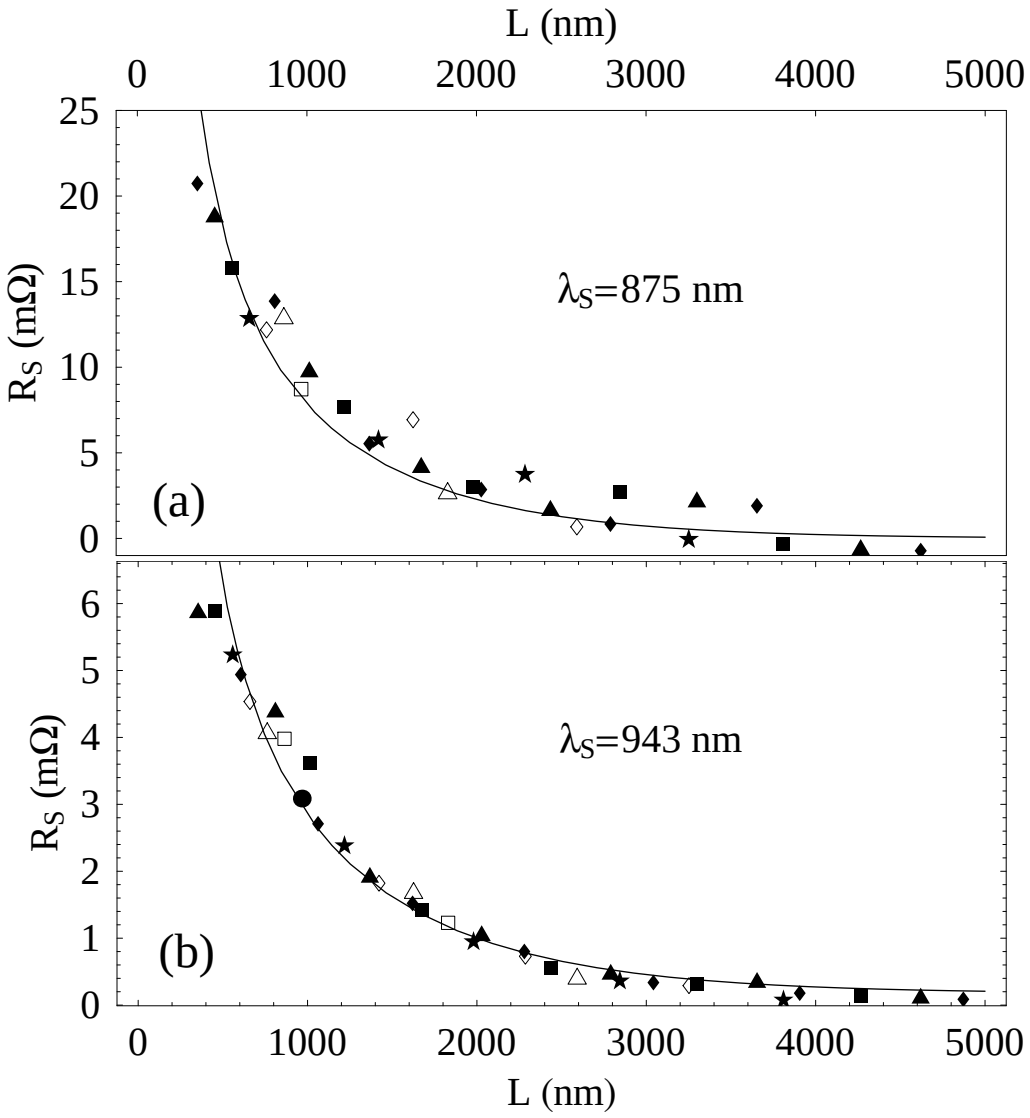

Figure 5.12: Injector-detector separation (L) dependence of the symmetric part of the nonlocal resistance R_S for transparent samples with (a) Py-Cu interfaces (s_sam10b3) and (b) Co-Cu interfaces (s_sam10b1p1) at room temperature.

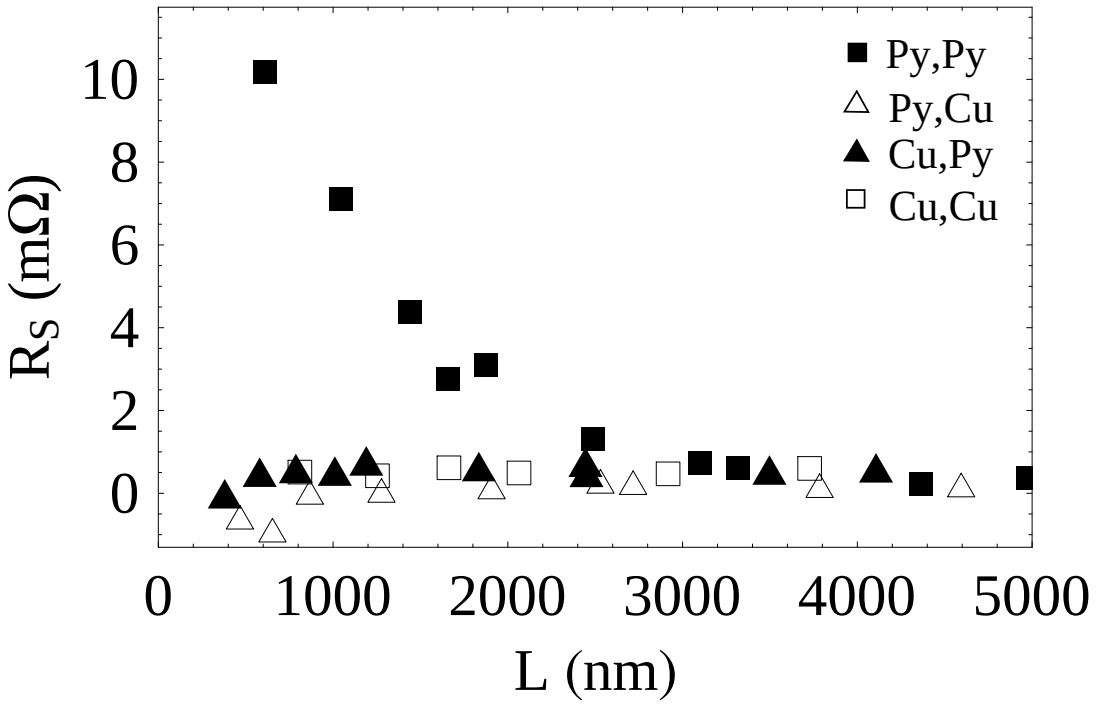

Figure 5.13: Injector-detector separation (L) dependence of the symmetric part of the nonlocal resistance R_S for transparent samples with either Py-Cu or Cu-Cu interfaces. Measurements for samples with Py injector and detector (Py,Py), Py injector and Cu detector (Py,Cu), Cu injector and Py detector (Cu,Py), and Cu injector and detector (Cu,Cu) are shown.

in section 5.2.1 by studying the dependence of R_A on L (927 nm), and are roughly 50% larger than the average value measured using Hanle effect (601 nm). The fact that length dependence measurements of both R_S and R_A give similar decay lengths provides evidence that both components are spin-related. Further evidence that R_S is related to spin is provided by Fig. 5.13, which shows measurements similar to those shown in Fig. 5.12, but with injector and detector fabricated of different materials. Only the measurements on samples with both magnetic injector and detector show length dependence of R_S, while the remaining measurements where either or both of the magnetic contacts were replaced for Cu showed no length dependence.

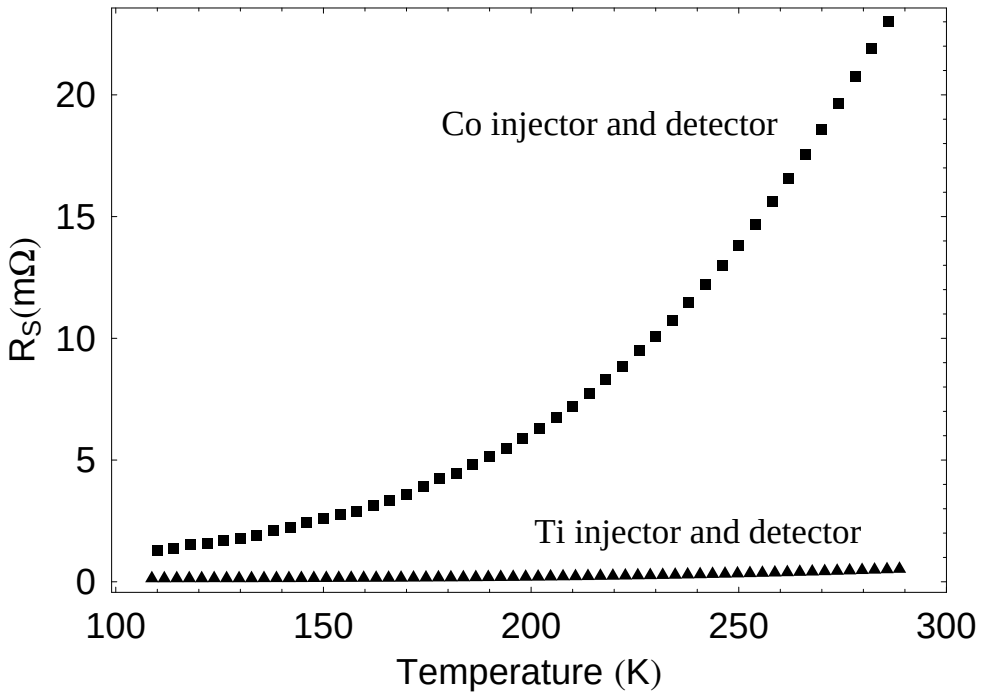

Figure 5.14: Comparison of the temperature dependence of R_S for a sample with magnetic injector and detector, and a control sample with nonmagnetic Ti electrodes.

5.2.5 Temperature dependence of R_S for a control sample

Control samples were fabricated by replacing both the magnetic injector and detector by titanium (Ti). The typical resistance of the Ti-Cu contact was about 80Ω, about 6 times larger than the contact resistance of many of the Co-Cu samples that showed a nonlinear R_S. With the same setup that was used to measure the mentioned Co-Cu samples, temperature dependence measurements of the symmetric nonlocal resistance R_S were performed on the Ti-Cu control sample. A comparison of the results of the two measurements is shown in Fig. 5.14. The symmetric nonlocal voltage V_S is shown instead of the nonlocal resistance R_S. The control sample shows a very small temperature dependence, two orders of magnitude smaller than that of

the Co-Cu sample, confirming that the signal is related to spin. As will be argued later, it also shows that geometric effects are not an issue in our measurements.

5.2.6 Heating and thermoelectric effect

If two different metals which are in contact with each other are at different temperatures, an electric potential difference appears between them [Fig. 5.15 (a)]. This is known as thermoelectric effect, thermopower, or Seebeck effect. The thermoelectric voltage between points A and B in Fig. 5.15 (a) is given by

$$V_A - V_B = \int_A^B S(x)\nabla T(x)\, dx, \tag{5.11}$$

where $S(x)$ is the Seebeck coefficient, which depends on position since it is different for different metals, and $T(X)$ is the temperature throughout the two metals.

The possibility of heating effects appearing as an additional voltage in the measured nonlocal signal can be understood as follows. Figure 5.15 (b) shows a schematic of a typical device together with the path of the current and the voltage probe locations. The gray regions depict ferromagnetic contacts while the white ones represent the nonmagnetic metal wires. Since the resistivity of the magnetic materials used is larger than that of the normal metal, most of the Joule heating (I^2R) will occur in the path of the current before point A. The temperature should therefore be highest in this region and decrease with the distance from point A. Points D and E are far away from the heated area and should therefore be at the same temperature. However points B and C are close to A so they can be at a different temperature, which depends on the details of heat diffusion in the sample.

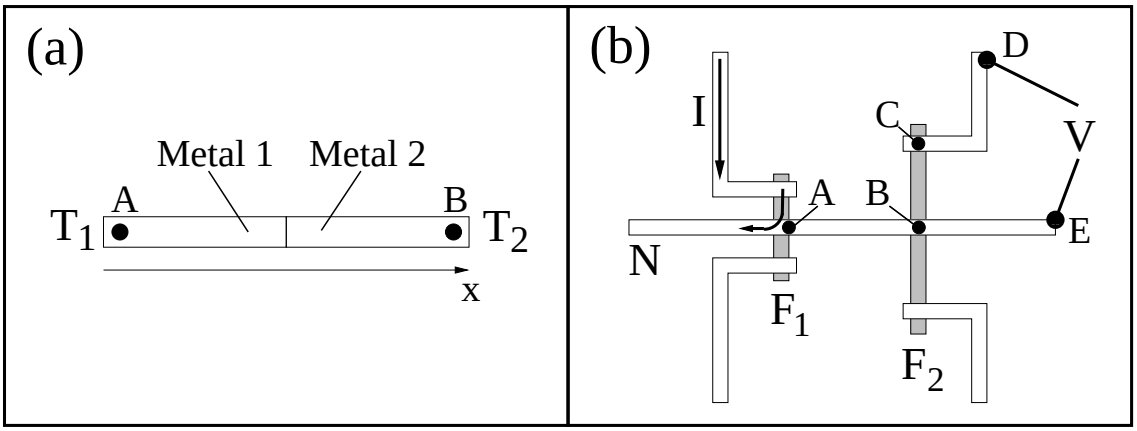

Figure 5.15: (a) Schematic of Seebeck effect with two dissimilar metals. (b) Schematic of a typical sample to illustrate the possibility of measuring heating-related voltages.

If the segment between B and C was also a normal metal, then from equation 5.11 it is clear that $V_B - V_E = V_B - V_D$ since the Seebeck coefficient would be position independent. But since segment B-C is made of a magnetic material with a different Seebeck coefficient than that of copper, then $V_D - V_E \neq 0$ and a heating-related voltage might appear between the voltage probes. The thermal mass of the system is small so the thermal response is fast. Simplified calculations show that the thermal response time is much shorter than the period of the AC drive current, so the temperature and therefore the Seebeck voltage have the same time dependence as the heating, proportional to I^2. Assuming that the current drive has both DC and AC components, the heating-related voltage that appears between points D and E is given by

$$V_S = V_D - V_E \propto (I_{DC} + I_{AC}(t))^2$$
$$\propto (I_{DC}^2 + I_{AC}^2/2) + 2I_{DC}I_{AC}\sin\omega t - I_{AC}^2\cos(2\omega t)/2. \quad (5.12)$$

The first term in the second line of equation 5.12 appears at DC, the second one appears at the fundamental, and the last one shows up at the second harmonic and is 270 degrees out of phase. In principle lock-in measurements are only sensitive to the fundamental component (and to odd harmonics), so the only term that could be measured is $2I_{DC}I_{AC}\sin\omega t$. However, to make sure none of the other terms could be measured, the DC and 2ω rejection of the lock-in was tested, confirming that this signals can only contribute to at most 1 nv lock-in output, which is two orders of magnitude smaller than the observed symmetric component of the nonlocal resistance R_S, and can therefore be completely disregarded when measuring at the fundamental frequency. To study the remaining component of the heating signal, differential resistance measurements were performed. A relatively small AC current with a rms amplitude of either 672 nA or 1344 nA was added to a DC current which was changed between -30 and 30 μA, and the nonlocal voltage was measured at the AC frequency of the current. The result of the measurement is the differential resistance

$$R(I_{DC}) = \frac{\partial V}{\partial I}\Big|_{I_{DC}} \tag{5.13}$$

times I_{AC}. Figure 5.16 shows the measurement results together with linear fits. The triangles (squares) and solid (dashed) line are for an AC bias current of 672 nA (1344 nA). The data are fit well by a line with non-vanishing slope and intercept, which means that the I-V curve has linear plus quadratic behavior. The quadratic term in the I-V curve (the linear term in I_{DC} in the fits) can be attributed to heating together

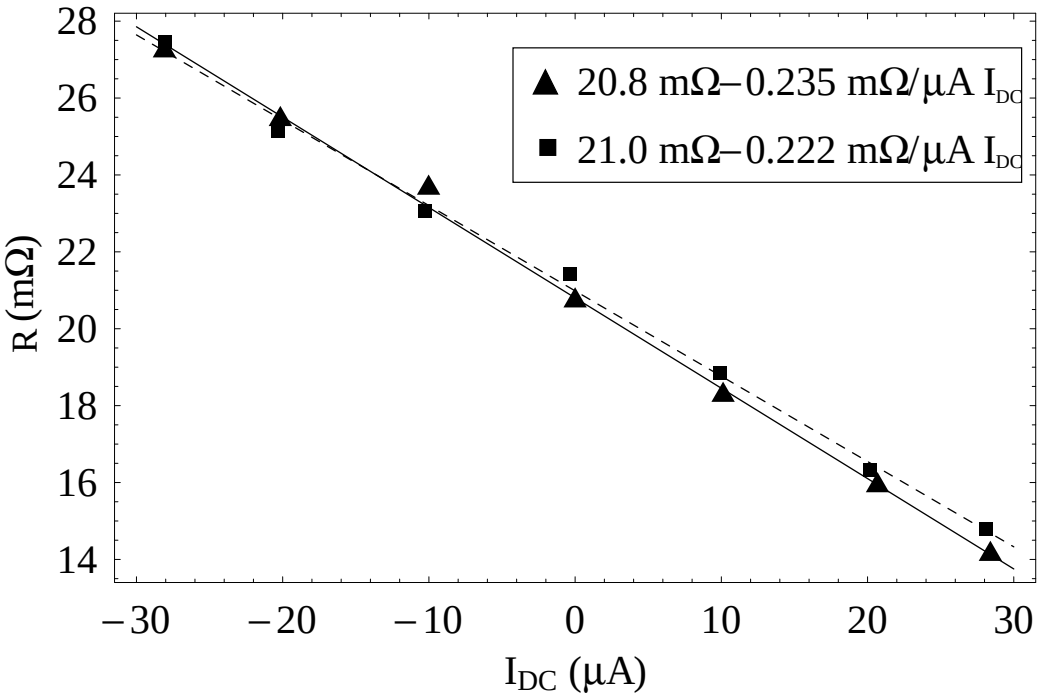

Figure 5.16: Differential resistance R as a function of the DC bias current for AC bias currents of 672 nA (triangles) and 1344 nA (squares), together with linear fits. The solid (dashed) line is the result of the fit to the 672 nA (1344 nA) data.

with thermoelectric effects, but the linear term in the I-V curve (the constant term in the fits) cannot. Furthermore, the heating effect is much smaller than the other part of the measured signal for small currents, and even for currents of 20 μA it is less than 11% of the measured signal. This is the first piece of evidence that shows that heating cannot explain the results of the measurements, since even though it can be present, it does not give the main contribution to the measured signal. According to equation 5.12, heating can be observed at the second harmonic. Since no spin-related signal is expected at that frequency, measurements at the second harmonic should only give a heating-related signal. Lock-in measurements (as well as spectrum analyzer measurements) were made to test this, and the result, $-0.243 m\Omega/\mu A\ I$

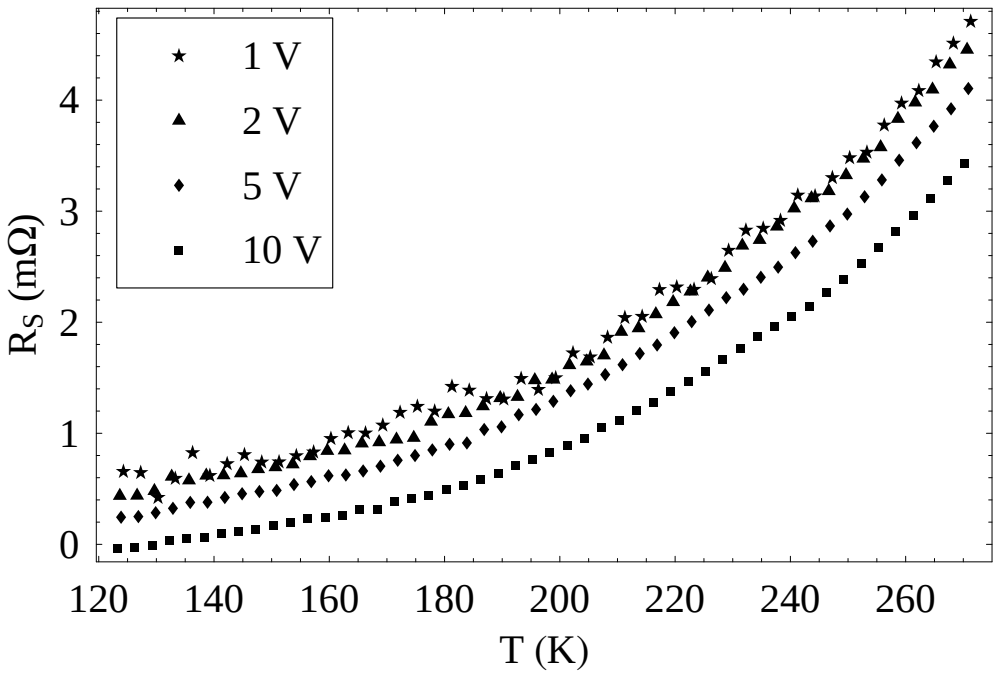

Figure 5.17: Temperature dependence of R_S for four different bias conditions as indicated in the text.

agrees well with that from the differential resistance measurements, confirming the presence of small heating-effects that cannot account for the observed symmetric component of the nonlocal resistance.

As a final test of the effects of heating, the temperature dependence of R_S was measured for four different bias conditions, as shown in Fig. 5.17. The bias conditions are the following:

Bias Label	I_{AC} (μA)	I_{DC} (μA)
1 V	9.8	4.9
2 V	19.6	9.8
5 V	49	24.5
10 V	98	49

Table 5.1: Bias parameters. The first column contains the applied voltage bias, the second column the AC current bias, and the last one the DC current bias.

According to equation (5.12) any heating component observed at the fundamental frequency should be proportional to the product of I_{DC} and I_{AC}. This means that any heating-related component of the nonlocal resistance should be proportional to the DC current. However, Fig. 5.17 shows that for different DC biases the curves are almost exactly the same. For the bias conditions 1 V and 2 V the curves are indistinguishable. For 5 V, the curve has almost exactly the same shape but is shifted towards negative values by a small amount, and for 10 V the shift is larger and the shape of the curve is slightly different at the highest temperatures but has not changed significantly. What this means is that only at high biases it is possible to see heating effects, and they appear as shifts in the baseline that are almost temperature independent. Furthermore, significant heating occurs only for large AC and DC biases, and since in the typical measurement setup no DC current is applied, heating and thermoelectric effects cannot account for the observed symmetric component of the nonlocal resistance and its temperature dependence.

Finally, non-magnetic samples with Ti-Cu and AuGe-Cu interfaces were fabricated and measured under the same conditions as other magnetic Py-Cu and Co-Cu samples. Even though the contact resistances for the Ti-Cu samples were around 76 Ω, larger than the contact resistance of any other sample for which R_S was measured, the measured nonlocal voltage was less than 10 nV for all the Ti-Cu samples and was almost temperature independent, supporting the idea that R_S comes from spin injection and detection rather than from heating and thermoelectric effects. AuGe-Cu and Cu-Cu samples also showed null results.

5.2.7 Geometric effects

Another important issue that must be taken into account when designing spin valve devices, is the effect of the geometry and electrostatics in the measured signal. Figure 5.18 shows a simplified two dimensional picture of the electric field lines (or current lines) and equipotential lines for a cross geometry when the current flows between adjacent arms. The equipotential lines extend a certain distance l_g to the bottom and left arms of the cross, even though the net current flowing through this sections is zero. This means that there is a nonzero potential difference between points A (close to the cross) and B (far away from it). Therefore to avoid additional voltages in spin valve measurements, the characteristic decay length for this equipotential lines, l_g, should be shorter than the separation between injector and detector. The value of l_g is related to the width of the arms of the cross. Detailed calculations for our particular structures were not made, but according to the calculations of Takahashi et. al. [26], the width of the wires was small enough compared to the separation between injector and detector such that geometric effects were not important. A supporting argument to disregard this effect is the fact that the resistivity of Co and Cu and the contact resistance depend linearly on temperature as shown in Fig. 5.9, and any electrostatic voltage should be linear in this variables, therefore no nonlinear temperature dependence is expected for this effect, contrary to the observed R_S which is nonlinear in temperature.

More evidence that the observed nonlocal resistance does not come from electrostatic effects is given by the fact that the Ti-Cu samples that were fabricated

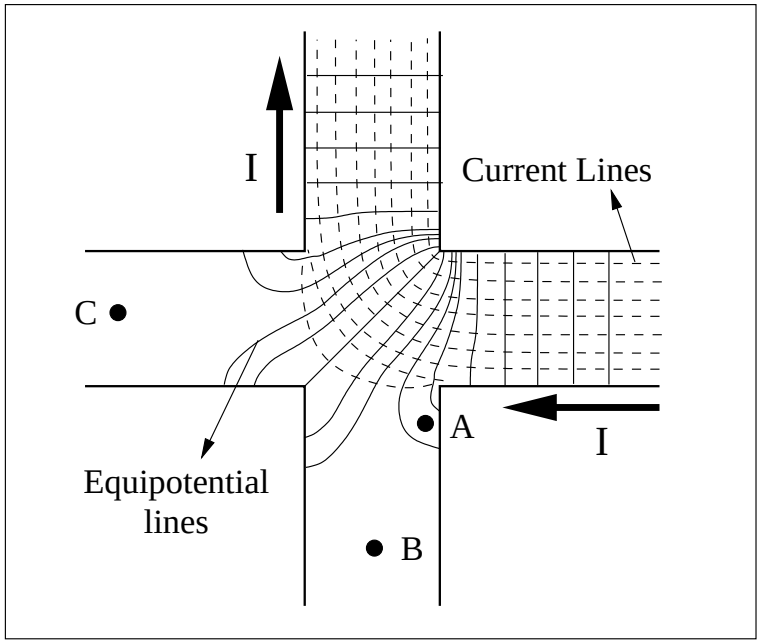

Figure 5.18: Two dimensional schematic of the current lines and equipotential lines in a cross geometry when the current flows between adjacent arms.

with contact resistances of about 76 Ω gave null results.

As a side comment, it is important to note that measurements of the contact resistance can contain a component from the mentioned electrostatic effect. To illustrate this point, measurements of the contact resistance in Py-Cu samples were done by injecting current as shown in Fig. 5.18 and measuring the voltage difference between points C and B. The measurements gave negative values for the contact resistance, that were on the order of -100 mΩ. The contact resistance must be positive and in the case of transparent samples it must be smaller than hundreds of mΩ. This apparent contradiction is resolved by looking at the equipotential lines between points C and B in Fig. 5.18, and realizing that the equipotential line closest to C is at a lower voltage than that closest to B, so indeed a negative potential drop

exists apart from any real contact potential. Therefore electrostatic effects can be of importance for some of the measurements, but their contribution to the nonlocal resistance is negligible.

5.2.8 Current leakage

The four types of current leakage that can occur in the experiment are the following. First, in the probe wiring; second, through the surface of the samples or through the insulating SiO_2 layer to the doped Si; third, capacitive leakage due to wiring capacitances and the input capacitance of the lock-in amplifiers; and fourth, resistive leakage due to the finite input impedance of the lock-in amplifiers. Current leakage in the probe wiring, the sample holder, and the sample, were checked with a high input impedance multi-meter [11]. All of the measured resistances were larger than 1 GΩ. The stray capacitance of the wiring (wire to wire and wire to ground) at the operating frequency is close to 100 MΩ, so its contribution is as large as that from the leakage through the input impedance of the lock-in amplifiers. A circuit model of the device and probe is needed in order to understand the effect of these current leakages in the measured signal. This is presented in Fig. 5.19(b), together with a sample schematic [Fig. 5.19(a)]. The numbered capacitances (120 pF and 160 pF) are stray capacitances from the wiring, while the ones labelled A and B (30 pF) are the input capacitances of the lock-in amplifier. For example C_{1-3} is the capacitance between lead 1 and lead 3, while C_A is the input capacitance of the A channel of the lock-in amplifier. The resistors labelled RC_1 and RC_2 represent the contact resistances

[11] HP digital multi-meter.

of the F_1-N and F_2-N interfaces, R1-2 represents the resistance of the copper line between injector and detector, and RA and RB are the input impedances of the two channels of the lock-in amplifier. The rest of the numbered resistors represent the resistance from either the injector interface or the detector interface to the BNC connectors in the probe, through each of the different leads numbered in Fig. 5.19(a). For example R_3 is the resistance from the F_1-N interface to BNC 3, which is connected to lead 3, while R_6 is the resistance from the F_2-N interface to BNC 6, connected to lead 6. The two arrows show the placement of control leads used to measure the difference in voltage between the A and B input channels of the lock-in amplifier. The result of PSPICE simulations on this and similar circuits showed that, depending on the particular values of the resistances and for bias currents of about 20 μA, there was an in phase component of the nonlocal resistance due to leakage that was smaller than 15 nV and that could be either positive or negative, together with an out of phase component that could be larger (reaching 100 nV for some of the samples) and that could also have positive or negative sign. The out of phase component is of no consequence for the measurements since the lock-in only detects signals that are in phase with the drive. The small value of the calculated in phase signal can explain the small shifts of the nonlocal resistance that were sometimes observed at low temperatures (for example in Fig. 5.6), but it cannot account for the large symmetric component that appeared at higher temperatures or for its temperature dependence.

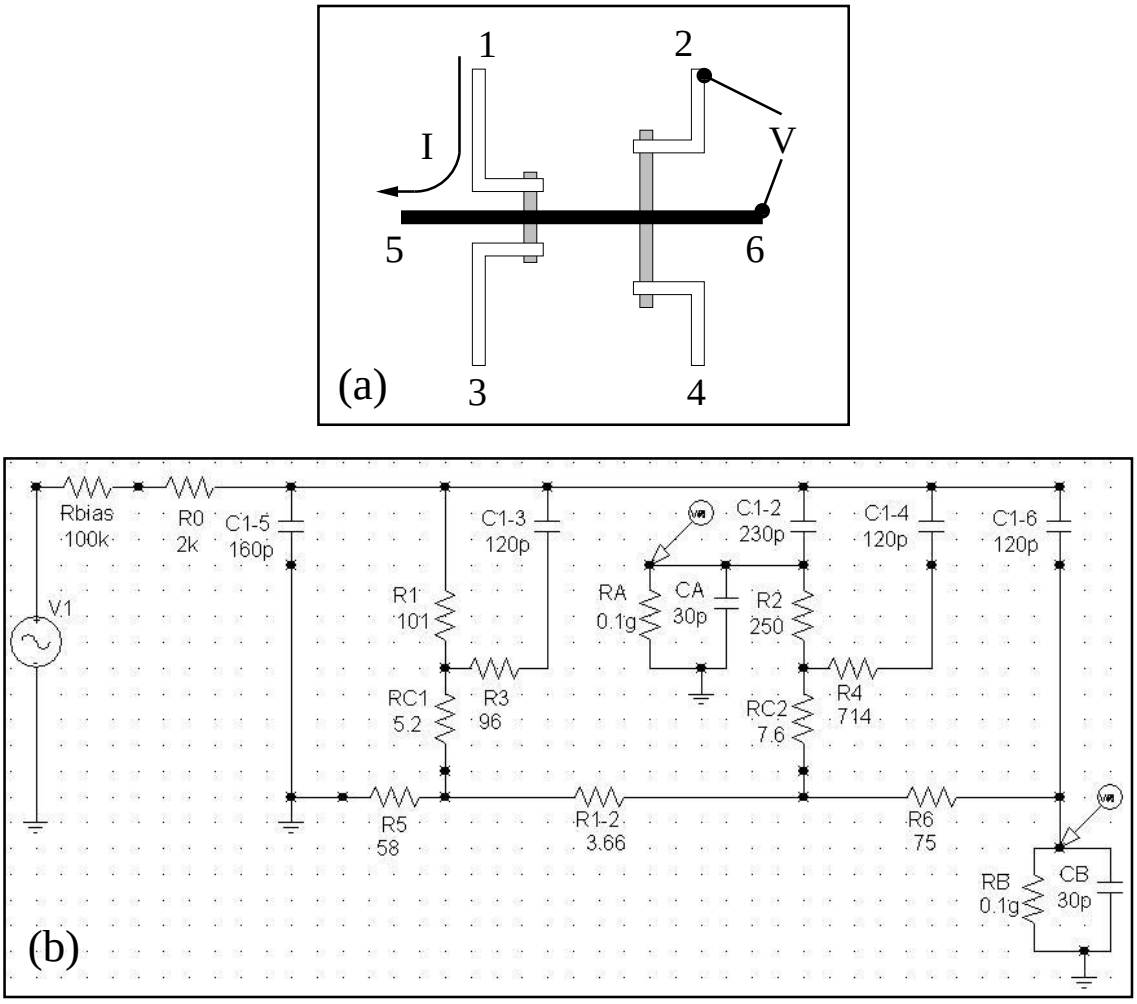

Figure 5.19: (a) Schematic of the sample with numbered leads. (b) Circuit model schematic of sample plus wiring. The numbers in the labels of the components are those illustrated in (a). Resistances are in units of Ohms and capacitances in units of Farads, with the additional modifiers pico (p), kilo (k), and giga (g).

5.2.9 Lock-in tests

To check the operation of the lock-in amplifiers that were used in the experiments, three different tests were performed. The first one was to check the stability of the phasing, the second was to check the DC rejection, and the third was to check the second harmonic rejection. The first check was performed by phasing the lock-in with a 100 mV bias at low sensitivity as described in the operation manual of the PAR-124 Lock-in Amplifier, and then measuring the in phase and out of phase voltage components at a small resistor at a high sensitivity (100 nV). The appearance of an out of phase signal would mean incorrect phasing in the high sensitivity settings. However, for an in phase signal of 108 nV, the out of phase component was 1.9 nV, within the noise of the measurements, so no dephasing at high sensitivities was detected. For the second test, DC rejection, DC voltages between -100 mV and 100 mV were applied directly to the inputs of channels A and B of the lock-in, and the in phase component was monitored at a sensitivity of 100 nV. The measured voltages were between -2.6 nV and 2 nV, also within the noise of the measurements. Finally, the second harmonic rejection was tested by injecting a voltage signal at twice the fundamental into either channel A or B and monitoring the output of the lock-in. For voltages larger than 10 μV the lock-in overloaded, but for voltages as high as 9 μV the output was less than 1 nV. Therefore all the tests show correct operation of the lock-in.

Chapter 6

Spin injection and magnetic force microscopy detection I: Introduction

The previous section reported on transport measurements of the spin relaxation length and the spin current polarization in Py-Cu and Co-Cu spin valves. The interpretation of these measurements required fitting the data to a model based on the diffusion equation, which assumed different electrochemical potentials for each spin channel, and also a particular set of boundary conditions at the F-N interfaces. Since no microscopic understanding of interfacial spin transport is available, an alternative experiment which can directly give the spin relaxation length and the spin current polarization without requiring any spin transport model is useful. This and the following chapters will describe such an experiment, based on the direct magnetic force microscope (MFM) detection of the magnetic field produced by the excess magnetization in a Cu wire. This excess magnetization is generated by the injection of spin-polarized electrons from a neighboring ferromagnetic contact.

In this chapter the operation and simplest theoretical model of a scanning probe microscope (SPM) such as a magnetic force microscope (MFM), electric force microscope (EFM), or atomic force microscope (AFM), will be shown. The procedure for measuring a non-equilibrium spin polarization in a nonmagnetic metal

using MFM will be discussed, together with some of the improvements that were made to the cantilever and the operation mode in order to enhance the resolution and sensitivity. The following chapter will discuss the actual experimental setup and the results.

6.1 Scanning probe microscope operation and model

A schematic of a magnetic force microscope (or equivalently an atomic or electric force microscope) is shown in Fig. 6.1. By means of a drive piezoelectric, a cantilever with a magnetized tip[1] is made to oscillate in the z direction at its resonant frequency $\omega_0 = \sqrt{k/m^*}$ where k is the cantilever spring constant and m^* the effective cantilever mass[2]. A semiconductor laser is used to shine light on the back surface of the cantilever. By monitoring the difference in light intensity between the upper and lower sections of a four segment photodetector, normalized by the total light intensity, the deflection of the reflected beam and therefore of the cantilever can be found. The deflection information goes to a controller and computer which send a feedback signal to both the Z drive and Z piezoelectrics to control the cantilever vibration and to adjust the cantilever's vertical position. The sample is mounted on X, Y, and Z piezoelectrics which control the fine motion from nanometers to tens of microns. Coarse movement along any of the three axis can be made using a mechanical stage.

The MFM is operated in the tapping mode, in which the cantilever encounters

[1]The magnetic metal covered tip is necessary only for MFM. For EFM any metal can be used, but nonmagnetic ones are preferred, and for AFM no metallic coating of the tip is necessary.

[2]Which is equal to one fourth of the mass of the cantilever.

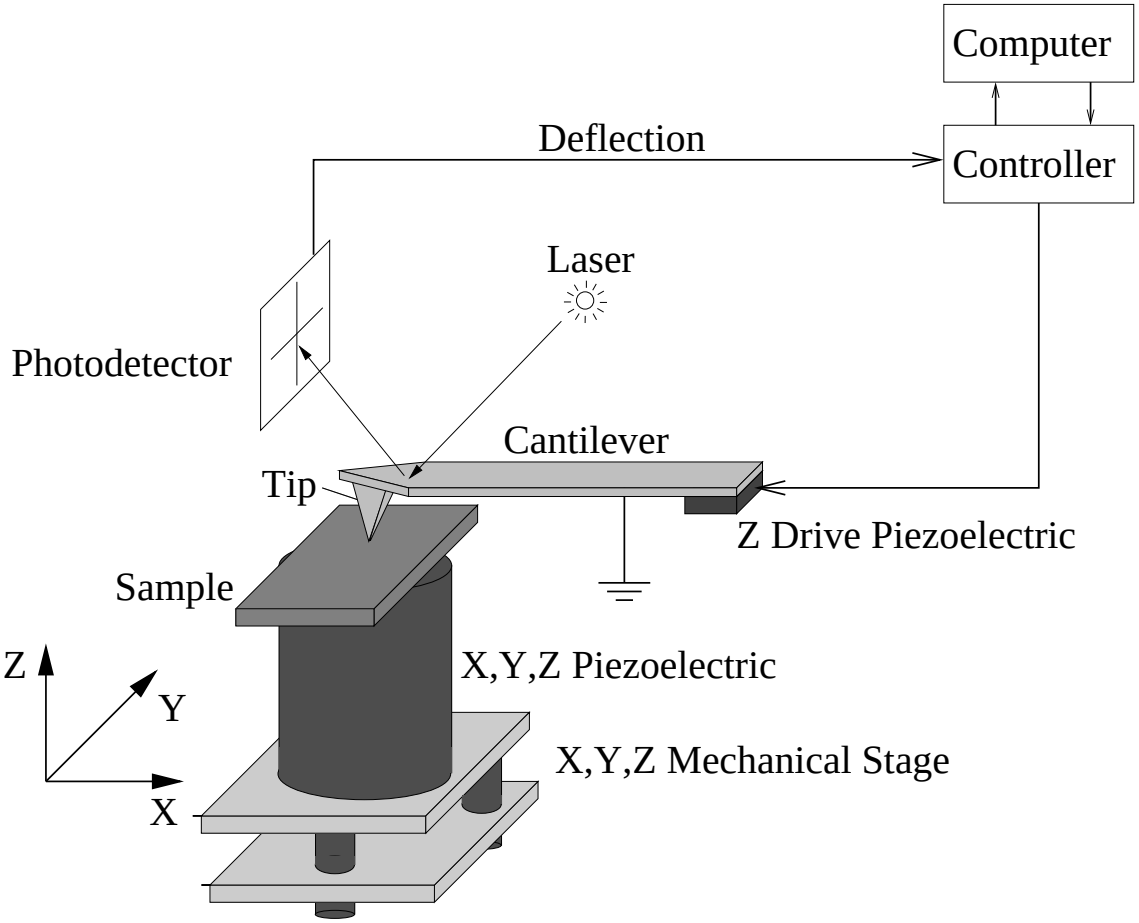

Figure 6.1: Schematic of a scanning probe microscope (MFM, EFM, or AFM) with a fixed vibrating cantilever and movable sample stage.

the short range repulsive part of the Van del Waals interaction with the sample. This decreases both tip and sample damage by avoiding shear forces. To get topography information of the sample the Z piezoelectric is used to move the stage up until the cantilever oscillation amplitude changes, due to Van del Waals repulsion, to a specified setpoint. The cantilever is then said to be engaged to the sample. The X,Y piezoelectrics are then used to laterally move the sample. Any change in the topography of the sample changes the force between the sample and the cantilever, changing the deflection. The controller senses this change and modifies the vertical

position of the cantilever by changing the voltage at the Z piezoelectric to keep the deflection at the specified setpoint. This feedback system avoids crashing the sample into the tip, and by monitoring the feedback signal (i.e. the voltage control sent to the Z piezoelectric) a calibrated image of the topography of the sample can be generated since the voltage-displacement relation of the X,Y,Z piezoelectrics is known.

For the Digital Instruments Multi-Mode SPM used in the experiment, topography and magnetic force detection are interleaved, that is, line scans of topography and line scans of magnetic force detection are taken one after the other. First, trace (increasing X) and retrace (decreasing X) topography lines are acquired. The cantilever is then raised to an average baseline at a specified height above the average height of the sample to do the magnetic force detection. During magnetic force detection the feedback loop is disconnected and the change in the phase of the oscillating cantilever is monitored by the computer. Again trace and retrace lines are acquired, the cantilever is brought down to the original Z position, and the system is ready to acquire the next topography line.

The simplest model for the operation of an MFM (EFM or AFM) treats the cantilever as a forced, damped, harmonic oscillator with resonant frequency ω_0 and quality factor Q. Therefore the equation of motion for the vertical position of the tip Z is given by

$$\frac{1}{\omega_0^2}\ddot{Z} + \frac{1}{Q\omega_0}\dot{Z} + Z = \frac{1}{k}\left[F_0 \exp(i\omega_0 t) + F|_{Z_0} + \left.\frac{\partial F}{\partial Z}\right|_{Z_0}(Z - Z_0)\right], \tag{6.1}$$

where F_0 is the driving force from the Z drive piezoelectric, $F = F(x, y, z)$ is an external time independent force acting on the tip of the cantilever (either from magnetic, electric, or Van der Waals interaction with the sample). This force is assumed to be much smaller than the drive so that it can be expanded in a first order Taylor series about the equilibrium position of the tip Z_0 in the absence of any force. The solution to equation (6.1) is given by

$$Z(t) = \frac{1}{k}\left[F - \frac{\partial F}{\partial Z}Z_0\right]_{Z_0} + \frac{QF_0}{k}\left[i - \frac{Q}{k}\left.\frac{\partial F}{\partial Z}\right|_{Z_0}\right]^{-1}\exp(i\omega_0 t). \tag{6.2}$$

The first term on the right hand side only introduces a shift in the equilibrium position of the tip and is time independent. Phase sensitive detection averages this term to zero. The second one, however, has harmonic dependence with phase given by

$$\phi = -\frac{\pi}{2} - \arctan\left[\frac{Q}{k}\frac{\partial F}{\partial Z}\right]_{Z_0}, \tag{6.3}$$

which is the actual measured quantity in MFM. Since the force is small compared with the drive, the phase shift introduced by the external force is small so it can be approximated by

$$\triangle\phi = -\frac{Q}{k}\left.\frac{\partial F}{\partial Z}\right|_{Z_0}. \tag{6.4}$$

6.2 Spin injection and MFM detection

It was shown in chapter 3 that when a current is driven from a ferromagnetic to a nonmagnetic metal the current is spin-polarized and the spin, or equivalently the magnetization, decreases exponentially away from the point of injection with a characteristic length given by the spin relaxation λ of the electrons in the nonmagnetic material. Detection of such a non-equilibrium magnetization can in principle be done by taking advantage of the high resolution and high sensitivity of MFM. The advantage of MFM detection is that the magnetization of the spin-polarized electrons is detected by directly measuring its effect on a magnetized oscillating cantilever, so no transport model is necessary to interpret the results. Additionally, the length dependence of the magnetization can be studied for a fixed injector, avoiding the contact reproducibility problems found during the length dependence measurements of the spin signal in the previous chapter. Transport measurements of the length dependence of the spin related resistance required using different contacts for injection and detection, each of which could have different interfacial spin current polarization P, producing systematic errors in the measurement of λ. This is solved with MFM detection since in MFM measurements a fixed magnetic electrode is used for spin injection, and detection is done by scanning at different separations from the injection point. Finally, the spin current polarization P of the injector can be found independently, which was not possible with transport measurements where only the product P_1P_2 could be found.

A very important issue that has to be addressed is the back-action of the stray

magnetic field of the cantilever on the electrons. Measurements [68] have shown that the stray field from a typical cantilever at a distance of 250nm from the tip is about 4mT. It was shown in chapter 5 that in our typical devices electrons precess by an average angle of $\pi/2$ in a distance of the order of 900nm when a field of 300mT is applied. Therefore the stray field produced by the cantilever is too small to produce any significant electron spin dephasing in our Cu wires, so that the back-action of the cantilever can be ignored.

A schematic of the configuration for spin injection and MFM detection is shown in Fig. 6.2. An oscillating cantilever with a magnetized tip (shown in light gray) scans the surface of the sample in the x-y plane. Current is driven along the Cu wire (shown in white) between the top (T) and bottom (B) leads. Close to $y = 0$ a section of the Cu wire has been replaced by Py (shown in dark gray), so that all the

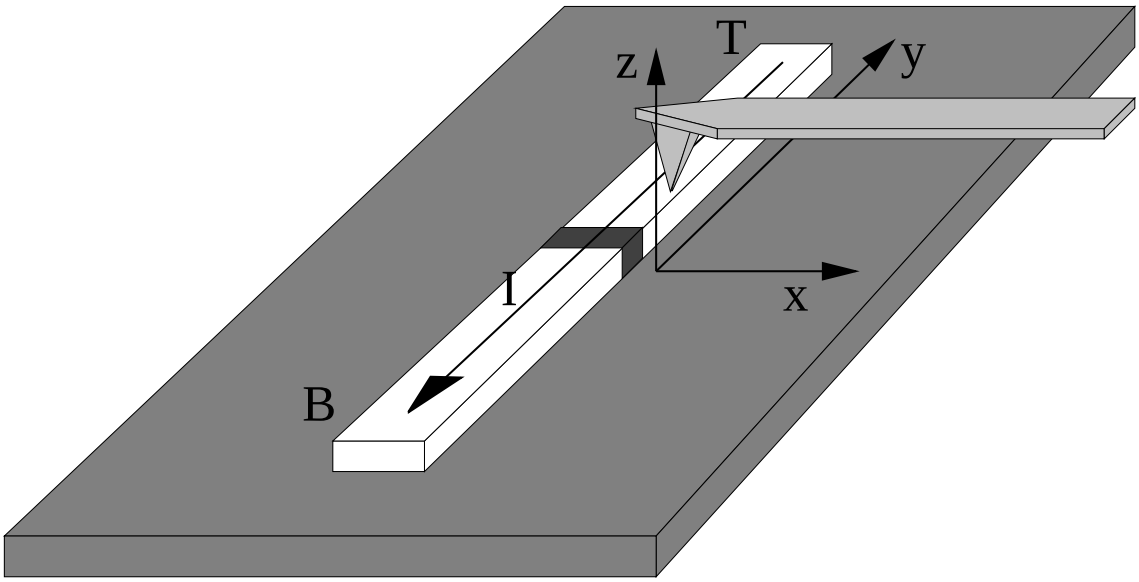

Figure 6.2: Schematic for spin injection and MFM detection. A current driven along the copper wire (white) is forced to enter a ferromagnetic section (black)of the wire, as a cantilever with a magnetized tip scans close to the ferromagnetic-nonmagnetic metal interface.

current goes from Cu to Py and back again to Cu. If the length of the wire section that was replaced is longer than the spin relaxation length of electrons in Py (less than ten nanometers according to Dubois et. al. [59] and Steenwyk et. al [61]), spin transport across one of the Cu-Py interfaces does not depend on the spin transport across the other Cu-Py interface. Assuming that the magnetic material has its magnetization in-plane and pointing in the x direction (this direction will be called spin up), electrons that enter the Py travelling from B to T have mostly spin up since the density of states in Py for spin up is larger than for spin down. Therefore an excess population of electrons with spin down is left in the bottom Cu section close to the interface. The injected electrons lose their spin information within a distance λ_F, relaxing to the average spin polarization value in Py. Meanwhile on the top Py-Cu interface mostly electrons with spin up are injected into Cu, so an excess population of electrons with spin up will appear on the top Cu section close to the magnetic contact. The electron density n_σ for spin σ can be easily calculated from the electrochemical potential μ_σ by using the free electron model. In the limit of small deviations from equilibrium, $\delta\mu_\sigma \ll E_F$ where E_F is the Fermi energy,

$$n_\sigma(y) = n_\sigma^0 + \frac{m^*}{\hbar^2\pi^2} k_{F\sigma}\delta\mu_\sigma(y), \tag{6.5}$$

where n_σ^0 is the equilibrium electron density, m^* the effective mass, and $k_{F\sigma}$ is the Fermi wave vector. Furthermore, since the excess magnetization is given by $\delta M = \mu_B(n_\uparrow - n_\downarrow)$ where μ_B is the Bohr magneton, it is possible to write in general

$$\delta M(y) = \frac{m^* \mu_B}{\hbar^2 \pi^2}(k_{F\uparrow}\delta\mu_\uparrow(y) - k_{F\downarrow}\delta\mu_\downarrow(y)), \tag{6.6}$$

or for the case of nonmagnetic metals where $\delta\mu_\uparrow = -\delta\mu_\downarrow = \delta\mu$ and $k_{F\uparrow} = k_{F\downarrow} = k_F$,

$$\delta M(y) = \frac{2m^* \mu_B}{\hbar^2 \pi^2} k_F \delta\mu(y). \tag{6.7}$$

By solving the equations for the electrochemical potential presented in chapter 3 for each F-N interface, and using equations (6.5) to (6.7), the excess magnetization as a function of y can be calculated. For transparent F-N interfaces the calculated excess magnetization (in the x direction) for a 1.2 μm wide, 50 nm thick wire carrying a current of 9.1 mA is shown in Fig. 6.3 for realistic values of the resistivity and spin relaxation lengths of both metals. The qualitative features described previously such as the extra spin up concentration for $y > 0$, extra spin down concentration for $y < 0$, and independence of spin transport at both interfaces due to the fast spin relaxation in the ferromagnet, are evident.

Detection of the excess magnetization is done by the oscillating magnetized cantilever shown in Fig. 6.2. Since the cantilever has a tip magnetized in the z direction, the interaction between the tip and sample magnetizations can be described by the potential energy [69]

$$U = -\int \vec{M} \cdot \vec{B_{\delta M}} dV, \tag{6.8}$$

where the term on the right hand side represents the energy stored in the magnetic moment of the cantilever due to the stray field produced by the sample magnetiza-

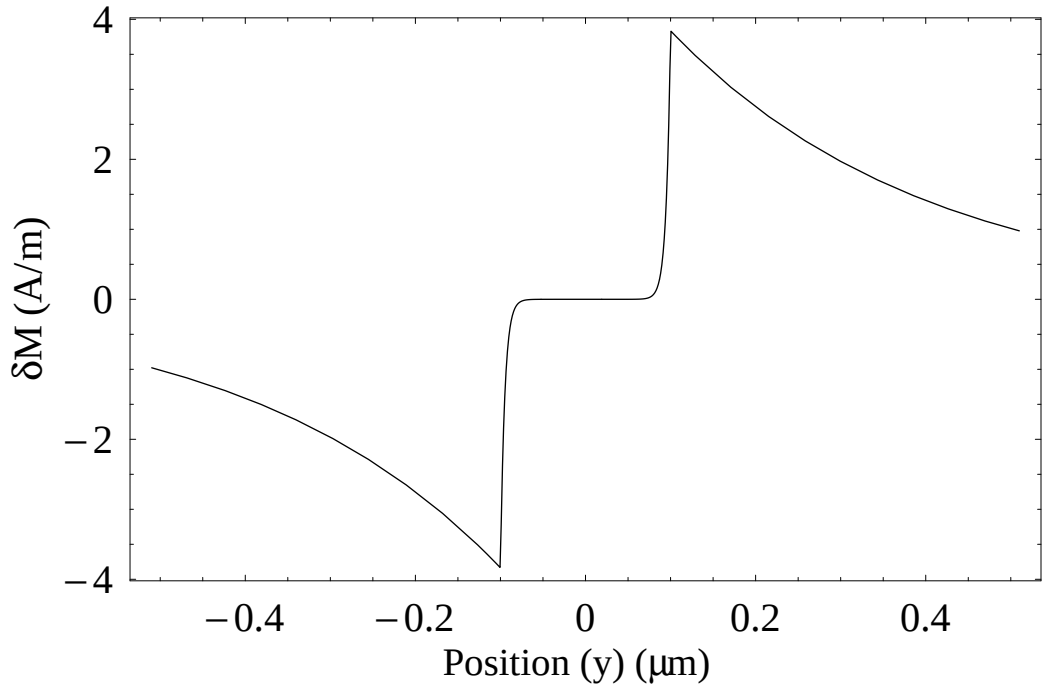

Figure 6.3: Calculated excess magnetization δM (in the x direction) as a function of y for a 1.2 μm wide, 50 nm thick wire carrying a current of 9.1 mA. Realistic values of the resistivity and spin relaxation lengths of both metals have been assumed for the calculation.

tion. Letting $(\hat{x}', \hat{y}', \hat{z}')$ be a reference frame mounted on the apex of the cantilever tip, with each primed axis parallel to the corresponding unprimed axis of the fixed reference frame on the sample (shown in Fig. 6.2), equation (6.8) can be written more precisely as

$$U(\vec{r}) = -\int \vec{M}(\vec{r'}) \cdot \vec{B_{\delta M}}(\vec{r} + \vec{r'}) d^3r', \tag{6.9}$$

where $\vec{B_{\delta M}}(\vec{r})$ is the magnetic field produced by the excess magnetization of the device at a point $\vec{r}$ in the unprimed reference frame, while $\vec{M}(\vec{r'})$ is the magnetization of the cantilever tip at point $\vec{r'}$ in the primed reference frame. The energy is a

function of the relative position between the cantilever tip and the device. Since the device is assumed to be fixed, the force on the cantilever produced by the magnetic coupling with the sample is simply the negative of the gradient of the potential energy. Furthermore, since the cantilever is extremely rigid in both x and y directions its only degree of freedom is in the z direction so the magnetic driving force on the cantilever is

$$F(\vec{r}) = -\frac{\partial U(x,y,z)}{\partial z}. \tag{6.10}$$

Replacing the expression for U from equation (6.9) into equation (6.10) gives

$$F(\vec{r}) = \int \vec{M}(\vec{r'}) \cdot \frac{\partial \vec{B}_{\delta M}(\vec{r}+\vec{r'})}{\partial z} d^3r', \tag{6.11}$$

which is the convolution of the magnetization of the cantilever tip and the z derivative of the field produced by the excess magnetization. Therefore the magnetization of the cantilever tip can be regarded as a convolution factor that can be either calculated numerically or found directly by measuring a device with a known magnetic field profile. The field produced by the excess magnetization in the spin injection device can be calculated using Green's functions as

$$\vec{B}_{\delta M}(\vec{r}) = \frac{\mu_0}{4\pi} \nabla\nabla \cdot \int \frac{\delta \vec{M}(\vec{r'})}{|\vec{r}-\vec{r'}|} d^3r', \tag{6.12}$$

for any function $\delta\vec{M}$, not necessarily continuous. If this expression is replaced into equation (6.11), and the ∇ operators are applied, the result is

$$F(\vec{r}) = -\frac{\mu_0}{4\pi}\frac{\partial}{\partial z}\int\int d^3r'd^3r'' \quad \left[-\frac{3\delta\vec{M}(\vec{r'})\cdot(\vec{r}+\vec{r'}-\vec{r''})\vec{M}(\vec{r''})\cdot(\vec{r}+\vec{r'}-\vec{r''})}{|\vec{r}+\vec{r'}-\vec{r''}|^5} + \frac{\delta\vec{M}(\vec{r'})\cdot\vec{M}(\vec{r''})}{|\vec{r}+\vec{r'}-\vec{r''}|^3}\right], \tag{6.13}$$

which has the same structure as the force between two dipoles. This last equation is specially useful for estimating the magnitude of the force to be measured, while equation (6.11) is useful for finding the convolution factor for a particular cantilever. The magnetic field produced by the excess magnetization shown in Fig. 6.3 for a wire of specified dimensions can be calculated directly by using equation (6.12) if the magnetization is assumed to be uniform along the cross section of the wire. For a 1.2 μm wide, 51 nm thick wire, a separation of 400 nm between the upper and lower Cu sections, and a current of 9.1 mA (see Fig. 6.3) the calculated field in the z direction at z=200 nm as a function of x and y is shown in Fig. 6.4(a). Only the z component of the field is relevant since the magnetization of the cantilever tip is constrained to be in the vertical direction. Two diagonally opposed peaks and holes are visible from the figure showing that the field in the top Cu wire is exactly opposite as that in the lower Cu wire since they come from accumulation of different spins. The maximum of the plotted field is about 0.57 μT. However, from equations (6.2) and (6.11) it is clear that in the normal MFM operation mode the cantilever is sensitive to $\partial^2 B_z/\partial z^2$. Furthermore, it will be shown later in this chapter that in the resonant MFM operation mode the cantilever is sensitive to $\partial B_z/\partial z$, therefore information on these quantities is relevant. Figures 6.4 (b) and (c) show the first

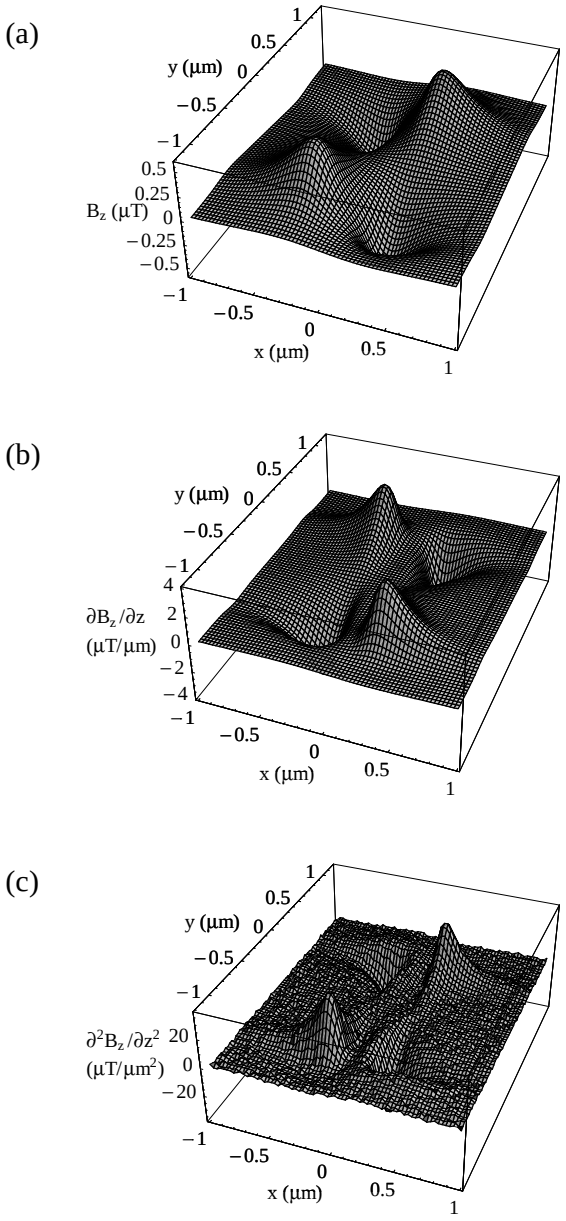

Figure 6.4: (a) Magnetic field in the z direction as a function of x and y at a height of 200 nm above a 1.2 μm wide, 51 nm thick wire carrying a current of 9 mA, due to the excess magnetization shown in Fig. 6.3. (b) First and (c) second derivatives of B_z with respect to z.

and second z derivatives of the field in the z direction, with maximum values 4 μT/μm and 37 μT/μm^2 respectively. This information will be useful for estimating the magnitude of the force produced by the excess magnetization on the cantilever.

6.3 Increasing the resolution of the cantilever

Commercially available MFM cantilevers have a magnetic coating on all of the tip and cantilever. This means that slowly decaying magnetic signals affect the cantilever response over a large scanning area. This limits the resolution since magnetic signals coming from very distinct parts of the sample are being averaged. In other words the convolution factor is too broad so detecting small features is impossible. In order to enhance the resolution of the cantilevers, a magnetic coating has been applied to nonmagnetic cantilevers on a small region near the apex of the tip. In this section I will describe the procedure used to fabricate this high resolution tips and will compare them with commercially available ones.

The starting point is an etched silicon probe from Veeco (model FESP), where the cantilever and tip have already been defined. A mask, e-beam lithography, lift-off procedure similar to the one described in chapter 4 is used, so only the new variations in the fabrication will be discussed in detail. The probe is mounted on a holder so that the inner part of the tip faces up. PMMA is used to cover the whole probe except for the cantilever and tip. Then, while heating the probe to a temperature of 100 ^{o} C, one drop of 150k PMMA is used to cover the tip and cantilever for 15 seconds. A thin layer of PMMA sticks to the tip and cantilever, and the rest of the PMMA drop is spun off at 3000 rpm. The probe is then baked

at 170 ^{o} C for an hour and the procedure is repeated with one more layer of 150k PMMA and then with one layer of 360k PMMA. A final bake of two hours at 170 ^{o} C is done to completely remove any remaining PMMA solvent. A low current electron beam rasters the bottom part of the probe to find the apex of the tip. This has to be done in a time shorter than the exposure time of the PMMA, or else the exposed areas will be developed. Once the apex of the tip has been aligned in the center of the field scale, the e-beam is used to expose a small region around the apex. The probe is then developed and a film of cobalt between 50 nm and 150 nm is thermally evaporated, followed by a thin protective chromium coverage. After lift-off, only a small area around the apex of the tip has Co covering. Three different tips with varying Co area are shown in Fig. 6.5. Even though by design the tips shown in (a) and (b) were supposed to have the same magnetic covering, there is some variation since the e-beam dose can change and since the lift-off is difficult.

In order to see the improvement of the resolution of the cantilever, the magnetic field produced by a straight 4.8 μm wide line carrying a current of 19 mA was measured in the normal MFM (phase) mode with both a normal and a high resolution probe at a scan height of 240 nm and scan rate of 0.1 Hz. The result is shown in Fig. 6.6. The dashed black line shows the expected response for a point probe[3], while the solid black (gray) line shows the response for a high resolution (normal) probe. The left (right) vertical scale gives the signal measured by the photodetector for the high resolution (normal probe). The units of the vertical axes

[3]Normalized to match the features of the other two curves.

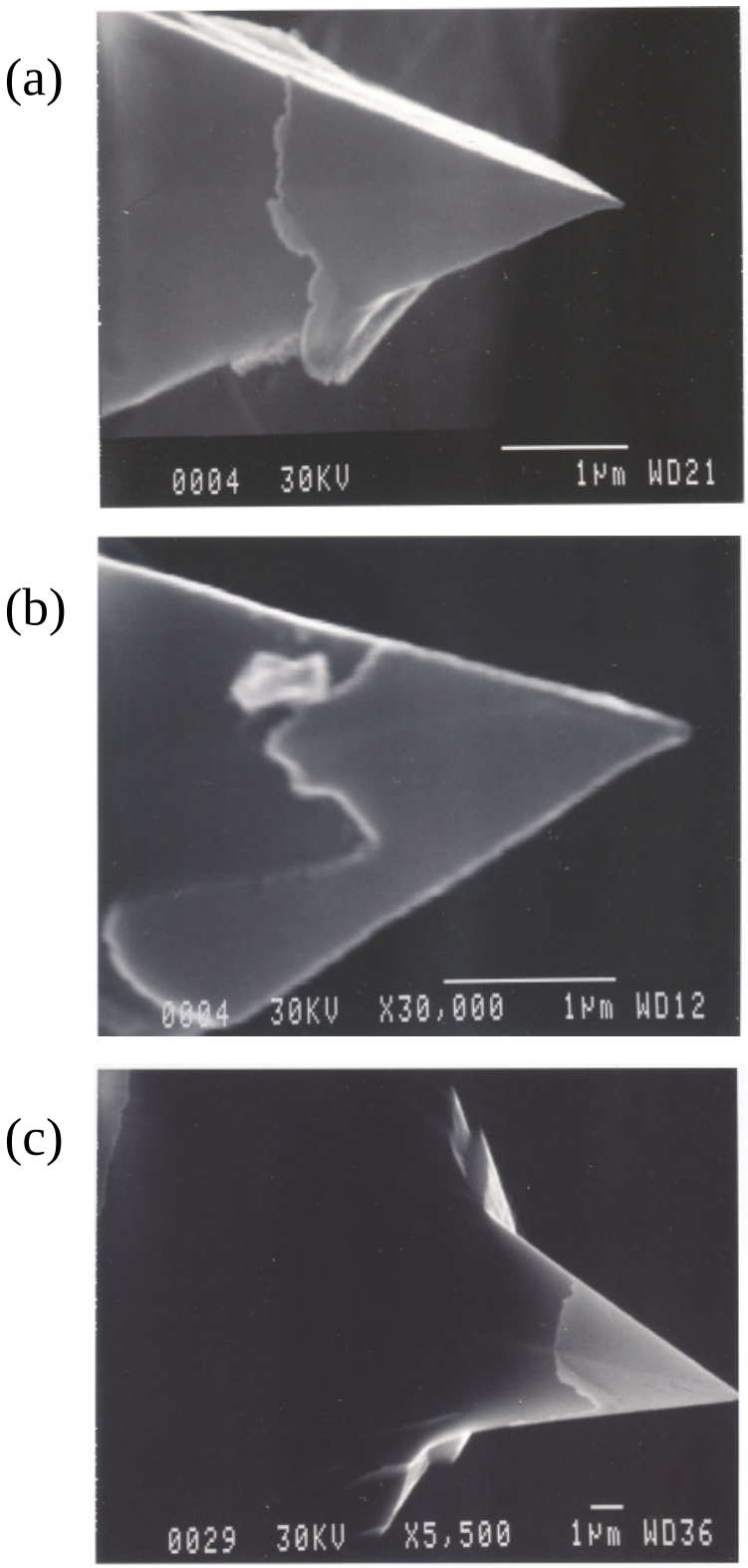

Figure 6.5: High resolution tips with small cobalt covering near the apex.

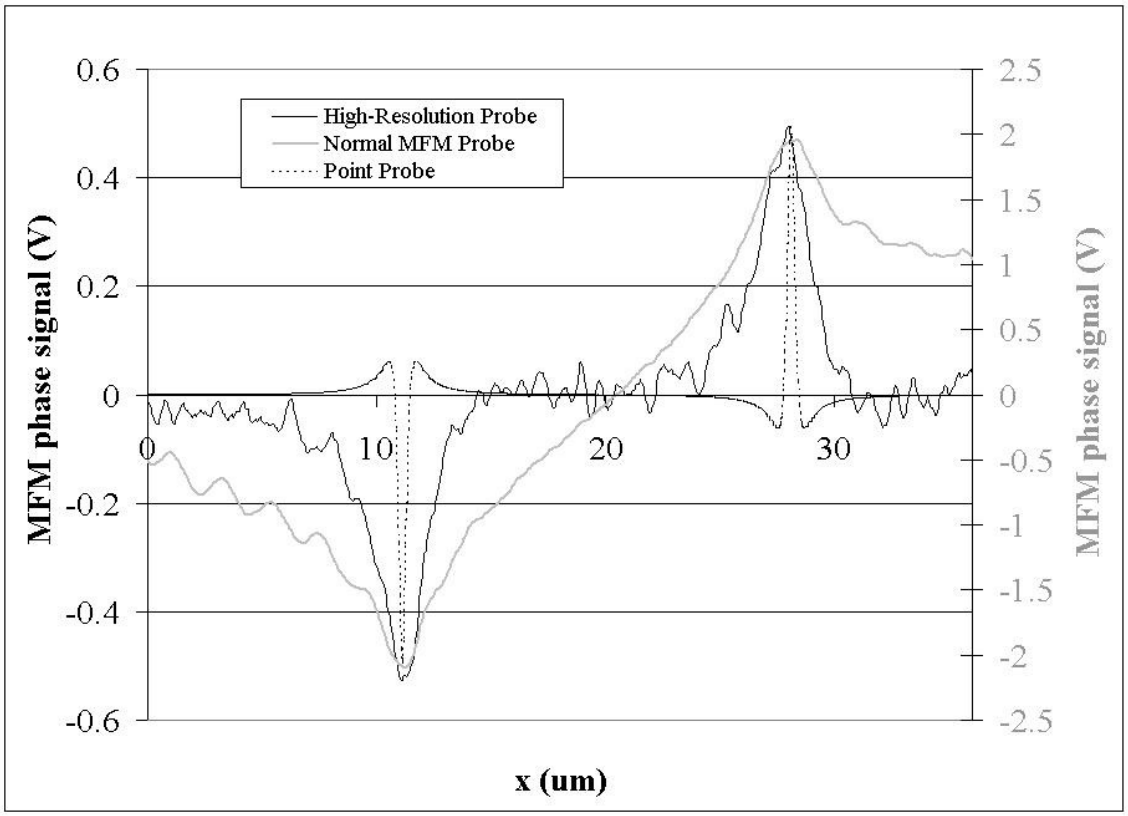

Figure 6.6: Comparison of the response of the normal MFM and high resolution probes to the field produced by a straight current carrying line. The high resolution (normal) probe response is shown with a solid black (gray) line, while the ideal response to a point probe is shown with a dashed black line.

are Volts, which can be converted to real units of phase (radians) after calibration (not necessary for this comparison). The high resolution cantilever has a response which is more than 2.5 times narrower than the normal cantilever, and the signal clearly goes to zero within the scanning range, as opposed to the signal from the normal cantilever which decays very slowly and on the right hand side has only decreased by 50% from the maximum value. However, the increase in resolution is at the expense of decreased sensitivity, as illustrated by the difference in the scale of the response for each probe. The decrease in sensitivity of the high resolution

probe can be compensated by depositing thicker films of cobalt, but this makes the lift-off process more difficult.

6.4 Resonant MFM operation

The normal mode of MFM operation was described in the first section of this chapter. It was shown that the detected signal is the phase shift of the cantilever oscillatory motion given by equation (6.4), which is proportional to the derivative of the force. Since the magnetic force is proportional to the derivative of the field, the cantilever gives information on $\partial^2 B_z/\partial z^2$. A variation of MFM detection can be implemented for systems in which the magnetic field produced by the sample at a fixed position is time dependent. In particular, for systems that produce a magnetic field that oscillates at the natural frequency of the cantilever ω_0 in a "resonant" way. Examples of such systems are a wire carrying an oscillating current at frequency ω_0, or a rotating magnetic moment with frequency ω_0. In this case the amplitude of oscillation gives information on the force, that is, on the first derivative of the field, $\partial B_z/\partial z$. In this section I will present the model for resonant MFM operation, and will compare measurement results using both phase and resonant methods.

Using the same model described at the beginning of this chapter which lead to equation (6.1), that is, treating the tip as a forced, damped, harmonic oscillator, it is possible to write the equation of motion for the tip as

$$\frac{1}{\omega_0^2}\ddot{Z} + \frac{1}{Q\omega_0}\dot{Z} + Z = \frac{F_0}{k}\exp(i\omega_0 t) + \frac{1}{k}\left[F|_{Z_0} + \left.\frac{\partial F}{\partial Z}\right|_{Z_0}(Z - Z_0)\right]\exp(i\omega t), \quad (6.14)$$

where F_0 is the driving force from the Z drive piezoelectric and $F = F(x, y, z)$ is the external force acting on the tip of the cantilever. This force is assumed to be much smaller than the drive so that it can be expanded in a first order Taylor series about the equilibrium position of the tip Z_0 in the absence of any force. The external force is assumed to have an explicit harmonic time dependence[4] with frequency ω, as represented by the term $\exp(i\omega t)$ in equation (6.14). The general solutions to first order at frequencies ω and ω_0 are given by

$$Z_\omega(t) = \tfrac{F|_{Z_0}}{k}\beta(\omega)\exp(\imath\omega t) \tag{6.15}$$

$$Z_{\omega_0}(t) = \tfrac{\imath Q}{k}\exp(\imath\omega_0 t), \tag{6.16}$$

where $\beta(\omega)$ is the enhancement factor due to the nonlinear frequency response of the cantilever, given by

$$\beta(\omega) = \left[1 - \frac{\omega^2}{\omega_0^2} - \imath\frac{\omega}{Q\omega_0}\right]^{-1}. \tag{6.17}$$

The cantilever response at the frequency ω is therefore proportional to the force. For a magnetic interaction between the sample and tip, the force is proportional to the derivative of the field, hence the amplitude of oscillation of the cantilever depends linearly on $\partial B_Z/\partial Z$. If $\omega \ll \omega_0$, $\beta \approx 1$ so the amplitude of the cantilever oscillations is equal to F/k. If, on the other hand $\omega \gg \omega_0$, $\beta \approx -\omega_0^2/\omega^2$ so the amplitude response of the tip is strongly attenuated. However, if $\omega = \omega_0$, $\beta = \imath Q$

[4]Which can be caused by an oscillating current or by a rotating magnetic moment, both of which produce an explicitly time dependent magnetic field.

so the amplitude response is enhanced by a factor of $Q \gg 1$. This means that by oscillating the external force at the resonant frequency, the amplitude of oscillation of the cantilever is a factor of Q larger than the amplitude when the force is time independent.

In order to test the resonant method, the signal from a straight 4.8 μm wide line carrying a current of 106 μA was measured at a scan height of 400 nm and with a scan rate of 0.1 Hz, using both the normal (phase) and resonant methods. The result is shown in Fig. 6.7, with a different scale for each of the traces. Since the resonant method measures the change in amplitude, proportional to $\partial B_z/\partial z$, while the normal method measures the change in phase, proportional to $\partial^2 B_z/\partial z^2$, the trace obtained using the resonant method has to be transformed to give directly the second derivative of the field with respect to z. This can be done by using Fourier transforms as shown in the Appendix [see equation (A.37)]. The scale on each axis has been set in such a way that the maximum and minimum of each curve overlap. The ratio between the size of the peaks and the average fluctuations (noise) is more than two times larger for the resonant method than for the phase method. This additional sensitivity of the resonant method is not, however, a general property, but depends on the relative magnitude of the first and second derivatives of the field, and on the relative size of the thermal fluctuations[5] and the vibration amplitude of the cantilever. The latter determines the effect of the thermal noise in the phase, so for larger cantilever oscillation amplitudes, the displacements caused by thermal

[5]Which are the main source of noise. [70]

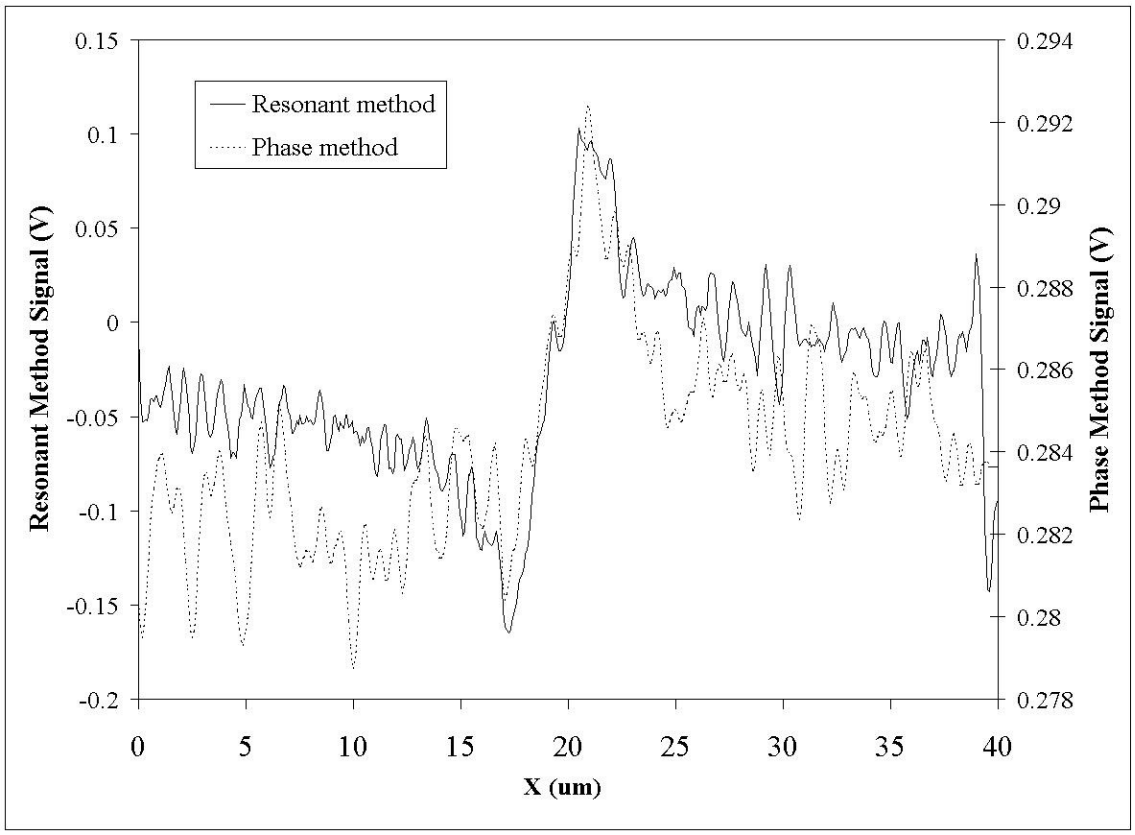

Figure 6.7: Comparison of the response of the normal MFM phase method and the resonant method to the field produced by a straight current carrying line. The resonant method (phase method) response is shown with a solid (dashed) line.

vibrations are relatively less important, and the phase noise is reduced. The gray trace from Fig. 6.6 is more than two orders of magnitude larger than the dashed trace from Fig. 6.7 since the applied current in the former measurement was about 180 times smaller than that applied in the latter one. That is why the signal to noise ratio is much smaller in Fig. 6.7.

6.5 Force sensitivity: thermal noise

The limit in the force sensitivity of a scanning probe microscope is set by how the thermal noise affects the zero point motion of the cantilever. Other sources

of noise like laser fluctuations and vibrations have been shown to be much smaller than the thermal noise, so they can be disregarded [70]. A typical cantilever has effectively one degree of freedom, namely, flexion in the vertical direction. All the other flexural, torsional, and compressional degrees of freedom are effectively frozen since their stiffness is much larger. From the energy equipartition theorem, it is clear that at temperature T random thermal fluctuations in the oscillation amplitude of the cantilever have an average energy $k\delta Z^2/2 = k_B T/2$, where k_B is Boltzmann's constant. This means that the rms amplitude of the fluctuations is $\delta Z = \sqrt{k_B T/k}$. This vibrational noise is the result of a noise force that excites the end of the cantilever. The force noise is characterized by a flat power spectrum S_N [29][6], which means that the cantilever is driven with the same force at every frequency. Relating the force noise power to the rms displacement of the cantilever requires solving equation (6.14) replacing the external force by a driving term which is constant at all frequencies. This can be easily done in Fourier space, where the equation can be solved directly as

$$\tilde{Z}(\omega) = \beta(\omega)\frac{\sqrt{S_N}}{k}, \tag{6.18}$$

with $\tilde{Z}(\omega)$ the Fourier transform of $Z(t)$ and $\beta(\omega)$ the enhancement factor defined in equation (6.17). The mean square amplitude of the fluctuations is given by $\delta Z^2 = \int_{-\infty}^{\infty} |Z(t)|^2 dt$. By using Parseval's theorem

[6] S_N, the force noise power, has units of N^2/Hz, since it is the time integral of the square of the force.

$$\int_{-\infty}^{\infty} |Z(t)|^2 dt = \int_{-\infty}^{\infty} |\tilde{Z}(\omega)|^2 d\omega, \tag{6.19}$$

together with equation (6.18) and replacing δZ^2 by $k_B T/k$, it can be shown that the force noise in a bandwidth B, or equivalently the minimum detectable force, is given by

$$F_{min} = \sqrt{S_N B} = \sqrt{\frac{2kk_B T}{\pi Q f_0} B}, \tag{6.20}$$

where $f_0 = \omega_0/2\pi$. On the other hand, the spring constant of a rectangular cantilever can be approximately calculated from its length l, thickness t, and width w using $k = Ewt^3/(4l^3)$ [71], where E is the Young modulus. Therefore in terms of the dimensions of a cantilever with a uniform cross section[7], the minimum detectable force is given by

$$F_{min} = (\rho_M E)^{1/4} \left(\frac{wt^2}{lQ}\right)^{1/2} (k_B T B)^{1/2}, \tag{6.21}$$

where ρ_M is the density of the cantilever. Therefore the sensitivity of the cantilever can be increased by decreasing its width and thickness or by increasing its length and quality factor. The etched silicon cantilevers used in the experiment had approximate dimensions $l = 225\mu m$, $w = 28\mu m$, and $t \approx 3\mu m$, which are typical for commercially available cantilevers. However, the thickness of cantilevers is hard to control during processing so the values given by the manufacturer and the actual

[7]For such a cantilever the resonant frequency is given by $\omega_0 = \sqrt{k/m^*}$ where m^* is the effective mass at the tip, equal to 1/4 of the mass of the cantilever.

measured thickness can be different. In order to solve this difficulty, the thickness of the cantilever is taken to be unknown, so it is found in terms of the resonant frequency and the spring constant. Therefore, if the Young's modulus of the cantilever is known, the spring constant can be calculated to a good approximation by measuring the resonant frequency of the cantilever and using the relation [71]

$$k = 2\pi^3 l^3 w \sqrt{\rho^3/E}(f_0^3). \tag{6.22}$$

For a resonance frequency of 56.8 kHz the calculated spring constant is 1.2 N/m. Typical values of the quality factor at atmospheric pressure are in the 140-150 range. According to equation (6.20), at room temperature the force resolution per square root bandwidth for such a cantilever is $19 \times 10^{-15} N/\sqrt{Hz}$. This value is typical for commercially available cantilevers at room temperature and atmospheric pressure. Reducing the temperature to 4.2^oK reduces the noise by a factor of 8, and operating under vacuum can increase the quality factor 50 to 500 times [72], reducing the noise by a factor between 7 and 20. Reducing the width and thickness of the cantilever by factors of 4 and 10 respectively decreases the noise by a factor of 20. If all this improvements are made the noise can be reduced by a factor of about 3200, giving a force resolution of 6 attoNewtons per square root bandwidth [29].

6.6 Cantilever Calibration

The deflection of the cantilever is measured by the photodetector in units of volts. The conversion factor α to real units of displacement, like nanometers, depends on

details of the cantilever placement with respect to the laser, which can change for every measurement. The conversion factor can be defined as $\alpha = Z/V$, where Z is the real displacement and V is the photodetector signal. Additionally, if the signal is to be converted to an equivalent force, it is necessary to use a model such as that given by 6.14, which predicts that the amplitude response of the cantilever at a frequency ω is given by $Z_\omega = \beta(\omega)F/k$. Therefore the measured force at a frequency ω is related to the photodetector voltage at that frequency by

$$F_\omega = k\alpha V_\omega/\beta(\omega). \tag{6.23}$$

This means that knowledge of the spring constant k and the conversion factor α are necessary to correctly scale the measured signal to units of force. In the case of magnetic signals another calibration factor is important. In that case the magnetic field, or the magnetic field gradient, are the quantities that need to be measured, so a connection between them and the force felt by the cantilever has to be made. According to equation (6.11), this force is the convolution of the z derivative of the field with the magnetization of the tip, which is also unknown, hence by using both (6.23) and (6.11) it can be shown that the measured voltage at the photodetector produced by the magnetic interaction between some field $\vec{B}(\vec{r})$ and the magnetization of the tip $\vec{M}(\vec{r})$ is

$$V_\omega(\vec{r}) = \int [\vec{M}(\vec{r'})\beta(\omega)/(k\alpha)] \cdot \frac{\partial \vec{B}(\vec{r}+\vec{r'})}{\partial z} d^3r'. \tag{6.24}$$

This means that the unknown conversion factor α, spring constant, and magneti-

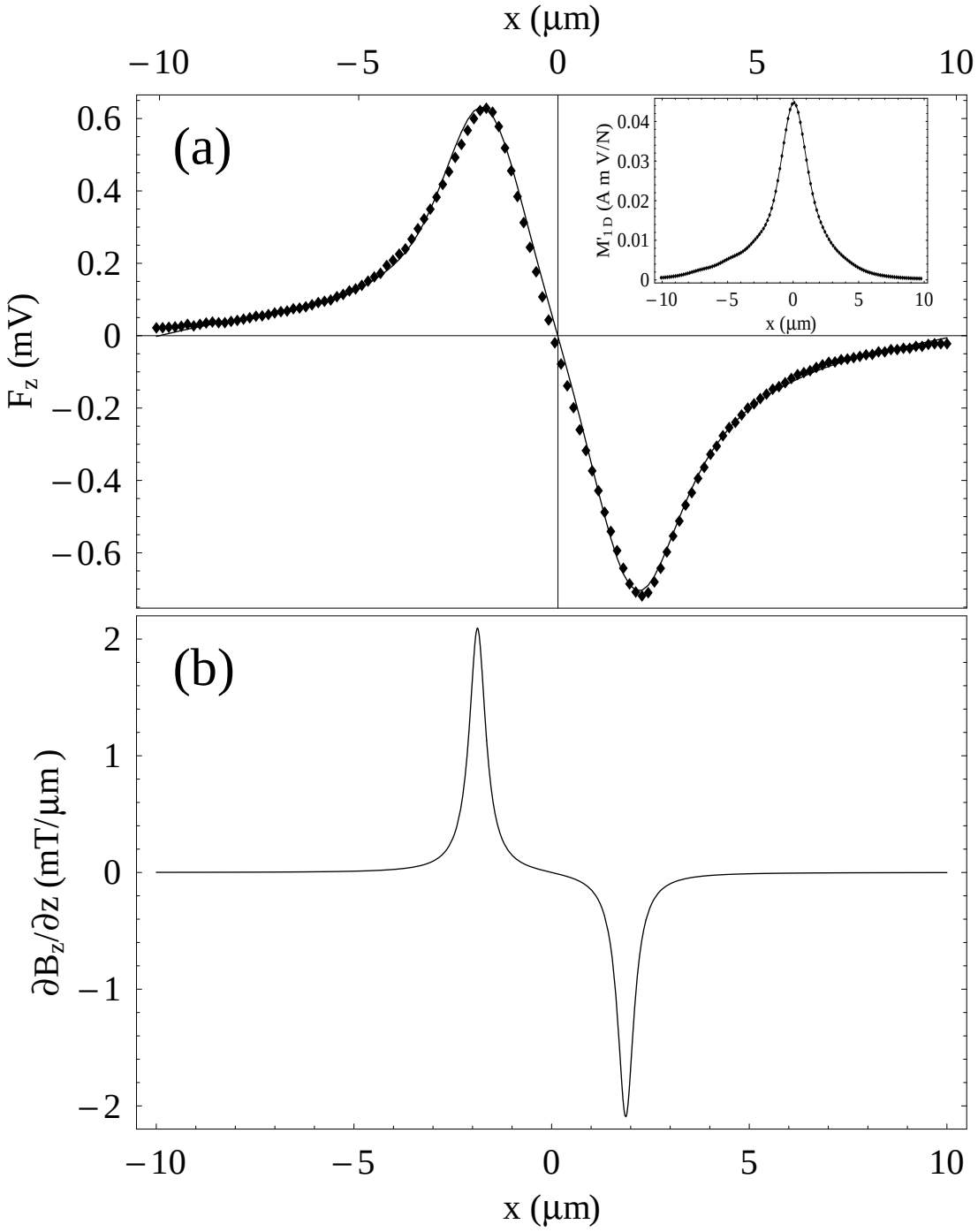

Figure 6.8: (a) Position dependence of the magnetic signal measured by the cantilever (diamonds) at a scan height z=300 nm above the sample. Since the field is independent of y, only the x dependence is shown. The solid line shows the convolution of the expected signal [shown in (b)] with the 1D convolution factor of the tip [shown in the inset of (a)].

zation of the tip can be joined as a single unknown convolution factor $\vec{M}'(\vec{r}) = \vec{M}(\vec{r})\beta(\omega)/(k\alpha)$. By measuring the cantilever response to the field produced by a straight current carrying Cu wire of known dimensions, which can also be calculated analytically, the convolution factor can be found by an iterative procedure known as the "Maximum Entropy Algorithm" [73, 74].[8] First, the response of the cantilever is measured in the $x - y$ plane, with the tip at a given height above the sample. This gives an image as shown by the diamonds in Fig. 6.8 (a) in units of Volts. Only a section at constant y is shown, since the field has negligible y dependence. The magnetic field produced by the current carrying line can be easily found using Biot-Savart's law. The result of the calculation of the expected signal is shown in Fig. 6.8 (b). Experimental broadening of the features of Fig. 6.8 (b) is clear in Fig. 6.8 (a) due to the smearing effect of the magnetization of the cantilever tip, which is not a localized dipole but is instead distributed over an area with dimensions of the order of μm. An ansatz for the convolution factor is given and iteratively changed to minimize the difference between the measured signal and the convolution of the predicted signal. A typical 1-D convolution factor is shown in the inset of Fig. 6.8 (a). To show the quality of the procedure, the calculated signal shown in 6.8 (b) was convoluted with the 1-D convolution factor, and plotted in Fig. 6.8 (a) with a line. The measured signal (diamonds) and the convolution of the calculated signal with the 1-D convolution factor (line) agree very well.

[8]This algorithm will not be described here. One important comment, however, is that the Maxwell equations constrain the magnetic field so that measurements of B_z in a single $x - y$ plane at a particular height z are enough to find B_z anywhere else in space, as long as the magnetization and the currents remain in the $x - y$ plane. Details can be found in the Appendix.

It is possible to directly obtain information about the resolution of the cantilever in terms of magnetic field gradient without any information about the conversion factor α, the spring constant, or the magnetic moment of the tip. For that purpose it is necessary to measure the cantilever noise. This can be extracted from the variance in the roughness of the data, which can be found by finding the difference between the real data and a smoothed version of the data. The noise as a function of frequency for the cantilever used for the experiments is shown in Fig. 6.9. At a bandwidth of 1Hz the noise is 1μV. From Fig. 6.8 the relation between photodetector output (mV) and field derivative (mT/μm) can be found, therefore a noise of 1μV is equivalent to a field gradient of $\approx 3\mu$T/μm. The gradient produced by the excess magnetization for realistic values of the current, the spin relaxation length, and the resistivity of Py and Cu, was estimated to be 4μT/μm at the beginning of this chapter [9]. Therefore it seems possible to detect the spin polarization of electrons using MFM under the conditions specified before (see last footnote, and discussion of Fig. 6.4), as long as a bandwidth equal to or smaller than 1 Hz is used.

If the cantilever noise is assumed to come completely from thermal excitations [70], an additional calibration can be made. As shown in equation (6.20), the thermal noise increases with the square root of the bandwidth, and for typical cantilevers used in the experiment, it is $19 \times 10^{-15} N/\sqrt{Hz}$. Figure 6.9 shows the measured noise of the cantilever in μV, together with a linear fit with slope 0.93 $\mu V/\sqrt{Hz}$.

[9] See Fig. 6.4(b) where the gradient produced by the excess magnetization for a 9.1 mA current through a 1.2 μm wide wire was calculated for the case of transparent F-N interfaces. The calculated value of the spin current polarization in this case is approximately 5%.

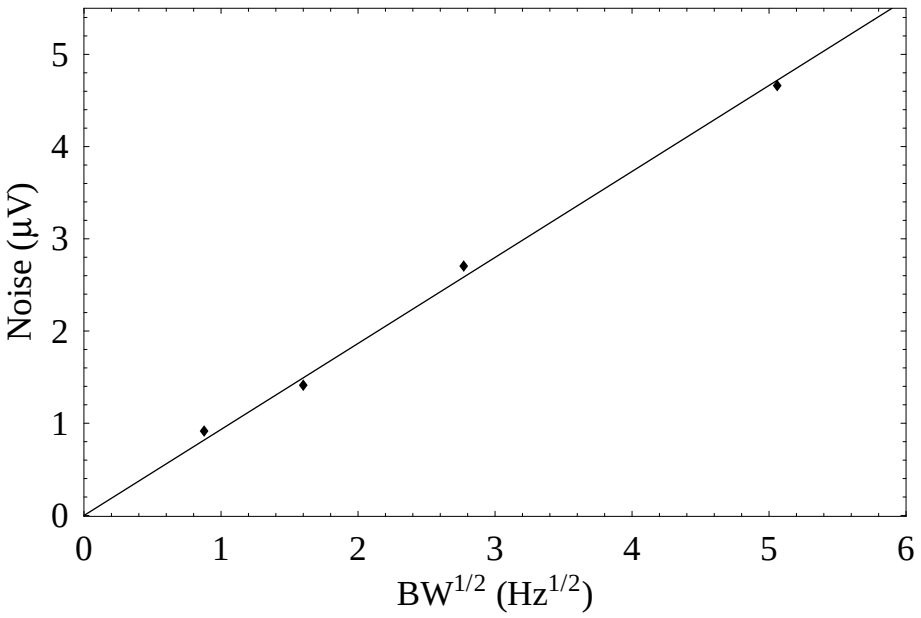

Figure 6.9: Measured cantilever noise as a function of bandwidth, with linear fit.

By comparing the expected and measured noise a scaling factor of 20 $\times 10^{-9}$ N/V is found, which is valid only for signals measured at resonance.

By integrating the magnetization $\vec{M}(\vec{r})$, which can be found directly from the convolution factor $\vec{M}'(\vec{r})$ by using values for α (obtained from the noise calibration) and k (measured by measuring the resonant frequency), the effective magnetic moment of the cantilever can be found to be 0.6×10^{-15} A m^2, which is smaller than the estimated real magnetic moment. This effective magnetic moment is not the real magnetic moment of the tip, but the weighted moment over all possible heights, where the weighing function is determined by how fast the magnetic field decays in the z direction. [10] Higher order (2-D) convolution factors can be found by using not a single current carrying line but two non-parallel lines, since in this case the field

[10] See equation (A.35) in the Appendix for a precise definition of the 1-D convolution factor.

is a function of both x and y.

Chapter 7

Spin injection and magnetic force microscopy detection II: Experiment

In the previous chapter I explained the basic concepts behind the idea of spin injection and MFM detection, and showed that MFM offered the resolution and sensitivity to detect the field produced by an excess magnetization created by injection of spin polarized conduction electrons from a ferromagnetic into a nonmagnetic metal. However, the field produced by this excess magnetization is much smaller than the fields produced by the magnetic injector and the current, so that a new measurement setup that would filter out unwanted magnetic signals had to be developed. Additionally, a different sample fabrication procedure was used, in an effort to fabricate flat Cu-Py-Cu wires with no additional topographical features at the Cu-Py interfaces. Finally, since the cantilever is not only sensitive to magnetic fields but also to electric fields, it was necessary to balance the potential difference between the tip of the cantilever and the scanned region of the sample to avoid the appearance of additional unwanted signals. I will begin this chapter by discussing the principle of operation and the experimental setup. Then I will describe the flat sample fabrication process and the balancing of the electric potential, and finally I will present results of the measurements.

7.1 Principle of operation

Estimations of the size of the spin injection signal detected by the cantilever showed that this signal is more than 200 times smaller than the signal produced by the current circulating through the sample. The signal produced by the magnetic material is larger but of the same order as that produced by the current, so it is necessary to design a way to separate the small spin injection signal from the very large background produced by both the current and the magnetic material. This can be done by taking advantage of the nonlinearity of the excess magnetization in the nonmagnetic metal, which depends on the product of the magnetization within the magnetic material and the injected current. A magnetic injector with large aspect ratio and small (submicron) dimensions has a very sharp hysteresis curve such that a magnetic field applied along the easy geometrical axis will only flip the magnetization into either of the two easy directions. Therefore the magnetization of the injector is expected to be in any of two possible states. If the applied magnetic field, large enough to flip the magnetization of the injector, is reversed with a frequency ω_1, the magnetization of the injector will change direction with the same frequency, $\vec{M} = M\hat{x}(1 - 2\Theta[\sin(\omega_1 t)])$, where $\Theta(t)$ is the step function, and the easy axis is defined to be in the x direction. If the injected current is made to oscillate at frequency ω_2 such that $I(t) = I\sin(\omega_2 t)$, the excess magnetization δM will have a time dependence of the form $\delta M \propto (1 - 2\Theta[\sin(\omega_1 t)])\sin(\omega_2 t)$. By expanding the step function in a series and developing the products, it can be shown that terms of the form $\cos(\omega_1 \pm \omega_2)$, $1/3\cos(3\omega_1 \pm \omega_2)$, $1/5\cos(5\omega_1 \pm \omega_2)$, ... appear. What this

means is that by flipping the magnetization with frequency ω_1 and by injecting a current with frequency ω_2, the field from the excess magnetization can be measured at a frequency $\omega_1 + \omega_2 \neq \omega_1 \neq \omega_2$, so by using phase sensitive detection each of the signals can be distinguished from each other. If the frequencies are chosen so that $\omega_1 + \omega_2 = \omega_0$, the complete equation of motion of the tip can be written as

$$\begin{aligned}
\frac{1}{\omega_0^2}\ddot{Z} + \frac{1}{Q\omega_0}\dot{Z} + Z = \quad & \frac{1}{k}\left[F_0 + F_{\delta M}|_{Z_0} + \left.\frac{\partial F_{\delta M}}{\partial Z}\right|_{Z_0}(Z - Z_0)\right]\exp(i\omega_0 t) \\
+ \quad & \frac{1}{k}\left[F_M|_{Z_0} + \left.\frac{\partial F_M}{\partial Z}\right|_{Z_0}(Z - Z_0)\right]\exp(i\omega_1 t) \\
+ \quad & \frac{1}{k}\left[F_I|_{Z_0} + \left.\frac{\partial F_I}{\partial Z}\right|_{Z_0}(Z - Z_0)\right]\exp(i\omega_2 t), \qquad (7.1)
\end{aligned}$$

where $F_{\delta M}$, F_M, and F_I are the forces produced by the excess magnetization, the magnetic material, and the current, expanded to first order in Z. To lowest (zeroth) order in Z the solution to equation (7.1) at frequencies ω_0, ω_1, and ω_2 is given by

$$Z^0_{\omega_0} = \frac{(F_0 + F_{\delta M})}{k}\beta(\omega_0) = \frac{\imath Q}{k}(F_0 + F_{\delta M}) \qquad (7.2)$$

$$Z^0_{\omega_1} = \frac{F_M}{k}\beta(\omega_1) \qquad (7.3)$$

$$Z^0_{\omega_2} = \frac{F_I}{k}\beta(\omega_2). \qquad (7.4)$$

where $\beta(\omega)$ is the enhancement factor defined by equation (6.17) in the previous chapter, which is equal to $\imath Q$ at resonance. Therefore measurements at these three different frequencies yield independent information on $F_{\delta M}$, F_M, and F_I. If the frequencies ω_1 and ω_2 are away from the resonant frequency ω_0, the enhancement

factor at those frequencies will be much smaller than Q . The first order solution at frequencies ω_0 and $2\omega_0$ is given by

$$z^1_{\omega_0} = \frac{\imath Q}{k}\left[z^0_{\omega_1}\frac{\partial F_I}{\partial z} + z^0_{\omega_2}\frac{\partial F_M}{\partial z}\right]_{z_0} \tag{7.5}$$

$$z^1_{2\omega_0} = z^0_{\omega_0}\left.\frac{\partial F_{\delta M}}{\partial z}\right|_{z_0}\frac{\imath Q}{k(2-\imath 3Q)}. \tag{7.6}$$

Other first order solutions, which are not important, have been left out. The significance of equation (7.5) is that at frequency ω_0 not only $F_{\delta M}$ is detected [equation (7.2)] but also the derivatives of F_M and F_I. Therefore depending on the magnitude of the force from the magnetic material and the current, the frequencies ω_1 and ω_2 should be chosen to attenuate $z^0_{\omega_1}$ and $z^0_{\omega_2}$ such that the largest component of z_{ω_0} comes from $z^0_{\omega_0}$, that is, from $F_{\delta M}$, instead of from $z^1_{\omega_0}$.

7.2 Experimental setup

The setup that was used for the experiment is shown in Fig. 7.1. The signal from the photo-detector, which carries the information of the cantilever deflection, is connected to the input of three lock-in amplifiers, a Princeton Applied Research PAR-5209 that measures the signal from F_M at $\omega_1 = 4kHz$, a Stanford Research SR-844 that measures the signal from $F_{\delta M}$ at $\omega_0 = 56.8kHz$ set by the resonant frequency of the cantilever, and a Princeton Applied Research PAR-124 that measures the signal from F_I at $\omega_2 = 60.8kHz$[1]. The signal that drives the cantilever at its resonant frequency (56.8 kHz in the diagram) is used to reference the Stanford

[1]This frequencies vary depending on the cantilever used.

Figure 7.1: Diagram of the experimental setup. Three lock-in amplifiers are used to detect the cantilever response at different frequencies, to independently measure the fields produced by the magnetic material, the current, and the excess magnetization from spin injection.

SR844 lock-in and is also connected to the R input of a Mini-Circuits ZAD-8 frequency mixer. The internal oscillator of the PAR-124 lock-in (set to 60.8 kHz in the diagram) is connected to the L input of the mixer, and to a switch triggered by the computer. The output of the switch, which is equal to the input oscillatory signal when the switch is on and zero when the switch is off, is connected to a 200 Ω resistor, at which the voltage is measured, and then to one of the terminals of the sample (the other terminal of the sample is grounded). The switch is used to acquire consecutive points with and without current through the sample in order to distinguish the real effect from artifacts such as laser interference. The output of the mixer is the superposition of two signals with frequencies $60.8kHz - 56.8kHz = 4kHz$ and $60.8kHz + 56.8kHz = 117.6kHz$. After an 80kHz RC low-pass filter the higher frequency component is attenuated enough so that the signal only triggers the Hewlett Packard HP-3314A function generator at 4kHz. The TTL output of the function generator is used to reference the PAR-5209, while its main signal output is used to create an adjustable amplitude square wave that is amplified using an HP-6826A to a level high enough to drive a current through the magnet. However, due to the magnet's finite inductance, the current is not a square wave anymore and its magnitude is reduced. This is not crucial for the experiment if the magnetic injector has a very sharp transition in the hysteresis curve, as it only introduces a phase lag in the applied field, and if the signal can be amplified enough so that the inductive damping is not important. Finite amplification of the electronics used in the experiment limited the maximum frequency of the field to about 4kHz. The

magnet was fabricated by winding a copper wire coil on a thin nonmagnetic stainless steel cylindrical shell about 8mm long with a 3mm inner diameter filled with a soft magnetic core. The coil and core were fixed to the steel shell with GE varnish. The magnet was mounted on an aluminum support structure on the sample holder, less than 2mm away from the magnetic injector, and held in place with Apiezon H grease which also provided good thermal contact to the holder[2]. The adjustment of the magnet position and orientation were made by eye, so even though the main component of the field was parallel to the easy axis of the magnetic injector, small transverse components, both in and out of plane, remain. However, if small enough, this components do not directly affect the measurement. Calibrations of the magnet were not very useful since the relative position between the injector and the magnet changed for every measured sample. However, it was experimentally seen that the magnet was close enough to switch the magnetization of the injector in both directions, which is the only relevant fact for the experiment.

7.3 Flat sample fabrication

In order to avoid crashing the sample and the tip, the topography of one line of the sample is acquired, after which the tip is raised to a specified position above the average baseline measured in the topography scan, and the magnetic response is measured. Therefore any roughness in the topography affects the actual height at which the magnetic scanning is being done. This means that variations in the magnetic signal from one line to the next can appear simply because of variations

[2]Good thermal contact was important since the magnet heated up when driven at high currents.

in the topography. To avoid this problem it is desirable to fabricate completely flat samples, or at least samples in which the topography of each line is the same (so that all the magnetic field line scans are done in the same conditions). In the case of a wire made of a single material this can be achieved by good lithography and clean lift-off. However, since the samples must have interfaces between magnetic and nonmagnetic materials, the problem gets more complicated. In principle a Cu-Py-Cu wire as shown in Fig. 6.2 or Fig. 7.2 (f) will have uniform topography along the y axis, solving the problem. This kind of structure can be fabricated as follows. A permalloy film is thermally evaporated on a clean substrate. Then a bilayer of PMMA is used to coat the wafer, and e-beam lithography followed by developing, as explained in chapter 4, are used to define a mask as shown in Fig. 7.2(a). The sample is placed in a vacuum chamber and ion milling is done as explained in chapter 4 to remove all the permalloy from the unprotected region [Fig. 7.2(b)]. The four terminal resistance of a co-evaporated wafer is used as an in-situ detector to evaluate when all of the permalloy film has been removed. Then an equivalent amount of Cu is thermally evaporated to fill up the hole left by the milling process [Fig. 7.2(c)]. A second step of PMMA covering, e-beam lithography, and developing is done to define the mask shown in Fig. 7.2(d). The sample is ion milled once more to trim the Cu-Py-Cu wire to the proper width by completely removing any metal outside the masked area [Fig. 7.2(e)]. Once again the four terminal resistance of a co-evaporated wafer is used to decide when all the metal has been removed. The result is a wire with a uniform cross section in y as shown in Fig. 7.2(f). However, due to

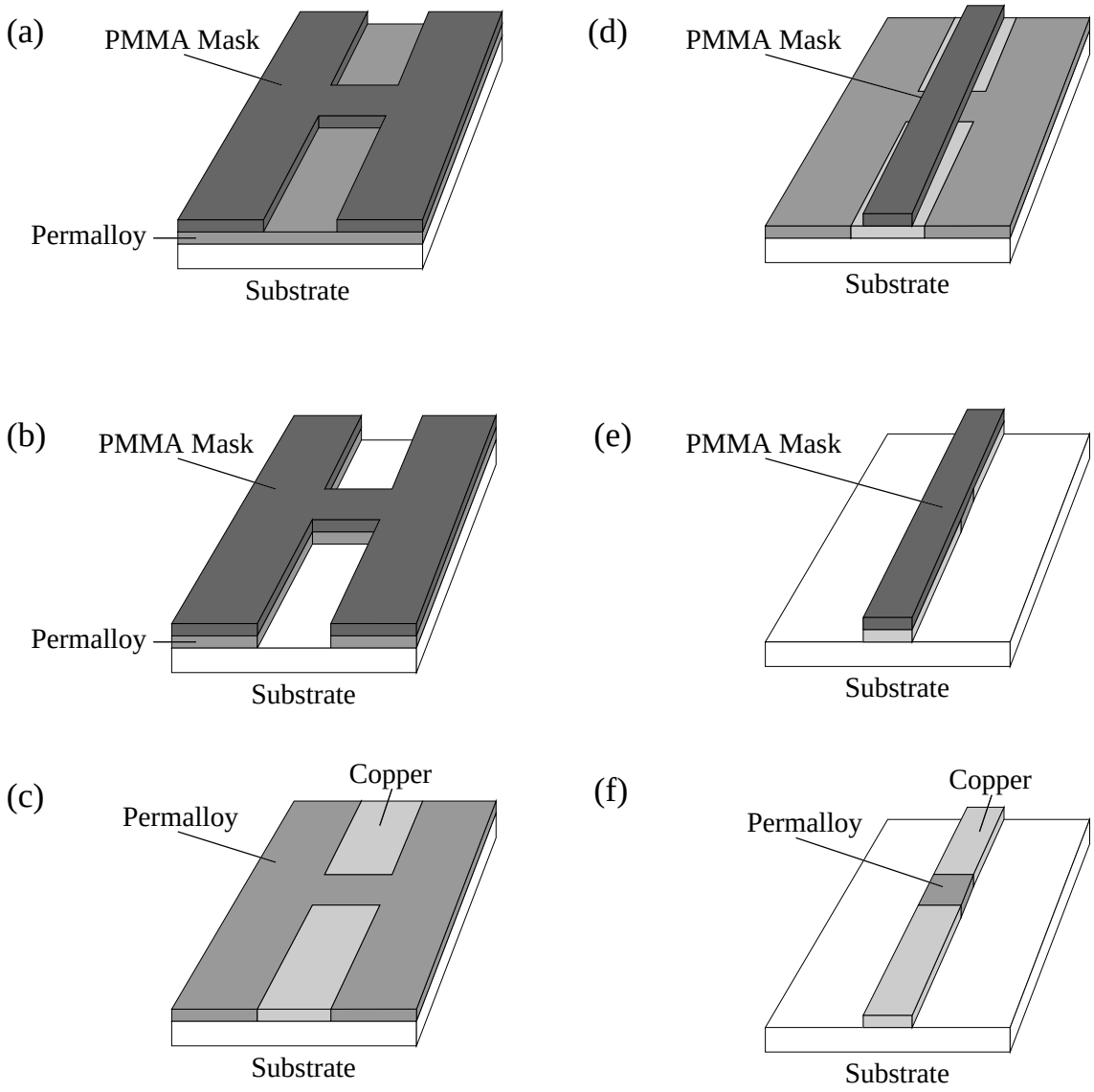

Figure 7.2: Flat sample fabrication steps. (a) A PMMA mask is defined on top of a uniform Py film. (b) Ion milling is used to remove unprotected Py. (c) The hole left by ion milling is filled up with Cu. (d) Second PMMA mask is defined. (e) Ion milling is used to trim the Cu-Py-Cu line to the desired width. (f) Final result.

slightly different milling rates for Py and Cu, or because the evaporated Cu did not completely fill up the hole left by the Py milling, small variations in topography are always present, but they are smaller than with the previous fabrication technique.

7.4 Electric potential balancing

Since the tip of the cantilever is covered by a magnetic metal, the cantilever can experience a force due to capacitive coupling with the sample. In order to minimize this effect it is necessary to tune the voltage in the cantilever to make it as close as possible to the voltage of the scanned area of the sample. This can be achieved by designing the samples with an additional Cu wire in parallel with the main Cu-Py-Cu wire as shown in Fig. 7.3. If the voltage at the top and bottom of the sample is given by V_1 and V_2, the voltage in the metal at the position of the centered dotted line is given by $V_0 = (V_1 + V_2)/2$, assuming equal contact resistances at each of the F-N interfaces. This voltage is the same at both the left and right arms of the sample as long as the wires have a uniform cross section, even if they do not have exactly the same width. The tip of the cantilever usually scans a region of the right wire within 1-2 μm of the dashed line, so if the cantilever is electrically connected to the side wire of the left arm, the potential difference between the tip and the scanned region of the sample will be less than 1.4 mV for current densities as high as $2.4\times10^{10}\mathrm{A/m^2}$. According to numerical and analytical calculations [75, 76] the force between an infinite plane and the tip is about 3×10^{-15}N for the tips used in the experiment, and for a 1.4 mV potential difference. This force should be reduced in the case of a wire and be much smaller than the value 19×10^{-15} which

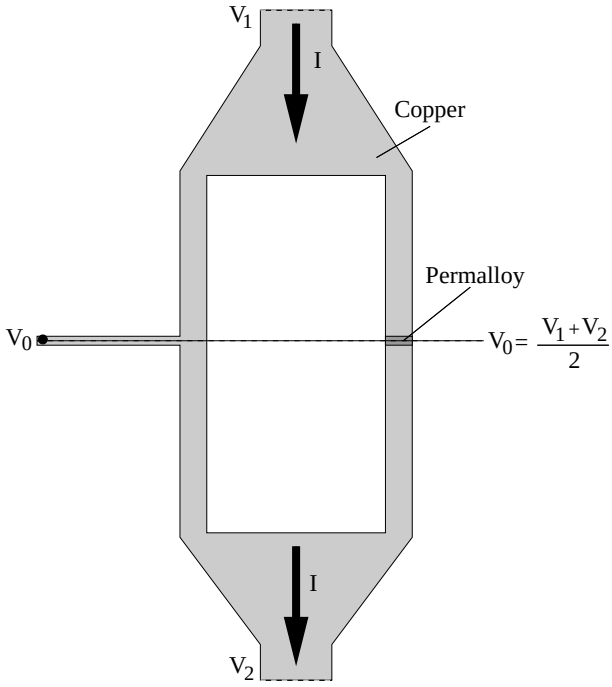

Figure 7.3: Schematic of the sample layout for balancing the voltage on the cantilever, which is connected to the point with voltage V_0 on the left wire.

is the minimum detectable force at a 1Hz bandwidth due to thermal vibrations of the cantilever. However, unbalanced electric potentials of 4mV are large enough to produce a force equivalent to the noise, so care must be taken to distinguish any small residual capacitive effect from the magnetic effect that is being measured. If necessary, symmetry properties of the electrostatic interaction can help distinguish it from the expected signal.

7.5 Results

An AFM image of a typical Cu-Py-Cu wire is shown in Fig. 7.4. Even though the method discussed in section 7.3 was used to fabricate the sample, some variation in the thickness can be seen. The dip corresponds to the region where permalloy

remains while the higher regions are made of copper.[3] The width of the wire is 1.5 μm and its thickness 57 nm, even though the figure shows a bigger thickness since part of the substrate was milled during fabrication. The thickness variation of the wire due to the dip is about 20 nm, which causes a change in the scanning height of the cantilever close to 10 nm, which is small compared with the scanning height of 300 nm used for the magnetic field measurements. Furthermore, since the field of the spin polarized electrons injected into Cu is what we want to measure, only the

[3]Better samples were obtained but no complete set of measurements was taken for them.

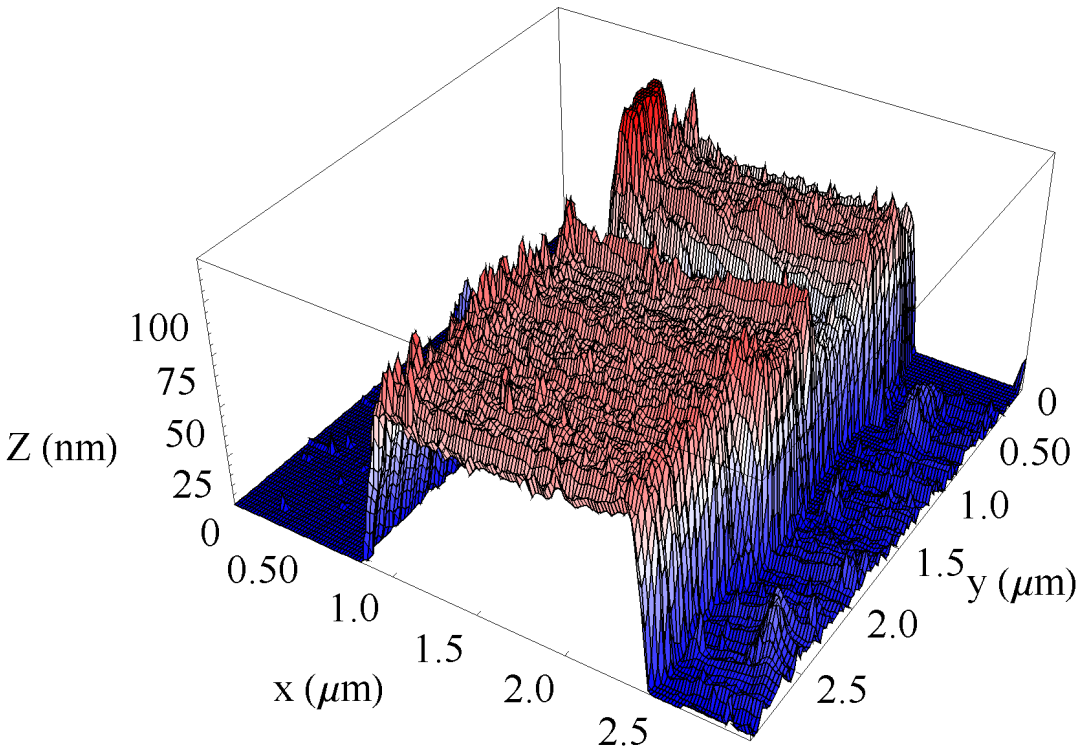

Figure 7.4: Topography of the wire near the Cu-Py-Cu interfaces.

signal in Cu just after the injection point is relevant, so small topography changes in the Py region are not important.

The cantilever signal at a frequency of 60.8kHz, the frequency at which current is being driven into the sample, is shown in Fig. 7.5. The signal has the characteristics of the field produced by a uniform current carrying wire which were observed in the previous chapter (Fig. 6.8). A similar procedure as that used in section 6.6 can be followed to obtain the convolution factor. The current driven through the wire is 2 mA, which gives a current density of $2.34\times10^{10}\mathrm{A/m^2}$.

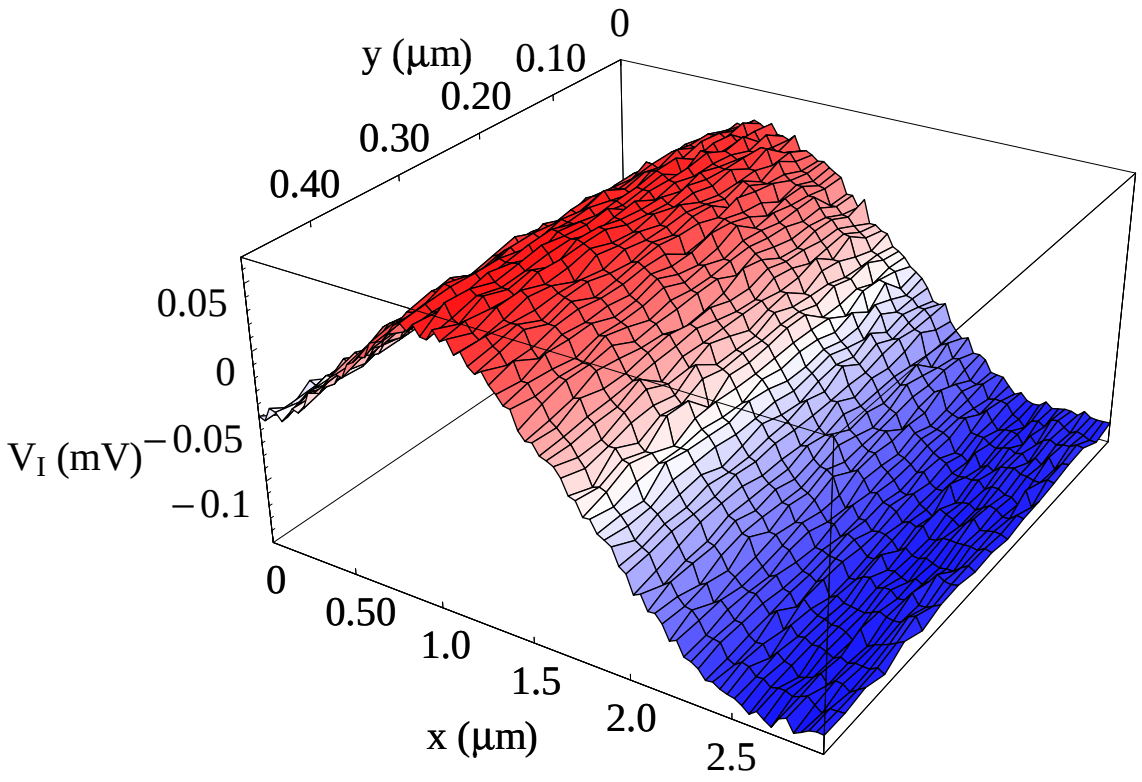

Figure 7.5: Measured cantilever response to the magnetic field produced by the current at a frequency of 60.8 kHz.

The force produced by the magnetic injector is detected by measuring the cantilever response at 4kHz, which is the frequency at which the magnetization of the injector is being reversed. Figure 7.6 shows the measured cantilever deflection as a function of position for the sample shown in Fig. 7.4 before using any conversion factor or applying any deconvolution. A dipole field structure at the place of the magnetic injector can be seen. It is important to point out that Figs. 7.5 and 7.6 give the cantilever deflection as measured by the photodetector, and not the force. Therefore it is not correct to directly compare them to conclude that the

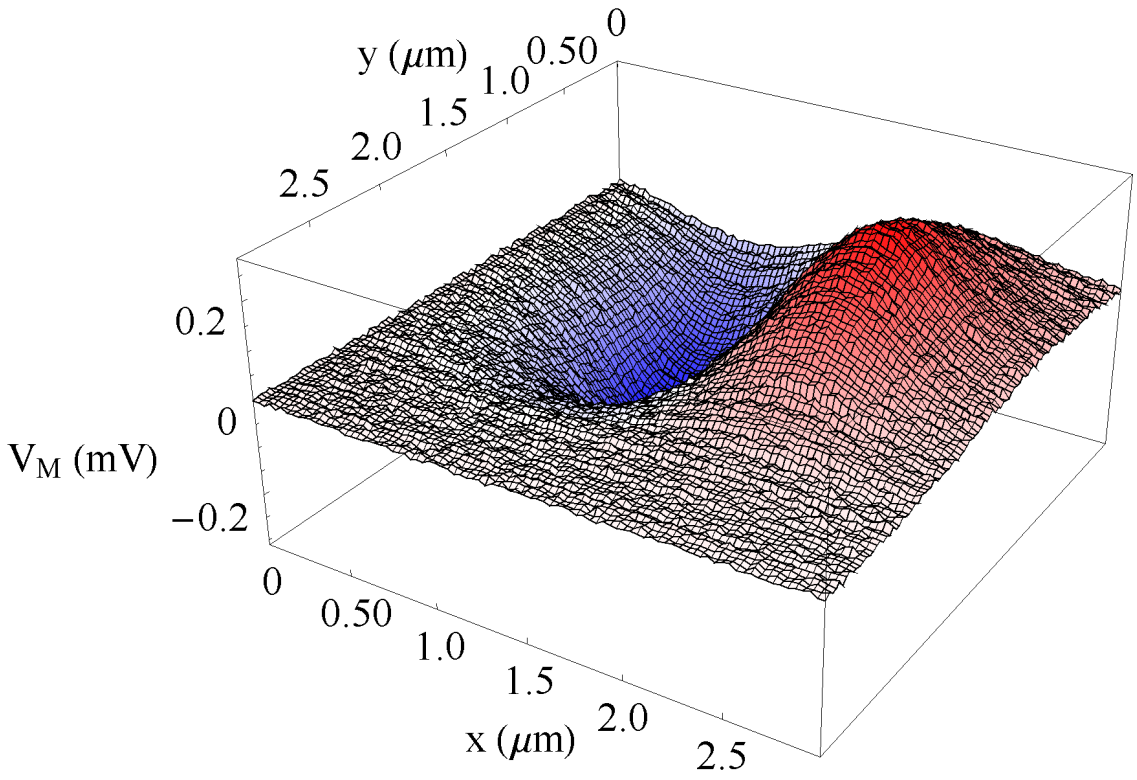

Figure 7.6: Measured cantilever response to the field produced by the magnetic injector at a frequency of 4.32kHz.

force is similar in both cases. A correct comparison can only be made after scaling each of the measured amplitudes by the factor $\beta(\omega)$ defined by equation (6.17) which characterizes the response of the system to a force F at a frequency ω, and assuming that the 2D convolution factors are equivalent. The values of β are -6.84+0.34$\imath$ for the force produced by the current and 1.006+0.0005$\imath$ for the force produced by the magnetic injector, which means that the force produced by the current is about 7 times smaller than that produced by the magnetic injector, even for a current density as high as 2.34×10^{10}A/m^2.

The response of the cantilever at its resonant frequency is shown in Figs. 7.7 and 7.8, at two perpendicular phases. The in and out of phase components are acquired directly and then, for each of them, the signals with and without current are subtracted[4]. The resulting two images at phases 0^o and 90^o are then combined to generate two new images at phases 15^o and 105^o, which are the ones presented here. This is done since in and out of phase are not well define due to unaccounted phase lags, and the 0^o and 90^o images seem to have components of the same data. The additional rotation angle of 15^o is chosen so that the images appear to be independent.

Some features are clearly visible in Fig. 7.7, where the signal would appear to be only about ten times smaller than that produced by the magnetic injector. However, after scaling it by the factor $\beta(\omega_0) = \imath Q$ where the quality factor Q is 147,

[4]It is worth noting that points with and without current are acquired consecutively instead of line by line so the subtraction technique is very effective in removing additional artifacts like laser interference.

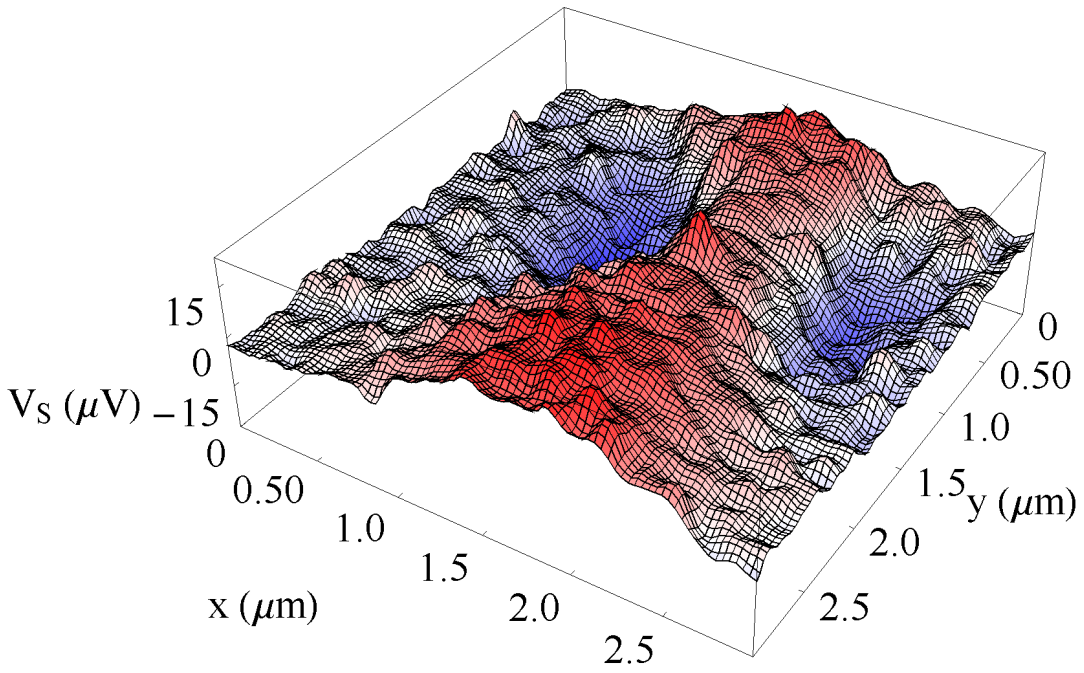

Figure 7.7: Measured cantilever response at a frequency of 56.8 kHz and 15 degrees phase.

this signal is about 1500 times smaller than that produced by the magnetic injector. This shows how the setup allows the extraction of very small signals that are buried in much larger unwanted backgrounds, which was impossible with the standard magnetic force microscopy setup and phase operation. The signal to noise ratio is observed to be about 4.5. The features that can be observed in Fig. 7.7 are first, an increased signal (red) throughout the center of the scanning area (at x=1.5μm) with a width of about 1.5μm (the center position and width of this feature agree with the position and width of the wire) and a size of about 18μV. And second, two regions

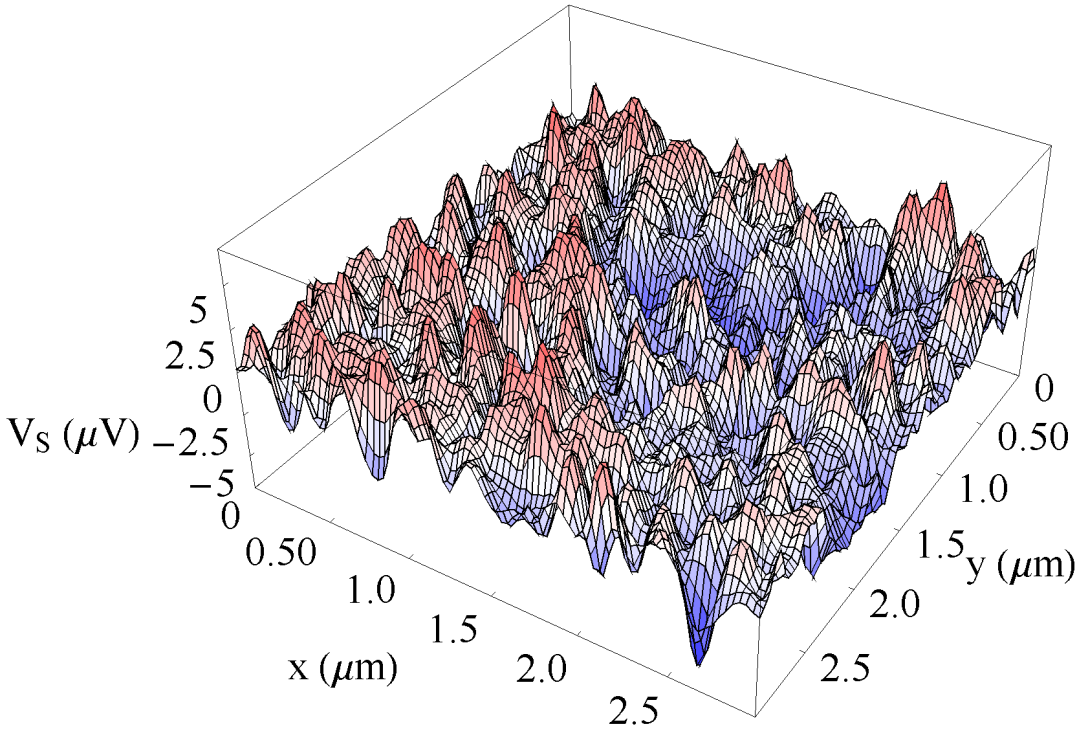

Figure 7.8: Measured cantilever response at a frequency of 56.8 kHz and 105 degrees phase.

of decreased signal (blue) to the sides, at the y coordinate at which the magnetic injector is found. None of these features has the correct symmetry expected for the field produced by a decaying excess magnetization in Cu (see Fig. 6.4), so the expected signal must be buried within the noise, and the observed features must have a different origin.

It was pointed out in section 7.4 that the electric sensitivity of the tip was a concern, hence the electric potential in the tip was balanced so that it would be

as close as possible to the electric potential in the scanning area. Additionally, the sample was mounted on a metallic plate which was set at the same potential as the tip, to create a uniform background electric potential. However, the red feature in Fig. 7.7, which extends over the width and length of the metallic line, seems to be caused by changes in the capacitance between the tip and the metallic wire as the tip scans over the wire, together with an x dependence of the electrostatic potential due to the presence of the wire. For a 10 mV potential difference along the x axis, the estimated electrostatic force (see section 7.4) is about 140×10^{-15}N. From Fig. 7.7 the noise can be measured to be 1.77μV at a bandwidth of 1 Hz, and assuming that it is completely thermal in origin (as done at the end of section 6.6), the calibration factor 10.7×10^{-9}N/V can be found[5]. According to this factor the size of the red feature is 193×10^{-15}N, which is close to the estimated value, confirming that this feature can be due to electrostatic effects since it agrees both qualitatively and quantitatively with what is expected (within the roughness of the estimations of the unbalanced potentials).

The other feature observed in Fig. 7.7 (the blue dips) can be explained by equation (7.5), which shows that at the fundamental frequency not only the effect of the excess magnetization can be detected but also a higher order signal coming from the product of F_I, F_M, and their derivatives can be measured. In order to confirm this idea, it is necessary to rewrite equation (7.5) in terms of the measured signals. This can be done by using the special property of the magnetic fields generated by

[5]This factor is only valid for scaling signals that have been measured at resonance.

a current and an in plane magnetic moment [see equation (A.22) in the Appendix],

$$\frac{\partial B_z(x,y,z_0)}{\partial z} = F_{x,y}^{-1}\left[F_{x,y}[B_z(x,y,z_0)]\sqrt{k_x^2+k_y^2}\right], \tag{7.7}$$

which states that the derivative with respect to z of the magnetic field in the z direction at a height z_0 can be found if the field in the z direction at the same height $B_z(x,y,z_0)$ is known, by means of Fourier transforms between the (x,y) and (k_x,k_y) spaces, $F_{x,y}$[6]. The final expression is given by

$$V_{\omega_0}^1 = \beta(\omega_0)\alpha\left[\frac{V_{\omega_1}}{\beta\omega_2}\frac{\partial V_{\omega_2}}{\partial z} + \frac{V_{\omega_2}}{\beta\omega_1}\frac{\partial V_{\omega_1}}{\partial z}\right], \tag{7.8}$$

where $\partial V/\partial z$ is calculated according to equation (7.7) [or equivalently by using equation (A.37) in the Appendix]. The factor α can be calculated from the noise data as done before in section 6.6. The result of applying equation (7.8) to the measured data (Figs. 7.5 and 7.6) is shown in Fig. 7.9. Two dips with a size of -34μV and -60μV can be seen in the same place as those seen in Fig. 7.7. The size of the large dip is not very reliable since in the data processing Fourier transforms have been used, and since the data is neither periodic nor goes to zero on some of the boundaries, significant errors can be introduced, specially on the regions close to the borders where the data does not vanish. The signal shown in Fig. 7.5 is close to zero (or at least close to a constant level) at x=0, but at x=3μm it is still close to the maximum negative value (since the field has not yet decayed to zero at this position), so large errors close to the boundary at x=3μm are expected. On

[6]See the Appendix for more information.

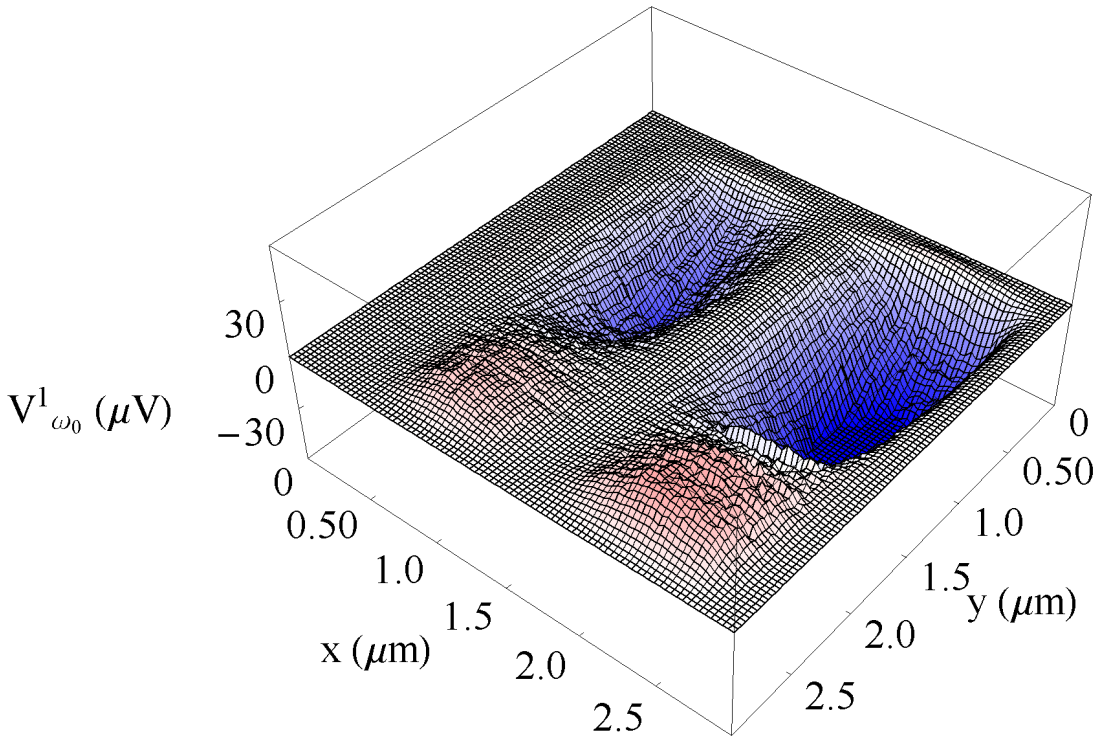

Figure 7.9: $V^1_{\omega_0}$ generated by equation (7.8).

the other hand the data close to the other boundary is expected to be more reliable since the magnetic signals have already decayed. Therefore a dip magnitude of -34μV should be much closer to the real value than -60μV. From Fig. 7.7 the size of the dips is about -23μV. Given the size of the errors that can be introduced by the procedure of calculating $V^1_{\omega_0}$ from the measured data, the difference between the measured and calculated values can be expected. The fact that the qualitative behavior is completely reproduced by the calculation and that the magnitude is

within a factor of 1.5[7], gives good evidence that the measurement setup is working correctly and that the model used to interpret the results is correct. Once again, given the accuracy with which quantities such as α and k are known, given the noise in the measurements, and given the systematic errors introduced by the calculations, the model is verified by the measurements.

However, no evidence for the detection of the excess magnetization in Cu was found. This was due in part to the thermal noise and low quality factor which limited the sensitivity of the MFM to 19×10^{-15}N, but also to the fact that unbalanced electrostatic effects and higher order signals appearing from the nonlinearity of the measurement were larger than the expected signal. The estimated size of the spin signal was larger than the measured noise, but interface spin-flip scattering could have decreased its size to below the noise level. This meas that the actual current spin polarization is smaller than the expected value of 5%. Transport measurements with tunnel barriers showed typical current spin polarizations of the order of 5% and as high as 17%, so it seems possible that by using resistive F-N interfaces the magnitude of the signal can be increased to a measurable value with the current configuration. However, the existence of resistive contacts increases the problems associated with unbalanced electrostatic potentials. Therefore decreasing the noise level by reducing the width and thickness of the cantilever [see equation (6.21)] is useful for detecting the spin signal. It is also useful to increase the quality factor or use higher frequencies in order to attenuate the higher order signals [see equation

[7]1.5 for the small dip or 2 for the average of the two dips.

(7.5)], increase the injected current spin polarization by using resistive barriers (Fig. 5.7), and reduce the electrostatic force between the tip and the sample.

Chapter 8
Summary and Conclusions
8.1 Transport

Spin injection and detection using both local and nonlocal configurations with transparent and resistive interfaces was shown for Co-Cu and Py-Cu spin valve structures. True nonlocal measurements on transparent Py-Cu spin valves were done, as opposed to previous measurements by Jedema et. al. [22] where their cross geometry measurements could include artifacts such as Hall effect and anomalous magneto resistance (AMR). The lack of reproducibility in the quality of the interfaces was pointed out. The large confidence intervals in the fits, and the fact that quantities not measured in the experiment such as the spin relaxation length and the spin resolved conductivities of Py either needed to be known for fitting the data or were used as fitting parameters, led to the conclusion that length dependence measurements of the spin relaxation length in mesoscopic wires with transparent interfaces was not reliable.

The temperature dependence of the spin related resistance was studied for the first time. In particular, the temperature dependence in the range from 100^oK to 300^oK of Py-Cu and Co-Cu transparent spin valve structures in the nonlocal config-

uration was measured. The temperature behavior of the antisymmetric component of the nonlocal resistance showed a linear behavior, which confirms the fact that the spin relaxation length is proportional to the mean free time so that at higher temperatures, where phonons are the main source of scattering, both relaxation times are proportional to 1/T. The existence of a previously unknown component of the nonlocal resistance, symmetric under the rotation of the magnetization direction of injector or detector, was demonstrated. This component vanished at lower temperatures (4.2^oK-100^oK) but increased nonlinearly above 100^oK. It was shown that by assuming interfacial spin-flip scattering so that spin resolved currents were not conserved at the interfaces, the existence of this new symmetric component could be phenomenologically understood, and information about the temperature dependence of the spin-flip scattering could be obtained. Confirmation that this new signal also came from spin transport effects was given by comparing the length dependence of this signal with the length dependence of the normal spin signal. Evidence to verify that the symmetric spin signal was not an artifact due to geometric effects, heating and thermopower, or current leakage, was also given. However, questions concerning the microscopic origin of the interfacial spin-flip scattering and its temperature dependence remain.

In terms of device applications, interfacial spin-flip scattering can significantly reduce the size of the changes in resistance in Giant Magneto Resistive (GMR) structures and Magnetic Tunnel Junctions (MTJ). In the first case this means reduced storage capacities in hard drives and slower response times while in the second case

it means higher power dissipation for readout of the MTJ state and larger RC time constants, and therefore reduced storage capacity and lower operating frequencies for MRAM's made of arrays of MTJ's.

Spin precession experiments in mesoscopic Cu wires were done for the first time. By using resistive Co-Cu interfaces and a nonlocal geometry the degree of injected spin current polarization was found to change over a wide range, from 0% to 17.2%. Although this high value of the spin current polarization is slightly less than half the value in Co, such a kind of device was not reproducible. The spin relaxation length was measured more precisely than with the length dependence method since a single injector and detector were used, avoiding the issue of interface reproducibility. An average value of 601 nm with a standard deviation of 6% was found, with the statistical deviation within the measurements error coming from uncertainties in the length and resistivity of the Cu wire segments between injector and detector.

The contact resistance was measured directly in most of the devices. This allowed better characterization of each contact, and verified that the equations valid in the limit of high contact resistance could be used.

Future work in this area includes using different kinds of resistive barriers, and different magnetic and nonmagnetic materials. Also, studying spin valves at lower temperatures might provide information on spin relaxation due to boundaries and impurities. In addition, the existence of spin polarized currents in the absence of any charge current, as in the case of the studied nonlocal geometry, opens the

possibility of studying fundamental issues related to pure spin transport, such as the study of spin transport statistics by measuring the zero charge current shot noise.

8.2 MFM

Spin injection into Cu using magnetic injectors, and detection of the excess magnetization with MFM was proposed, analyzed, and tested. It was theoretically shown that MFM detection was possible. However in practice, due to reduced spin injection which buried the signal below the thermal noise level, unbalanced electrostatic potentials, and higher order magnetic effects which masked the signal, it was impossible to detect the excess magnetization. However, improvements in the cantilever resolution were made by reducing the size of the magnetic covering to a small micron-sized region close to the apex of the tip. Improvements in the MFM sensitivity by means of a resonant method were made, and the results were compared with those from normal (phase) MFM operation by means of Fourier analysis, using special properties of the magnetic field produced by in-plane currents.

Additionally, a multi-frequency measurement setup that could separate the very large signals produced by the magnetic fields of injector and current from the small signal produced by the field of the excess magnetization was tested. Other artifacts, such as laser interference, were removed by subtracting consecutively acquired data points with and without current. The measurements verified the model used to interpret the data, and showed that the sensitivity was high enough to detect higher order effects coming from the injector and current fields, but the excess magnetization signal was still smaller than those effects. By repeating the experiment at

higher frequencies, unwanted higher order signals could be attenuated. Increasing the quality factor of the cantilevers by operating in vacuum could also increase the weight of the wanted to signal with respect to the higher order unwanted effects, as well as reduce the effects of thermal noise. In addition, reducing the noise by changing the cantilever geometry or operating at lower temperature would enhance the signal to noise ratio.

Reducing the electrostatic coupling between the tip and the sample or balancing the electrostatic potential so that the electric force on the tip is constant is essential. However this is not an easy task since decreasing the electrostatic coupling usually also decreases the magnetic coupling, and improving the implemented balancing scheme seems a difficult task. It is possible that by biasing the tip at the sum of DC and AC voltages, the electrostatic force can be measured at a particular frequency and after data analysis subtracted from the measured signal at resonance, to remove any electrostatic effects that appear at that frequency.

The current setup can in principle detect spin polarizations as small as P=5%. Spin polarizations of this order were obtained by using resistive F-N interfaces, but the transparent interfaces used for MFM measurements had lower values of P. Therefore using resistive junctions should give values of P which are large enough for MFM detection. However, resistive interfaces are accompanied by additional large electrostatic effects which make the electric balancing of the sample more difficult. MFM detection of an excess magnetization in Cu is feasible by making small improvements as those suggested above.

Appendix A

Magnetic field properties, Green's functions, and convolutions

Since in principle MFM only gives a signal related to the magnetic field in the z direction as a function of x and y at a constant height z_0, it is useful to consider the z coordinate separately from the other two. Additionally, special properties of the magnetic field produced by in-plane (x-y) currents or magnetizations can give information such as the field, or even derivatives of the field, at a different height. In this appendix I will review some of this special properties and will show that they are still true even for convoluted magnetic signals. From now on all of the currents and magnetizations will be assumed to have a vanishing component in the z direction, except of course by the magnetization of the cantilever tip which will be assumed to be in the z direction.

A.1 Magnetic field generated by an in-plane current

Let $\vec{J}(\vec{r}) = J_x(x,y,z)\hat{x} + J_y(x,y,z)\hat{y}$ be the current density in some bounded region of space Υ. The magnetic field in the z direction $B_z(\vec{r})$ at position $\vec{r}$ outside Υ is given by

$$
\begin{aligned}
B_z(\vec{r}) &= \frac{\mu_0}{4\pi}\hat{z}\cdot\nabla\times\int\frac{\vec{J}(\vec{r}')}{|\vec{r}-\vec{r}'|}d^3r' \\
&= \frac{\mu_0}{4\pi}\hat{z}\cdot\int\vec{J}(\vec{r}')\times\frac{\vec{r}-\vec{r}'}{|\vec{r}-\vec{r}'|^3}d^3r' \\
&= \frac{\mu_0}{4\pi}\int\frac{J_x(\vec{r}')(y-y')-J_y(\vec{r}')(x-x')}{|\vec{r}-\vec{r}'|^3}d^3r', \qquad \text{(A.1)}
\end{aligned}
$$

where as usual integrations without limits mean integration over all space. By using the 2D Fourier transform

$$
f(k_x,k_y)=\frac{1}{2\pi}\int F(x,y)\exp[\imath(k_xx+k_yy)]dxdy, \qquad \text{(A.2)}
$$

it is possible to rewrite equation (A.1) as

$$
b_z(k_x,k_y;z)=\frac{\mu_0}{8\pi^2}\int\frac{J_x(\vec{r}')(y-y')-J_y(\vec{r}')(x-x')}{|\vec{r}-\vec{r}'|^3}\exp^{\imath(k_xx+k_yy)}\,dxdyd^3r'. \qquad \text{(A.3)}
$$

Replacing $x-x'\rightarrow x$ and $y-y'\rightarrow y$ equation (A.3) can be written as

$$
\begin{aligned}
b_z(k_x,k_y;z) &= \int dz'\Bigg[\qquad \text{(A.4)} \\
&\frac{\mu_0}{8\pi^2}\int J_x(\vec{r}')\exp^{\imath(k_xx'+k_yy')}\,dx'dy'\int\frac{y}{[x^2+y^2+(z-z')^2]^{3/2}}\exp^{\imath(k_xx+k_yy)}\,dxdy- \\
&\frac{\mu_0}{8\pi^2}\int J_y(\vec{r}')\exp^{\imath(k_xx'+k_yy')}\,dx'dy'\int\frac{x}{[x^2+y^2+(z-z')^2]^{3/2}}\exp^{\imath(k_xx+k_yy)}\,dxdy\Bigg],
\end{aligned}
$$

where the integrals over $dx'dy'$ can be identified as the 2-D Fourier transforms of J_x and J_y,

$$
j_x(k_x,k_y;z') = \frac{1}{2\pi}\int J_x(\vec{r}')\exp^{\imath(k_xx'+k_yy')}\,dx'dy'
$$

$$j_y(k_x, k_y; z') = \frac{1}{2\pi} \int J_y(\vec{r}') \exp^{\imath(k_x x' + k_y y')} \, dx' dy', \tag{A.5}$$

and the integrals over $dxdy$ can be identified as the Fourier transforms of the Green's functions,

$$\begin{aligned} g_y(k_x, k_y; z - z') &= \frac{1}{2\pi} \int \frac{y}{[x^2 + y^2 + (z - z')^2]^{3/2}} \exp^{\imath(k_x x + k_y y)} \, dxdy \\ g_x(k_x, k_y; z - z') &= \frac{1}{2\pi} \int \frac{x}{[x^2 + y^2 + (z - z')^2]^{3/2}} \exp^{\imath(k_x x + k_y y)} \, dxdy. \end{aligned} \tag{A.6}$$

Therefore equation A.4 can be written as

$$\begin{aligned} b_z(k_x, k_y; z) = \frac{\mu_0}{2} \int [j_x(k_x, k_y; z') \, g_y(k_x, k_y; z - z') \\ - j_y(k_x, k_y; z') g_x(k_x, k_y; z - z')] dz'. \end{aligned} \tag{A.7}$$

For currents without any component in the $\hat{z}$ direction, the continuity equation

$$\frac{\partial J_x}{\partial x} + \frac{\partial J_y}{\partial y} = 0 \tag{A.8}$$

implies that in 2-D Fourier space

$$j_x k_x + j_y k_y = 0, \tag{A.9}$$

so equation (A.7) can be expressed as

$$b_z(k_x, k_y; z) = -\frac{\mu_0}{2} \int j_y(k_x, k_y; z') \, [g_y(k_x, k_y; z - z') k_y / k_x + g_x(k_x, k_y; z - z')] \, dz'. \tag{A.10}$$

If it is further assumed that the current is nonzero only in a slab between $z = 0$ and $z = d$ and that inside the slab the current does not have any z dependence, then

$$b_z(k_x, k_y; z) = -\frac{\mu_0}{2} j_y(k_x, k_y) \int_0^d \left[g_y(k_x, k_y; z - z') k_y/k_x + g_x(k_x, k_y; z - z') \right] dz', \tag{A.11}$$

which after a change of variables can be formulated as

$$b_z(k_x, k_y; z) = -\frac{\mu_0}{2} j_y(k_x, k_y)[g(k_x, k_y; z) - g(k_x, k_y; z - d)], \tag{A.12}$$

with the definition

$$g(k_x, k_y; z) = \int^z \left[g_y(k_x, k_y; z') k_y/k_x + g_x(k_x, k_y; z') \right] dz'. \tag{A.13}$$

Since the Fourier transforms applied for this derivation are only from the x-y to the k_x-k_y space, equation (A.12) can be simply extended to the derivatives of the field by directly applying to it the operator $\partial/\partial z$:

$$b'_z(k_x, k_y; z) = \frac{\partial}{\partial z} b_z(k_x, k_y; z). \tag{A.14}$$

Now, by replacing $x \exp(\imath k_x x) \rightarrow \partial/\partial(\imath k_x) \exp(\imath k_x x)$ and similarly for $y \exp(\imath k_y y)$ in equations (A.6), and then changing the integration from rectangular (x,y) to polar (ρ, ϕ) coordinates, $g_x(k_x, k_y; z)$ and $g_y(k_x, k_y; z)$ can be expressed as

$$g_x(k_x, k_y; z) \;\; = \;\; \frac{1}{2\pi\imath} \frac{\partial}{\partial k_x} g_0(z)$$

$$g_y(k_x, k_y; z) = \frac{1}{2\pi\imath}\frac{\partial}{\partial k_y} g_0(z), \tag{A.15}$$

with

$$g_0(z) = \int \rho \frac{\exp(\imath k\rho\cos\phi)}{(\rho^2 + z^2)^{3/2}} d\rho d\phi, \tag{A.16}$$

and $k = \sqrt{k_x^2 + k_y^2}$. By direct integration $g_0(z)$ is found to be

$$g_0(z) = 2\pi \exp^{-k|z|} / |z|, \tag{A.17}$$

so replacing this result in (A.15) gives

$$\begin{aligned} g_x(k_x, k_y; z) &= -\frac{k_x}{\imath k} \exp^{-k|z|} \\ g_y(k_x, k_y; z) &= -\frac{k_y}{\imath k} \exp^{-k|z|}, \end{aligned} \tag{A.18}$$

and therefore, from (A.13),

$$g(k_x, k_y; z) = -\frac{k}{\imath k_x} \int^z \exp^{-k|z'|} dz' = \frac{1}{\imath k_x} \exp^{-k|z|}. \tag{A.19}$$

Finally, for $z > d$, (A.12) can be expressed as

$$b_z(k_x, k_y; z) = -\frac{\mu_0}{2\imath k_x} \left[1 - \exp^{kd}\right] j_y(k_x, k_y) \exp^{-kz}. \tag{A.20}$$

Since the z dependence is separable from the k_x, k_y dependence, it is clear that if the field is known at a height z, then it can be found at a height z' by using

$$b_z(k_x, k_y; z') = b_z(k_x, k_y; z) \exp^{-k(z'-z)}, \tag{A.21}$$

and then making a 2-D inverse Fourier transformation. Additionally, by applying the z derivative operator as shown in (A.14), it is clear that the derivative of the field and the field are related by

$$b'_z(k_x, k_y; z) = -k b_z(k_x, k_y; z). \tag{A.22}$$

The n'th order derivative can be easily found to be related to the field by

$$b_z^{(n)}(k_x, k_y; z) = (-k)^n b_z(k_x, k_y; z). \tag{A.23}$$

A.2 Magnetic field generated by an in-plane magnetization

Let $\vec{M}(\vec{r}) = M_x(x, y, z)\hat{x} + M_y(x, y, z)\hat{y}$ be the magnetization in some bounded region of space Υ. The magnetic scalar potential $\Psi(\vec{r})$ at position $\vec{r}$ outside Υ is given by

$$\begin{aligned} \Psi(\vec{r}) &= -\frac{\mu_0}{4\pi} \nabla \cdot \int \frac{\vec{M}(\vec{r}')}{|\vec{r} - \vec{r}'|} d^3 r' \\ &= -\frac{\mu_0}{4\pi} \int \frac{M_x(\vec{r}')(x - x') + M_y(\vec{r}')(y - y')}{|\vec{r} - \vec{r}'|^3} d^3 r'. \end{aligned} \tag{A.24}$$

As usual, the relation between the magnetic scalar potential and the magnetic field is given by $\vec{B} = -\nabla\Psi$ so $B_z = -\partial\Psi/\partial z$. The procedure leading to equation (A.7) in the previous section can be followed to give

$$\psi(k_x,k_y;z) = -\frac{\mu_0}{2}\int [m_x\,(k_x,k_y;z')g_x(k_x,k_y;z-z') \\ +m_y(k_x,k_y;z')g_y(k_x,k_y;z-z')]dz', \qquad \text{(A.25)}$$

where g_x and g_y are given by equation (A.6) and m_x and m_y are the 2-D Fourier transforms of the magnetization[1] given by

$$\begin{aligned} m_x(k_x,k_y;z') &= \frac{1}{2\pi}\int M_x(\vec{r}')\exp^{\imath(k_x x'+k_y y')}\,dx'dy' \\ m_y(k_x,k_y;z') &= \frac{1}{2\pi}\int M_y(\vec{r}')\exp^{\imath(k_x x'+k_y y')}\,dx'dy'. \end{aligned} \qquad \text{(A.26)}$$

Since there is no continuity equation for the magnetization, it is necessary to keep both independent functions m_x and m_y in the procedure. If the magnetization is further assumed to be nonzero only in a slab between $z = 0$ and $z = d$, and have no z dependence in the slab, the procedure which lead to equation (A.20) in the previous section can be followed identically to give

$$b_z(k_x,k_y;z) = -\frac{\mu_0}{2\imath k}\left[1-\exp^{kd}\right]\left[k_x m_x(k_x,k_y)+k_y m_y(k_x,k_y)\right]\exp^{-kz}, \qquad \text{(A.27)}$$

after using $b_z = -\partial\psi/\partial z$. Since once more the z dependence is completely separable and has the same form as in (A.20), equations (A.21)-(A.23) also apply to the case of a slab with in plane magnetization.

[1]Not to be confused with the magnetic moment, which is usually also denoted by m.

A.3 2-D Convolution

The signal detected by the MFM is not the derivative of the field in the z direction but instead its convolution with the magnetization of the tip. Therefore it is not obvious that the relations derived above, which apply to the field B_z, should also hold for the measured signal. In this section it will be shown that equations (A.21)-(A.23) are also valid for the measured convoluted signal.

Let U be the negative of the convolution of the magnetic field with the magnetization $\vec{M} = M\hat{z}$ of the tip, assumed to be in the z direction,

$$U(\vec{r}) = -\int B_z(\vec{r}+\vec{r}')M(\vec{r})d^3r'. \tag{A.28}$$

U is therefore the magnetic energy stored in the system. The measured signal, up to calibration constants, is given by $V = -\partial U/\partial z$. Following the procedure described at the beginning of section A, it is possible to write the 2-D fourier transform of U as

$$u(k_x, k_y; z) = -2\pi \int b_z(k_x, k_y; z+z')m(-k_x, -k_y, z')dz'. \tag{A.29}$$

Using the property (A.21) of the magnetic field, u can be written as

$$u(k_x, k_y; z) = -b_z(k_x, k_y; z)m_{2D}(-k_x, -k_y), \tag{A.30}$$

where the 2-D convolution factor in Fourier space $m_{2D}(k_x, k_y)$ is given by

$$m_{2D}(k_x, k_y) = 2\pi \int \exp^{-kz'} m(k_x, k_y, z')dz'. \tag{A.31}$$

Therefore the measured signal v is given by

$$v(k_x, k_y; z) = b'_z(k_x, k_y; z)m_{2D}(-k_x, -k_y), \tag{A.32}$$

Since the z dependence of $v(k_x, k_y; z)$ is given exactly by that of $b'_z(k_x, k_y; z)$, it is clear that equations (A.21)-(A.23) also apply to $v(k_x, k_y; z)$, hence

$$\begin{aligned} v(k_x, k_y; z') &= v(k_x, k_y; z) \exp^{-k(z'-z)} & \text{(A.33)} \\ v^{(n)}(k_x, k_y; z') &= (-k)^n v(k_x, k_y; z). & \text{(A.34)} \end{aligned}$$

A.4 1-D Convolution

If the measured field is constant in the y direction, then a 1-D Fourier transform can be used instead, and the procedure of the last section can be repeated. In this case, however, the measured signal is $v(k_x; z)$ and the 1-D convolution factor is given by

$$m_{1D}(k_x) = \sqrt{2\pi} \int \exp^{-kz'} m(k_x, y', z')dy'dz'. \tag{A.35}$$

Equations (A.33) and (A.33) are replaced by

$$\begin{aligned} v(k_x; z') &= v(k_x; z) \exp^{-k(z'-z)} & \text{(A.36)} \\ v^{(n)}(k_x; z') &= (-k)^n v(k_x; z). & \text{(A.37)} \end{aligned}$$

BIBLIOGRAPHY

[1] A. T. Filip, B. H. Hoving, F. J. Jedema, B. J. van Wees, B. Dutta, and S. Borghs. Experimental search for the electrical spin injection in a semiconductor. *Phys. Rev. B*, 62:9996–9999, 2000.

[2] M. Oestreich, M. Brender, J. Hübner, D. Hägele, W. W. Rühle, Th. Hartman P. J. Klar, W. Heimbrodt, M. Lampalzer, K. Voltz, and W. Stolz. Spin injection, spin transport and spin coherence. *Semicond. Sci. Technol.*, 17:285–297, 2002.

[3] M. Johnson and R. H. Silsbee. Interfacial charge-spin coupling: Injection and detection of spin magnetization in metals. *Phys. Rev. Lett.*, 55:1790–1793, 1985.

[4] Y. Yafet. Calculation of the g factor of metallic sodium. *Phys. Rev.*, 85:478, 1952.

[5] R. J. Elliott. Theory of the effect of spin-orbit coupling on magnetic resonance in some semiconductors. *Phys. Rev.*, 96:266–279, 1954.

[6] N. F. Mott. The electrical conductivity of transition metals. *Proc. R. Soc. London, Ser. A*, 153:699–717, 1936.

[7] N. F. Mott. The resistance and thermoelectric properties of the transition metals. *Proc. R. Soc. London, Ser. A*, 156:368–382, 1936.

[8] I. A. Campbell, A. Fert, and A. R. Pomeroy. Evidence for two current conduction iron. *Phil. Mag.*, 15:977–983, 1967.

[9] A. Fert and I. A. Campbell. Two-current conduction in nickel. *Phys. Rev. Lett.*, 21:1190–1192, 1968.

[10] T. Valet and A. Fert. Theory of the perpendicular magnetoresistance in magnetic multilayers. *Phys. Rev. B*, 48:7099–7113, 1993.

[11] S. Maekawa and T. Shinjo (Eds.). *Spin Dependent Transport in Magnetic Nanostructures*. Taylor and Francis, New York, 2002.

[12] S. S. P. Parkin *et al.* Magnetically engineered spintronic sensors and memory. *Proc. IEEE*, 91:661–680, 2003.

[13] I. Žutić, J. Fabian, and S. Das Sarma. Spintronics: Fundamentals and applications. *Rev. Mod. Phys.*, 76:323–410, 2004.

[14] V. A. Vas'ko *et al.* Critical current suppression in a superconductor by injection of spin-polarized carriers from a ferromagnet. *Phys. Rev. Lett.*, 78:1134–1137, 1997.

[15] J. Ngai *et al.* Scanning tunneling spectroscopy under pulsed spin injection. *Appl. Phys. Lett.*, 84:1907–1909, 2004.

[16] A. H. MacDonald. Spin bottlenecks in the quantum Hall regime. *Phys. Rev. Lett.*, 83:3262–3265, 1999.

[17] H. B. Chan *et al.* Tunneling into ferromagnetic quantum Hall states: Observation of a spin bottleneck. *Phys. Rev. Lett.*, 83:3258–3261, 1999.

[18] Q. Si. Spin injection into a Luttinger liquid. *Phys. Rev. Lett.*, 81:3191–3194, 1998.

[19] L. Balents and R. Egger. Spin transport in interacting quantum wires and carbon nanotubes. *Phys. Rev. Lett.*, 85:3464–3467, 2000.

[20] M. Johnson. Bipolar spin switch. *Science*, 260:320–323, 1993.

[21] M. Johnson. Spin accumulation in gold films. *Phys. Rev. Lett.*, 70:2142–2145, 1993.

[22] F. J. Jedema, A. T. Filip, and B. J. van Wees. Electrical spin injection and accumulation at room temperature in an all-metal mesoscopic spin valve. *Nature*, 410:345–348, 2001.

[23] F. J. Jedema, H. B. Heersche, A. T. Filip, J. J. A. Baselmans, and B. J. van Wees. Electrical detection of spin precession in a metallic mesoscopic spin valve. *Nature*, 416:713–716, 2002.

[24] M. Johnson and R. H. Silsbee. Thermodynamic analysis of interfacial transport and of the thermomagnetoelectric system. *Phys. Rev. B*, 35:4959–4972, 1987.

[25] E. I. Rashba. Diffusion theory of spin injection through resisitive contacts. *Eur. Phys. J. B*, 29:513–527, 2002.

[26] S. Takahashi and S. Maekawa. Spin injection and detection in magnetic nanostructures. *Phys. Rev. B*, 67:052409, 2003.

[27] R. H. Silsbee. Novel method for the study of spin transport in conductors. *Bull. Magn. Reson.*, 2:284–285, 1980.

[28] F. J. Jedema *et al.* Electrical detection of spin precession in a metallic mesoscopic spin valve. *Nature*, 416:713–716, 2002.

[29] T. D. Stowe, K. Yasumura, T. W. Kenny, D. Botkin, K. Wago, and D. Rugar. Attonewton force detection using ultrathin silicon cantilevers. *Appl. Phys. Lett.*, 71:288–290, 1997.

[30] H. J. Mamin, R. Budakian, B. W. Chui, and D. Rugar. Detection and manipulation of statistical polarization in small spin ensembles. *Phys. Rev. Lett.*, 91:207604, 2003.

[31] D. Rugar, R. Budakian, H. J. Mamin, and B. W. Chui. Single spin detection by magnetic resonance force microscopy. *Nature*, 430:329–332, 2004.

[32] F. Bloch. Nuclear induction. *Phys. Rev.*, 70:460–474, 1946.

[33] H. C. Torrey. Bloch equations with diffusion terms. *Phys. Rev.*, 104:563–565, 1956.

[34] A. Abragam. *The Principles of Nucelar Magnetism*. Oxford University Press, London, 1961.

[35] R. K. Wangsness and F. Bloch. The dynamical theory of nuclear induction. *Phys. Rev.*, 89:728–739, 1953.

[36] D. Pines and C. P. Slichter. Relaxation times in magnetic resonance. *Phys. Rev.*, 100:1014–1020, 1955.

[37] V. V. Andreev and V. I. Gerasimenko. On the theory of paramagnetic resonance and paramagnetic relaxation in metals. *Zh. Exp. Teor. Fiz.*, 35:1209–1215, 1958. [Sov. Phys. JETP **35**, 846-850 (1959)].

[38] Y. Yafet. g factors and spin-lattice relaxation of conduction electrons. In F. Seitz and D. Turnbull, editors, *Solid State Physics, Vol. 14*, page 2. Academic, New York, 1963.

[39] A. W. Overhauser. Paramagnetic relaxation in metals. *Phys. Rev.*, 89:689–700, 1953.

[40] J. Kondo. Theory of dilute magnetic alloys. *Sol. Stat. Phys.*, 23:184, 1969.

[41] C. Kittel. *Introduction to Solid State Physics, 7th Ed.* Wiley, New York, 1996.

[42] M. A. Blachly and N. Giordano. Kondo effect in cu(fe) films. *Phys. Rev. B*, 49:6788–6793, 1994.

[43] Wei Wei and Gerd Bergmann. Cuco: A new surface kondo system. *Phys. Rev. B*, 37:5990–5993, 1988.

[44] J. J. Hauser, D. R. Hamann, and G. W. Kammlott. Investigation of kondo alloys and compound by the superconductive proximity effect. *Phys. Rev. B*, 3:2211–2223, 1971.

[45] T. W. Griswold, A. F. Kip, and C. Kittel. Microwave spin resonance absorption by conduction electrons in metallic sodium. *Phys. Rev.*, 88:951–952, 1952.

[46] G. Feher and A. F. Kip. Electron spin resonance absorption in metals. I. Experimental. *Phys. Rev.*, 98:337–348, 1955.

[47] W. Kolbe. Spin relaxation time of conduction electrons in bulk sodium metal. *Phys. Rev. B*, 3:320–323, 1971.

[48] N. W. Ashcroft and N. D. Mermin. *Solid State Physics*. Sounders, Philadelphia, 1976.

[49] F. J. Jedema. Electrical spin injection in metallic mesoscopic spin valves. *Ph.D. Thesis (Rijksuniversiteit Groningen)*, 2002.

[50] M. Johnson and R. H. Silsbee. Ferromagnet-nonferromagnet interface resistance. *Phys. Rev. Lett.*, 60:377, 1988.

[51] E. I. Rashba. Theory of electrical spin injection: Tunnel contacts as a solution of the conductivity mismatch problem. *Phys. Rev. B*, 62:R16267–R16270, 2000.

[52] J. Bass and W. P. Pratt, Jr. Current-perpendicular (CPP) magnetoresistance in magnetic metallic multilayers. *J. Magn. Magn. Mater.*, 200:274–289, 1999.

[53] B. T. Jonker, S. C. Erwin, A. Petrou, and A. G. Petukhov. Electrical spin injection and transport in semiconductor spintronic devices. *MRS Bull.*, 28:740–748, 2003.

[54] J. J. Sakurai. *Modern Quantum Mechanics*. Addison-Wesley, 1994.

[55] M. Johnson and R. H. Silsbee. Coupling of electronic charge and spin at a ferromagnetic-paramagnetic metal interface. *Phys. Rev. B*, 37:5312–5325, 1988.

[56] John G. Simmons. Electric tunnel effect between dissimilar electrodes separated by a thin insulating film. *J. Appl. Phys.*, 34:2581–2590, 1963.

[57] John G. Simmons. Generalized thermal j-v characteristic for the electric tunnel effect. *J. Appl. Phys.*, 35:2655–2658, 1964.

[58] Q. Yang, P. Holody, S.F. Lee, L. L. Henry, R. Loloee, P. A. Schroeder, Jr. W. P. Pratt, , and J. Bass. Spin flip diffusion length and giant magnetoresistance at low temperatures. *Phys. Rev. Lett.*, 72:3274–3277, 1994.

[59] S. Dubois, L. Piraux, J. M. George, K. Ounadjela, J. L. Duvail, and A. Fert. Evidence for a short spin diffusion length in permalloy from the giant magnetoresistance of multilayered nanowires. *Phys. Rev. B*, 60:477–484, 1999.

[60] P. Holody, W. C. Chiang*, R. Loloee, J. Bass, Jr. W. P. Pratt, and P. A. Schroeder. Giant magnetoresistance of copper/permalloy multilayers. *Phys. Rev. B*, 58:12230–12236, 1998.

[61] S. D. Steenwyk, S. Y. Hsu, R. Loloee, J. Bass, and Jr. W. P. Pratt. Perpendicular-current exchange-biased spin-valve evidence for a short spin-diffusion lenght in permalloy. *J. Magn. Magn. Mater.*, 170:L1–L6, 1997.

[62] J. R. Petta and D. C. Ralph. Studies of spin-orbit scattering in noble-metal nanoparticles using energy-level tunneling spectroscopy. *Phys. Rev. Lett.*, 87:266801, 2001.

[63] S. Schultz and C. Latham. Observation of electron spin resonance in copper. *Phys. Rev. Lett.*, 15:148–151, 1965.

[64] F. Beuneu and P. Monod. The Elliott relation in pure metals. *Phys. Rev. B*, 18:2422–2425, 1978.

[65] C. H. Shang, J. Nowak, R. Jansen, and J. S. Moodera. Temperature dependence of magnetoresistance and surface magnetization in ferromagnetic tunnel junctions. *Phys. Rev. B*, 58:R2917–R2920, 1998.

[66] F. Bloch. Zur theorie des ferromagnetismus. *Z. Phys.*, 61:206, 1930.

[67] D. Y. Petrovykh, K. N. Altmann, H. Hochst, M. Lauscher, S. Maat, G. J. Mankey, and F. J. Himpsel. Spin-dependent band structure, fermi surface, and carrier lifetime of permalloy. *Appl. Phys. Lett.*, 73:3459, 1998.

[68] J. Scott, S. Mc Vitie, R. P. Ferrer, and A. Gallagher. Electrostatic charging artefacts in lorentz electron tomography of mfm tip stray fields. *J. Phys. D: Appl. Phys.*, 34:1326–1332, 2001.

[69] J. D. Jackson. *Classical Electrodynamics, 3nd Ed.* Wiley, New York, 1998.

[70] Y. Martin, C. C. Williams, and H. K. Wickramasinghe. Atomic force microscopeforce mapping and profiling on a sub 100- scale. *J. Appl. Phys.*, 61:4723–4729, 1987.

[71] J. P. Cleveland, S. Manne, D. Bocek, and P. K. Hansma. A nondestructive method for determining the spring constant of cantilevers for scanning force microscopy. *Rev. Sci. Instrum.*, 64:403–405, 1993.

[72] T. R. Albrecht, P. Grutter, D. Horne, and D. Rugar. Frequency modulation detection using high-q cantilevers for enhanced force miscroscopy sensitivity. *J. Appl. Phys.*, 69:668–673, 1991.

[73] R. Yongsunthon, A. Stanishevsky, E. D. Williams, and P. J. Rous. Mapping electron flow using magnetic force microscopy. *Appl. Phys. Lett.*, 82:3287–3289, 2003.

[74] R. Yongsunthon. Magnetic force microscopy for observation of current crowding in electromigration phenomena. *Ph.D. Thesis (University of Maryland at College Park)*, 2002.

[75] S. Belaidi, P. Girard, and G. Leveque. Electrostatic forces acting on the tip in atomic force microscopy: Modelization and comparison with analytic expressions. *J. Appl. Phys.*, 81:1023–1030, 1997.

[76] S. Hudlet, M. Saint Jean, C. Guthmann, and J. Berger. Evaluation of the capacitive force between an atomic force microscopy tip and a metallic surface. *Euro. Phys. Jour. B*, 2:5–10, 1998.